NUMERICAL INVESTIGATION OF AN INVERSE THEOREM FOR COMPUTER TOMOGRAPHY

By

SAMUDRA VIJAY

NETP
1992
M
VIJ
NUM

NUCLEAR ENGINEERING AND TECHNOLOGY PROGRAMME

INDIAN INSTITUTE OF TECHNOLOGY KANPUR

APRIL, 1992

NUMERICAL INVESTIGATION OF AN INVERSE THEOREM FOR COMPUTER TOMOGRAPHY

A Thesis Submitted
in Partial Fulfilment of the Requirements
for the Degree of
MASTER OF TECHNOLOGY

By
SAMUDRA VIJAY

to the
NUCLEAR ENGINEERING AND TECHNOLOGY PROGRAMME
INDIAN INSTITUTE OF TECHNOLOGY, KANPUR
April 1992

2
CENTRAL LIBRARY
113495

NETP - 1992 - M-VII NIN

13.4.92

Certificate

This is to certify that this work on "A NUMERICAL INVESTIGATION OF AN INVERSE THEOREM FOR COMPUTER TOMOGRAPHY" by Mr Samudra Vijay has been carried out under my supervision and has not been submitted elsewhere for the award of a degree.

(Prabhat Munshi)
Assistant Professor
Nuclear Engineering and Technology Programme
I. I. T.– Kanpur

April 1992

Acknowledgements

I wish to express my sincere thanx to Dr. Prabhat Munshi for his constant encouragement and guidance.

I also wish to express deep sense of gratitude to my teachers Prof. K. Sriram, Dr. M. S. Kalra and Dr. A. Sengupta for 'enrichment' of my knowledge during the course of study.

Co-operation of other N. E. T. family members , Tomar ji, Pathak ji, Yadav ji, Mohasin & Gopal is also appreciated.

Thanks to Amitava, Gyaniji, Verma, S. K. Bhargava, Dr. P. Kumar and P. Manmohan for making the stay at I I T/ K enjoyable.

Discussions with Shekhar & Mukul gave me a wider perspective and helped development of better understanding.

A special note of thanks to K. M. Singh, without whom this thesis could have not been presented in a nice form.

— Samudra Vijay

Contents

Certificate i

Acknowledgements ii

List of Figures v

List of Tables vii

Nomenclature viii

Abstract ix

1 Introduction 1

2 Preliminaries 3

2.1 Data Collection Modes 4

2.1.1 Parallel–Beam Geometry 4

2.1.2 Fan–Beam Geometry 5

2.2 Mathematical Formulae for Tomographic Inversion 5

2.2.1 Parallel Beam Formulation 8

2.2.2 Fan–Beam Formulation 9

2.3 Convolution Back–Projection Algorithm 10

3 Program Implementation and Description 11

3.1 Computer Implementation of the CBP Algorithm 11
3.2 Errors Involved in Tomographic Inversion 13
3.2.1 Inherent error 13
3.2.2 Discretization error 14

4 Results and Discussion **16**
4.1 Data Used 16
4.2 Results 16
4.3 Discussion 17

5 Conclusions and Recommendations **46**

A Reconstructed Images **48**

B Error Variation with Frequency **60**

Bibliography **81**

List of Figures

2.1 Parallel–Beam Geometry 6

2.2 Fan–Beam Geometry 7

4.1 Original simulation of BRN, JET, CRO and THO 19

4.2 Original simulation of TST, SAT, LIN and FIN 20

4.3 Original simulation of GIN, IND and PIC 21

4.4 Maximum error variation at higher frequencies for SAT 26

4.5 Minimum error variation at higher frequencies for SAT 27

4.6 Maximum error variation at higher frequencies for LIN 28

4.7 Minimum error variation at higher frequencies for LIN 29

4.8 Maximum error variation at higher frequencies for FIN 30

4.9 Minimum error variation at higher frequencies for FIN 31

4.10 Maximum error variation at higher frequencies for GIN 32

4.11 Minimum error variation at higher frequencies for GIN 33

4.12 Maximum error variation at higher frequencies for JET 34

4.13 Minimum error variation at higher frequencies for JET 35

4.14 Maximum error variation at higher frequencies for CRO 36

4.15 Minimum error variation at higher frequencies for CRO 37

4.16 Maximum error variation at higher frequencies for THO 38

4.17 Minimum error variation at higher frequencies for THO 39

4.18 Maximum error variation at higher frequencies for TST 40

4.19 Minimum error variation at higher frequencies for TST 41
4.20 Maximum error variation at higher frequencies for BRN 42
4.21 Minimum error variation at higher frequencies for BRN 43
4.22 Maximum error variation at higher frequencies for PIC 44
4.23 Minimum error variation at higher frequencies for PIC 45

List of Tables

4.1 List of images used for reconstruction 18

4.2 Summary of errors in reconstruction of images SAT, LIN and FIN . . 22

4.3 Summary of errors in reconstruction of images GIN, JET and CRO . 23

4.4 Summary of errors in reconstruction of images THO, TST and BRN . 24

4.5 Summary of errors in reconstruction of images PIC and IND 25

Nomenclature

A	Cut-off frequency in the spatial frequency domain
c	Path of radiation
CAT	Computer Aided Tomography
CBP	Convolution backprojection
e_R	Inherent error
e_D	Discretization error
ERL	Average error as defined in 3.2.2
$ERMIN$	Minimum error of the reconstructed image
$ERMAX$	Maximum error of the reconstructed image
F	Spatial frequency
FBG	Fan beam geometry
$NRAY$	Number of rays in a view
$NVIEW$	Number of views
$p(s;\theta)$	Projected data
PBG	Parallel beam geometry
R_c	Cut-off frequency
$W(F)$	Window or filter function
Δs	Distance between two consecutive parallel lines
$\mu(r,\phi)$	Point dependent attenuation coefficient of the material
ρ	Density of the given material
θ	Angle between the Y-axis and the given ray in PBG

Abstract

CT is being used in various areas. Of the various algorithms reported so far, e.g. Convolution Backprojection (CBP), ART, Direct Fourier Inversion etc. the CBP algorithm has gained wide acceptance and popularity owing to its efficiency and ease of application. Some error estimates for the CBP algorithm have been reported by Natterar and Munshi et al, which incorporate the assumption of the projection data being essentially band limited. Due to finite frequency cut-off incorporated in implementation of CBP algorithm, the approximation obtained is having inherent error, e_R. A practical implementation of CBP method also introduce, apart from e_R, the discretization error arising due to discrete implementation of the convolution and backprojection integral. A numerical study of these errors for reconstruction of simulated images, using CBP was carried out. The results show that they are in tune with the theoretical predictions. Errors are found to be of the order $O(1/R_c)$.

Chapter 1

Introduction

The development of imaging systems based on the concept of computerized tomography has revolutionised the area of medical imaging. The potential of CT scanners is also being harnessed in the field of non destructive evaluation, at a large scale. This technique has proved its worth not only in the detection of cancerous tissues, but also in the area of void fraction measurment of two phase flow.

Problem of determination of cross sectional distribution of any property arises in many fields. Direct methods to solve the problem are not possible in many of the cases like non destructive testing, two phase flow, and medical imaging etc. Indirect methods are employed in such cases.

Projection data (refer chapter 2) can be obtained without much problem, by making use of x-ray, gama ray, or ultrasonic source detector system. Now the major problem to be dealt with is reconstruction of image from the projection data. Radon [1] paved the way to solve this hurdle in 1917. He proved that any arbitrary function could be recovered from its set of line integral taken along various chords and various directions, using Radon inversion formula. But this could not be implemented due to inherent mathematical complexities. Bracewell [2] reported an application of CT in radio astronomy and Cormack[3] derived an inversion formula in 1963. These two were

more closer to implementation than the Radon inversio formula. Bracewell & Riddle [4] made use of convolutions in 1967, which accelerated the CT computations. The use of RL filter by Ramachandran & Lakshminarayan[5] further accelerated the CT methodology. But it was Hounsfield[6] who pioneered the way to practical application of CT in 1973.

Some work has been done at IIT Kanpur, which deals with many fundamental problems in the field of CT[7]. This involves void fraction measurement using algorithms of gamma-ray tomography[8], estimation of error for tomographic inversions[9], and developing new filters for image reconstruction[10,11].

This study involves reconstruction of given images, using CBP algorithm, for different number of rays and studying the error in the reconstructed images.

Chapter 2

Preliminaries

When a beam of photon is incident on matter, it can interact with matter in many ways. Some of the photons are scattered, some undergo absorption, and rest are transmitted. The transmitted beam is said to be attenuated. The attenuation depends on thickness of the object and energy of the incident beam.

Single beam mono-energetic radiation attenuation phenomenon in a plane can be represented as follows :

$$N = N_0 \exp[-\int_c \mu(r, \phi)\ \mathrm{d}l] \tag{2.1}$$

where

N is no of incident photons,

N_0 is no of detected photons,

μ is linear attenuation coefficient for given energy,

l is the integration variable,

c chord, along which function is to be integrated, and

r, ϕ are cylindrical co-ordinates.

The value of μ for a given material depends on the type of radiation and energy of the radiation. In the equation (2.1) energy dependence of μ is ignored. μ is considered to be a function of r and ϕ only, as the radiation is restricted to a plane only.

The equation can be rewritten as :

$$p = \int_c \mu(r, \phi) \mathrm{d}l \tag{2.2}$$

where

$$p = \ln(N_0/N), \tag{2.3}$$

Now we have to find the value of $\mu(r, \phi)$ for getting the density distribution. Radon[1] showed that μ can be recovered from a set of p–values measured along various strips, using following formula :

$$\mu(r, \phi) = -\frac{1}{2\pi^2} \lim_{\epsilon \to 0} \int_\epsilon^\infty \frac{1}{q} \int_0^{2\pi} m_1(r\cos\phi + rsin\phi + q,\ \phi)\, d\phi\, dq, \tag{2.4}$$

where m_1 denotes partial derivative of $\mu(r, \phi)$ with respect to r. Rigorous proof of this formula is discussed by Herman[12]. The above written Radon formula has many implementation problems. In CT we have only a finite set of measurements, which are not sufficient to reconstruct the image accurately. Moreover the Radon formula is very sensitive to some inaccuracies which are inherent in CT like beam hardening, photon statistics, detector inaccuracies etc.

2.1 Data Collection Modes

Projection data are required for CT, collected by an array of radiation detectors for reconstruction of the function $\mu(r, \phi)$. Various data collection modes are discussed by Herman[12]. Two popular modes of data collection are termed as parallel-beam geometry (PBG) and fan-beam geometry (FBG).

2.1.1 Parallel–Beam Geometry

PBG mode CT scanners have a no. of uniformly spaced source-detector pairs. The object is mounted at the centre, around which are located the source-detector pairs.

The object can be rotated to give different values of angle θ. For each value of θ a set of projection data is collected. Figure (2.1) depicts PBG configuration.

The line SD represents the path of the data ray. The perpendicular distance of the ray from the origin is denoted by s. Several SD pairs collect the data p for a given θ. This set of p is known as a 'projection', which are collected for different views (at different θ). This data is denoted by $p(s;\theta)$.

2.1.2 Fan–Beam Geometry

In this mode, a single source is viewed by several detectors, simultaneously. The source angle is denoted by σ and the detector angle by β. The readings are taken at different values of β to get the data, denoted by $g(\sigma,\beta)$ or $h(l,\beta)$. Here, l is the perpendicular distance from the origin to the particular ray. This configuration, depicted in Fig.2.2, is widely used in tomography for medical purposes.The FBG mode can be implemented for a rotating object system as well. The data collection methodology remains the same as that for the PBG case.

2.2 Mathematical Formulae for Tomographic Inversion

The mathematical methods used to retrieve a two dimensional function from its projection data, known as Tomographic inversion methods, are generally categorized as the 'transform methods' and the 'algebraic reconstruction techniques'. The transform methods are based on mathematical formulae while the latter are iterative computational techniques. Algebraic reconstruction is useful when the no. of projection data available is small. Whereas transform methods give accurate results only with sufficient projection data. In the following sections, "transform" methods are briefly summarised for the two data collection geometries.

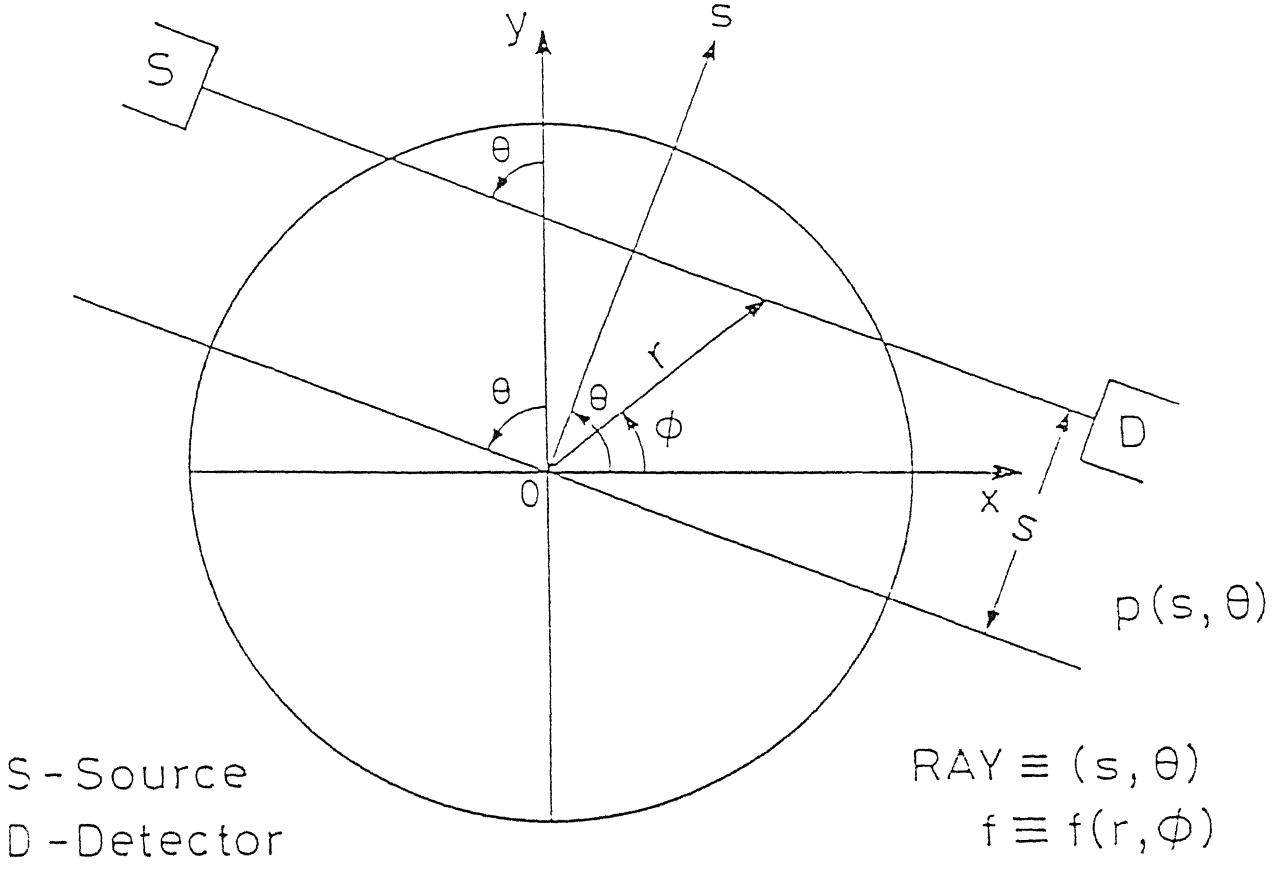

Figure 2.1: Parallel–Beam Geometry

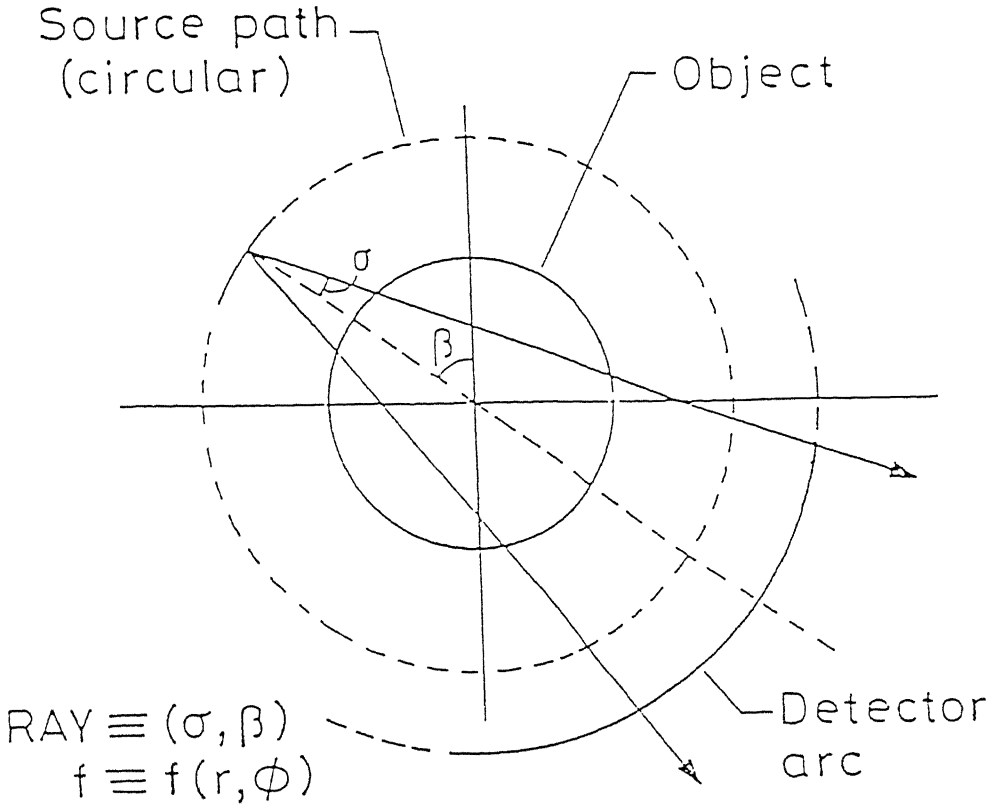

Figure 2.2: Fan-Beam Geometry

2.2.1 Parallel Beam Formulation

The reconstruction process of a two-dimensional function from its projections (line integrals) involves Fourier transforms for parallel beams and Hilbert transforms for divergent beam data. A very convenient transformation from FBG to PBG avoids the use of the Hilbert transform. The 'central-slice' theorem (also called the projection theorem) states that the one dimensional Fourier transform of the projection data, $p(s;\theta)$, with respect to the first variable s, is equal to the two-dimensional Fourier transform of the object function f. Mathematically,

$$\hat{f}(F;\theta) = \hat{p}(F;\theta) \tag{2.5}$$

Taking the inverse Fourier transform of (2.5) we get

$$f(r,\phi) = \int_0^{\pi} \int_{-\infty}^{\infty} \hat{p}(F;\theta)\, \exp[-i2\pi F r \cos(\theta-\phi)]|F|\, dF\, d\theta \tag{2.6}$$

For a given θ,

$$\hat{p}(F;\theta) = \int_{-R}^{R} p(s;\theta) \exp[-i2\pi F s]\, ds. \tag{2.7}$$

Equation (2.6) requires continuous projection data for all values of s and θ. For computational feasibility, a filter function is incorporated in the Fourier domain, to enable a finite cutoff frequency. This necessity arises because the limits on R vary from $-\infty$ to $+\infty$, which introduces divergence. This filter function, $W(F)$, vanishes for $|F|$ greater than A, the cut-off frequency. Equation (2.6) is transformed to

$$\tilde{f}(r,\phi) = \int_0^{\pi} \int_{-\infty}^{\infty} \hat{p}(F;\theta)\, \exp[-i2\pi F r \cos(\theta-\phi)]W(F)|F|\, dF\, d\theta. \tag{2.8}$$

The reconstruction is approximate as all the higher frequencies have been eliminated. Besides, as per the sampling theorem, the cut-off frequency and the sampling interval in the spatial domain are related by

$$A \geq [1/(2\Delta s)], \tag{2.9}$$

where Δs is the spacing between the rays.

The band-limiting filter, introduced in electron micrography by Ramachandran & Lakshminarayan[5] is given by

$$W(F) = \begin{cases} 1, & |F| < A, \\ 0, & |F| \geq A. \end{cases} \tag{2.10}$$

The sinc filter used by Shepp & Logan[13] is given by,

$$W(F) = \begin{cases} [\sin(\pi F/2A)]/(\pi F/2A), & |F| < A, \\ 0, & |F| \geq A. \end{cases} \tag{2.11}$$

The filter used in this thesis is the Ramchandran filter.

2.2.2 Fan–Beam Formulation

The inversion formula for the FBG case was first derived by Herman and Naparstek[14] and is given by,

$$\tilde{f}(r,\phi) = \frac{1}{4\pi^2} \int_0^{2\pi} \int_{-B}^{B} (1/\sin(\sigma' - \sigma)) D_v g(\sigma,\beta)\, d\sigma\, d\beta \tag{2.12}$$

where,

D = distance of source from reference origin,

σ = angle of the data–ray with the reference ray,

B = angle of the extreme data rays, β = source position,

$g(\sigma,\beta)$ = data for the ray represented by (σ,β),

$D_v = (1/U)(\partial/\partial\sigma - \partial/\partial\beta)$,

$\sigma' = \tan^{-1}[(r\cos(\beta-\phi))/(D + r\sin(\beta-\phi))]$,

$U = [(r\cos(\beta-\phi))^2 + (D + r\sin(\beta-\phi))^2]^{1/2}$,

and the remaining variables are same as for the PBG case (see Fig.(2.1). In the above equations U is the distance of the radiation source from (r, ϕ), the point being reconstructed ,and σ' is the angular displacement of the particular data ray passing through that point (r, ϕ). A major difference (compared to Eq.(2.7), which derives the reconstruction formula for parallel beam geometry) is the computation of partial derivatives of the data, g.

2.3 Convolution Back–Projection Algorithm

Reconstruction algorithms based on the inversion formulae are called 'transform methods'[15]. They are slow and require accurate interpolating schemes in computing the two-dimensional inverse Fourier transform. The introduction of convolution[4,5] eliminated the use of the Fourier transform and its inversion. For PBG , Eq.(2.8) can be written as

$$\tilde{f}(r, \phi) = \int_0^{\pi} \int_{-R}^{R} p(s; \theta)\, q(s' - s)\, ds\, d\theta, \tag{2.13}$$

where

$$q(s) = \int_{-A}^{A} W(F)\, |F|\, \exp(i2\pi F s)\, dF, \tag{2.14}$$

and $s' = r\cos(\theta - \phi)$.

Here q is known as the convolving function and is the inverse Fourier transform of the function, $W(F)\,|F|$, where $W(F)$ is the filter function. The inner integral of Eq.2.12) is a convolution and the outer integral is called the back-projection. The CBP algorithm is the most widely used method of reconstruction employed by commercial CT scanners used in the area of medical imaging.

Chapter 3

Program Implementation and Description

The CBP algorithm was used for reconstruction of 10 images and the error was calculated for each image for different no. of rays. The band limiting filter used for the image reconstruction was Ramchandran filter.

3.1 Computer Implementation of the CBP Algorithm

The problem of reconstruction from projections is to find $f(x, y)$ from the given value of $p(s; i)$. In practice, the problem may be stated as :

Given discrete projection data in the form of estimates of p for a finite number of rays, find a 2-D distribution, which is a reconstructed estimate of the unknown object.

In the case when p is sampled uniformly in both s and θ, for N angles $\Delta\theta$ apart,

with each view having M equispaced rays Δs apart, we define[15]

$$\left.\begin{aligned} M^+ &= (M-1)/2 \\ M^- &= -(M-1)/2 \end{aligned}\right\} \quad M \text{ odd} \tag{3.1}$$

$$\left.\begin{aligned} M^+ &= (M/2)-1 \\ M^- &= -M/2 \end{aligned}\right\} \quad M \text{ even} \tag{3.2}$$

In order to ensure that the collection of rays specified by

$$\left\{(m\Delta s, n\Delta\theta)\colon M^+ \le m \le M^-, \quad 1 \le n \le N\right\}$$

covers the unit circle, we have,

$$\Delta\theta = \pi/N \qquad \Delta s = 1/M^+. \tag{3.3}$$

A reconstruction algorithm which can be implemented on the digital computer is required to evaluate $f_B(k\Delta x, l\Delta y)$, which is a band limited approximation of the function to be reconstructed. Here $K^- \le k \le K^+$ and $L^- \le l \le L^+$, where k and l are the positions of the co-ordinates of the image pixel. The definition of their upper and lower limits is similar to that of 'm'. Thus the projected data from N views and M rays is to be used to construct an image of $K \times L$ pixels. The back-projection integral is evaluated as follows :

$$f_B(k\Delta x, l\Delta y) \simeq \Delta\theta \sum_{n=1}^{N} \dot{p}(f_B(k\Delta x \cos\theta_n + l\Delta y \sin\theta_n, \theta_n) \tag{3.4}$$

For each angle θ_n, the convolved values of $p(s', \theta_n)$ for the $K \times L$ values of s', we can either have a separate convolution for every s' with the actual value of $q(s' - m\Delta s)$ at that point or we can evaluate $\dot{p}(m\Delta s, \theta_n)$ only within the specified limits of m and then use interpolation. The latter approach is much faster and cheaper. These

operations are represented by

$$p_c(m'\Delta s, \theta_n) \simeq \Delta s \sum_{m=M^-}^{M^+} p(m\Delta s, \theta_n)\, q\left((m'-m)\right), \quad M^- \leq m \leq M^+ \tag{3.5}$$

$$p_I(s', \theta_n) \simeq \Delta s \sum_{m'} p(m\Delta s, \theta_n)\, I\left(s' - m\Delta s\right) \tag{3.6}$$

where $I(s)$ is an interpolating function. A linear interpolating function, say $I_L(s)$, corresponding to linear interpolation between adjacent samples is

$$I_L(s) = \begin{cases} \frac{1}{\Delta s}(1 - |s|/\Delta s), & |s| \leq \Delta s \\ 0, & |s| \leq \Delta s \end{cases} \tag{3.7}$$

The other popular scheme is nearest neighbour interpolation. Both of them give satisfactory results. The choice depend on the information required by the usercite-herman.

3.2 Errors Involved in Tomographic Inversion

Implementation of CBP algorithm involves various errors, which can be categorized as inherent error and discretization error. The error estimation for tomographic inversion is discussed in detail by Munshi et al.[16].

3.2.1 Inherent error

The inherent error is given by

$$e_R = f(r, \phi) - \hat{f}(r, \phi) \tag{3.8}$$

where $f(r, \phi)$ and $\hat{f}(r, \phi)$ are given by equation 2.6 and 2.8. $\hat{f}(r, \phi)$ represents approximation of $f(r, \phi)$. This error arises due to finite cut-off of the Fourier frequency.

This error is precisely zero if the function $f(r,\phi)$ happens to have a band limited projection data, and cut-off frequency is chosen such that it is at least equal to the largest frequency contained in f, and $w(R) = 1$, in the limit $[-R_c, R_c]$.

3.2.2 Discretization error

The data obtained for reconstruction are not continuous, but discrete. This causes error in the implementation of algorithm due to discretization of convolution and back projection integral.

The total error in the reconstruction, e_T at any point can be given as sum of the two aforesaid errors, at that point.

$$e_T = e_R + e_D \tag{3.9}$$

The errors involved in the reconstruction of the simulated images are represented in the following manner :

$$\begin{aligned} ERMIN &= \min(\tilde{f} - f) \\ ERMAX &= \max(\tilde{f} - f) \\ ERL1 &= \frac{1}{MP}\sum_i\sum_j\left|(\tilde{f}_{ij} - f_{ij})\right| \\ ERL2 &= \frac{1}{MP}\left[\sum_i\sum_j\left|(\tilde{f}_{ij} - f_{ij})\right|^2\right]^{1/2} \\ E &= \frac{1}{NP}\sum_i\sum_j\left|\tilde{f}_{ij}^{CD} - f_{ij}^{CD}\right| \end{aligned} \tag{3.10}$$

Here,

MP represents the total number of pixels considered for evaluation of ERL1 and ERL2,

NP represents the total number of pixels considered for evaluation of E

and, superscript CD implies the value of the function after the 32 gray level coding.

The errors, $ERL1$ and $ERL2$ represent the usual l_1 and l_2 errors. The error $\overline{E}$ represents an index of visual quality of the reconstructed image. For a given window and fixed cutoff frequency R_c, $ERMIN$ and $ERMAX$ give an indication of smoothness of the function concerned.

The normalized errors corresponding to $ERL1$, $ERL2$, and $\overline{E}$ are defined as follows:

$$\begin{aligned} ERL1N &= \frac{(ERL1)\,(MP)}{\Sigma_i \Sigma_j |f_{ij}|} \\ ERL2N &= \frac{(ERL2)\,(MP)}{\left[\Sigma_i \Sigma_j \left|f_{ij} - \bar{f}\right|^2\right]^{1/2}} \\ \overline{EN} &= \frac{(\overline{E})\,(NP)}{\Sigma_i \Sigma_j \left|f_{ij}^{CD}\right|} \end{aligned} \tag{3.11}$$

Here, $\bar{f}$ denotes the function value averaged over the entire region of interest.

Chapter 4

Results and Discussion

This chapter deals with the data i.e. images used for reconstruction and the errors obtained on implementation of the CBP algorithm.

4.1 Data Used

The simulated images used for reconstruction are listed in Table 4.1. These images use a 32 gray level scheme to denote the density at different points. The original images are shown in Figs. 4.1– 4.3.

4.2 Results

Reconstructed images for different number of rays are shown in the appendix. The various errors i.e. average errors l_1, l_2, $ERMAX$, and $ERMIN$ are displayed in the Tables 4.2 – 4.5 for different number of rays. The plots depicting variation of $ERMAX$ and $ERMIN$ with Fourier frequency are shown in Figs. 4.4 – 4.23 and in the Appendix–B. The reconstructions with varying R_c indicate that error reduces in a linear fashion. It can be seen that order of e_T is $O(1/R_c)$.

4.3 Discussion

As it is expected, the total error seems to be decreasing with the increase in number of rays. The total error consists of inherent error and discretization error. Both the errors are coupled, as the Fourier cut-off frequency is related to the number of rays. The nature of the curves obtained between error and Fourier frequency gives a fair reflection that the error decreases at a faster pace initially, and after a Fourier frequency value 64, the error decreases at a slower rate. Although, quantitatively it is difficult to make any conclusive remark, yet qualitatively it can be very well said that the error curves have two distinct regions. The first region has drooping kind of characteristic. Whereas the second region shows a linear decrease in the error values. The least squares fit for the higher Fourier frequency versus error is also shown in the plots (Figs. 4.4 – 4.23). This characteristic seems to be in tune with the theoretical predictions reported by Natterer[17] and Munshi[9].

Table 4.1: List of images used for reconstruction

Sl. No.	*Image*	*Image Key*
1	SAT	V
2	LIN	W
3	FIN	X
4	GIN	Y
5	JET	A
6	CRO	B
7	THO	C
8	TST	D
9	BRN	E
10	PIC	Z
11	IND	N

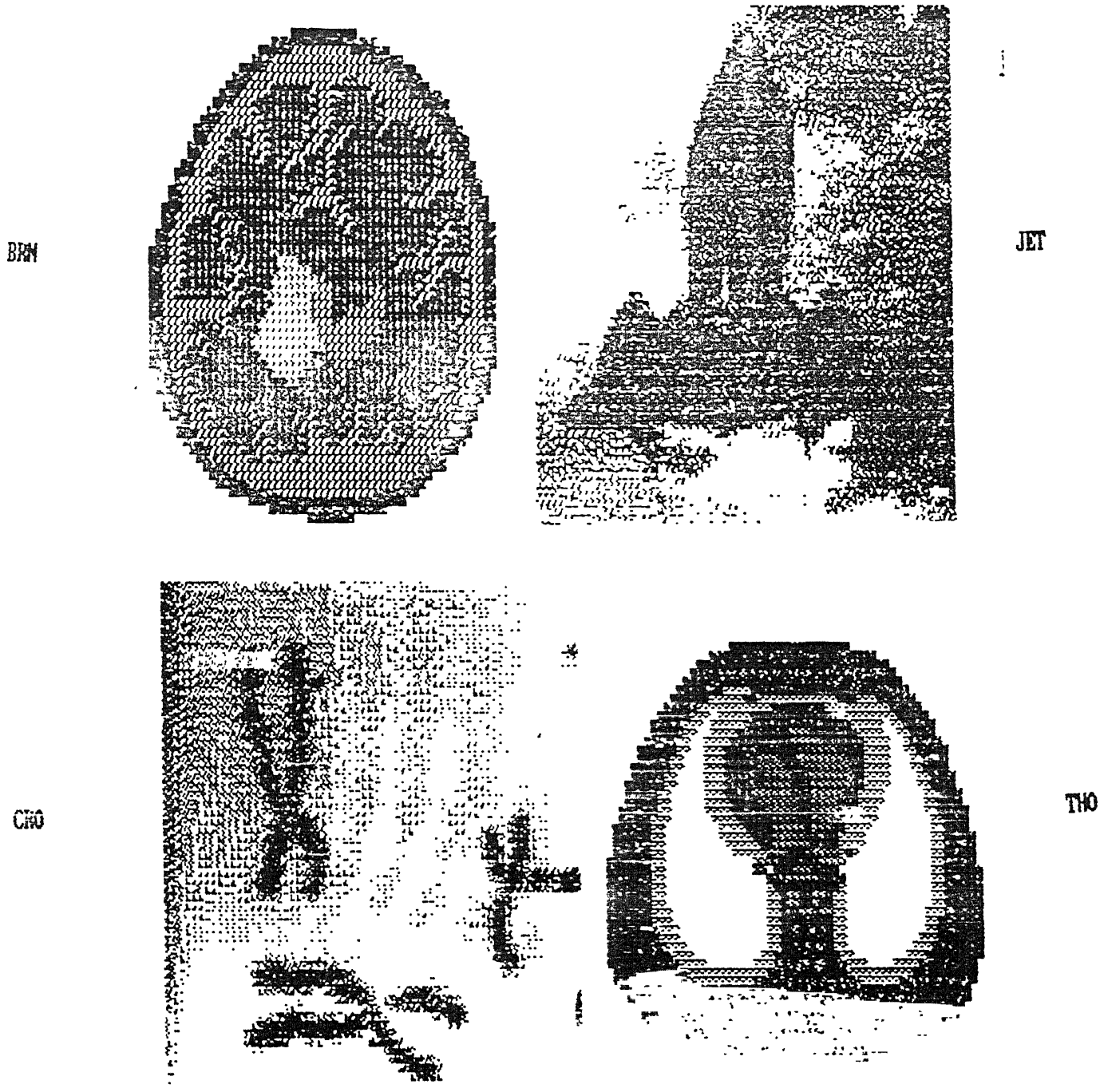

Figure 4.1: Original simulation of BRN, JET, CRO and THO

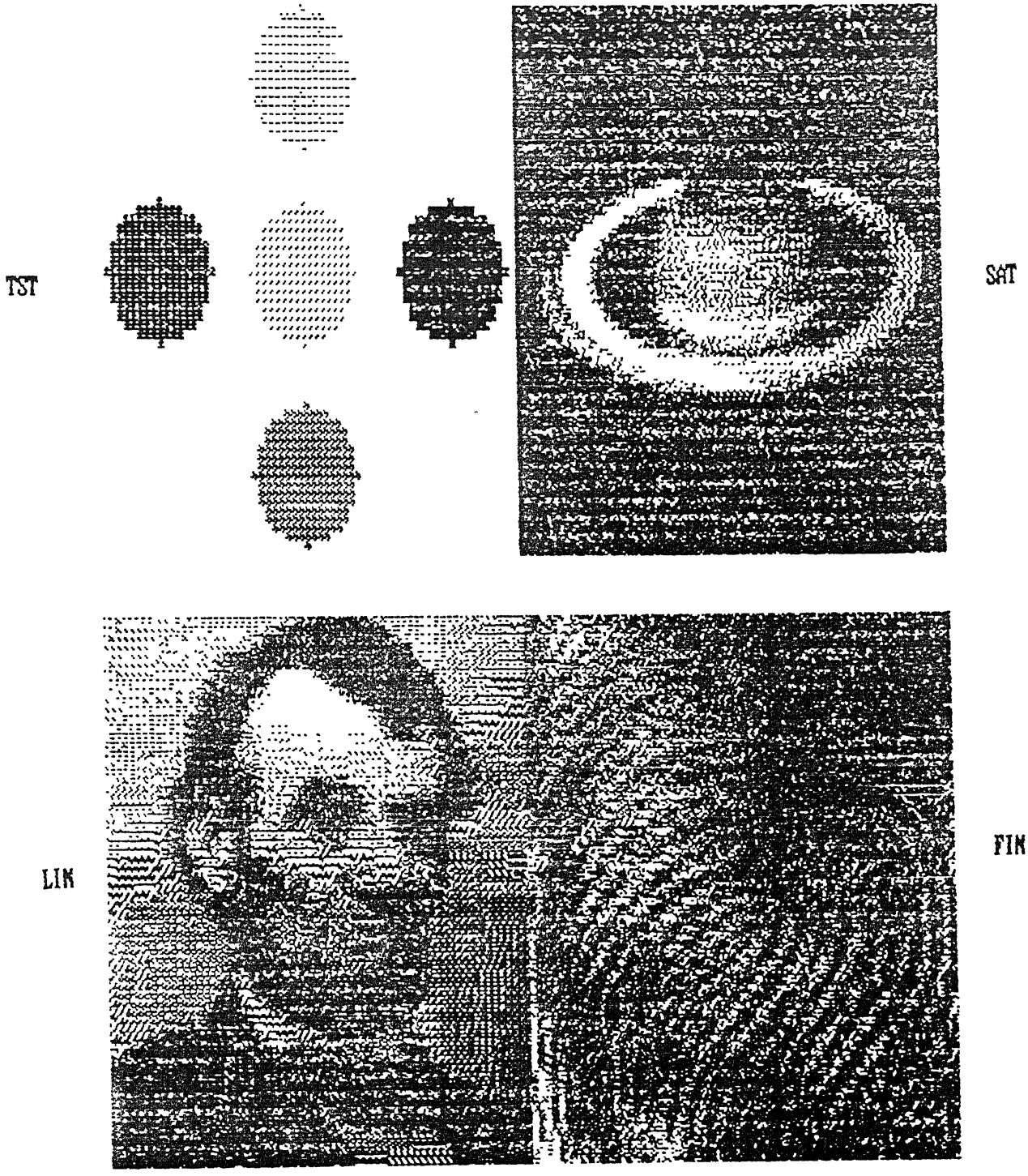

Figure 4.2: Original simulation of TST, SAT, LIN and FIN

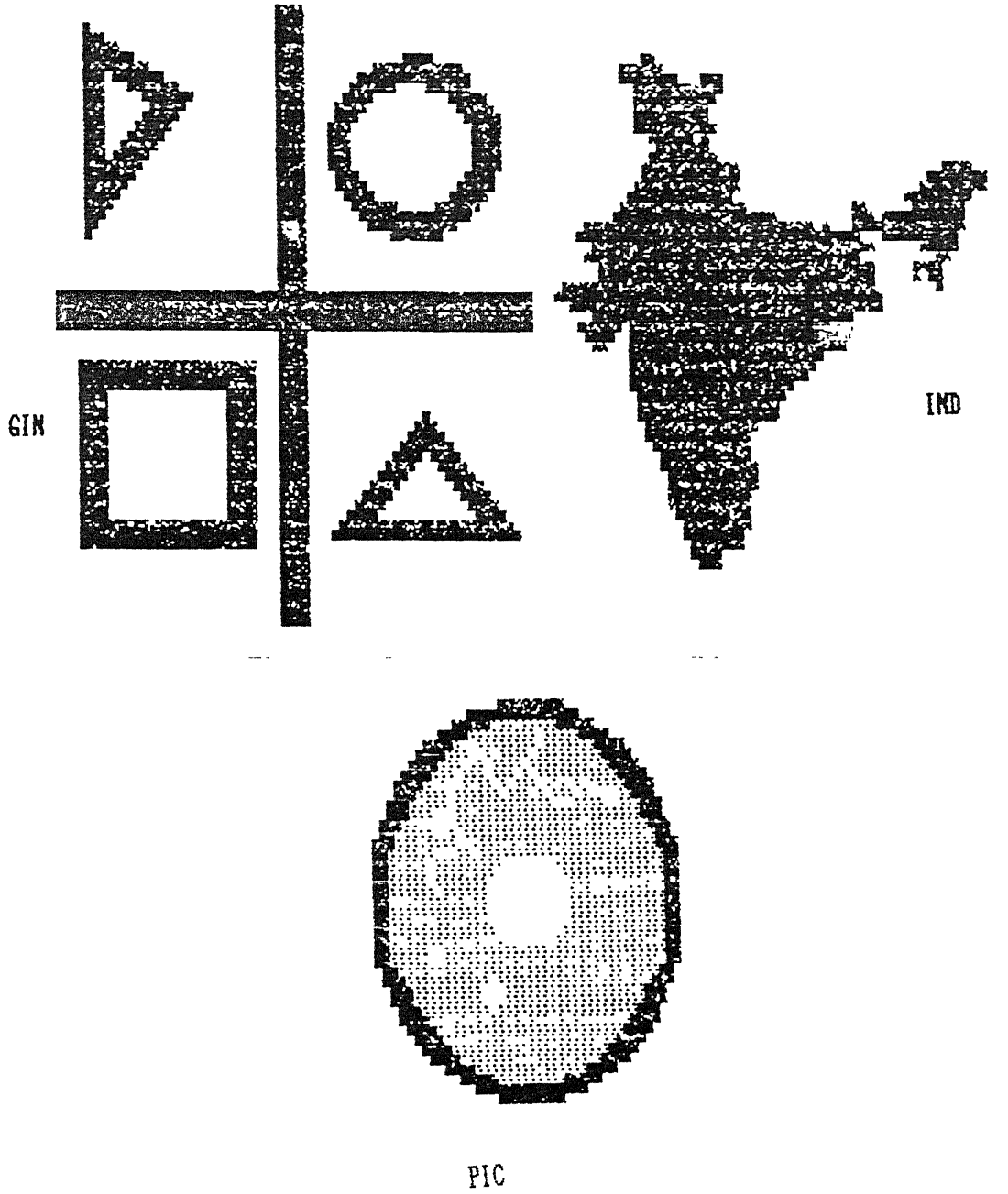

Figure 4.3: Original simulation of GIN, IND and PIC

Table 4.2: Summary of errors in reconstruction of images SAT, LIN and FIN

Image Name	*Image Code*	*NRAY*	*ERMIN*	*ERMAX*	ERL_1	ERL_2
SAT	V–1	64	-5.3244	4.8050	1.1386	1.4398
	V–2	128	-2.1813	1.9667	0.3678	0.4875
	V–3	256	-1.0952	1.0670	0.1632	0.2303
	V–4	512	-0.5420	0.5735	0.1106	0.1384
	V–5	1024	-0.1210	0.4017	0.1563	0.1631
LIN	W–1	64	-5.0369	4.3424	0.8991	1.1740
	W–2	128	-2.0879	2.1520	0.3137	0.4264
	W–3	256	-1.0424	1.1817	0.1362	0.1932
	W–4	512	-0.4148	0.6560	0.0889	0.1141
	W–5	1024	-0.1308	0.3845	0.1210	0.1309
FIN	X–1	64	-7.3287	9.7300	1.6054	2.0348
	X–2	128	-3.1491	2.6086	0.6067	0.7524
	X–3	256	-1.3809	1.2625	0.2784	0.3435
	X–4	512	-0.4684	0.6519	0.1439	0.1791
	X–5	1024	-0.1489	0.4301	0.1383	0.1591

Table 4.3: Summary of errors in reconstruction of images GIN, JET and CRO

Image Name	*Image Code*	*NRAY*	*ERMIN*	*ERMAX*	ERL_1	ERL_2
GIN	Y–1	64	-11.8286	12.6952	1.9095	2.5491
	Y–2	128	-05.2623	03.3543	0.6273	0.8680
	Y–3	256	-01.8502	01.8295	0.2644	0.3980
	Y–4	512	-00.7914	00.8206	0.1300	0.1933
	Y–5	1024	-00.3833	00.4918	0.1101	0.1408
JET	A–1	64	-9.1101	7.4484	1.0398	1.3839
	A–2	128	-2.8679	3.3377	0.3538	0.4990
	A–3	264	-0.8881	1.4410	0.1522	0.2202
	A–4	512	-0.3940	0.8061	0.0876	0.1205
	A–5	1024	-0.1078	0.5027	0.1048	0.1205
CRO	B–1	64	-5.6963	4.4814	0.7492	0.1008
	B–2	128	-2.4807	2.2000	0.2720	0.3913
	B–3	256	-1.1586	0.7974	0.1214	0.1762
	B–4	512	-0.5655	0.4923	0.0614	0.0874
	B–5	1024	-0.2486	0.2294	0.0469	0.0581

Table 4.4: Summary of errors in reconstruction of images THO, TST and BRN

Image Name	*Image Code*	*NRAY*	*ERMIN*	*ERMAX*	ERL_1	ERL_2
THO	C–1	64	-7.1519	7.2522	1.3028	1.7130
	C–2	128	-2.9083	2.4679	0.4409	0.6041
	C–3	256	-1.3023	1.4420	0.1951	0.2768
	C–4	512	-0.8100	0.6728	0.1047	0.1441
	C–5	1024	-0.3289	0.4173	0.1012	0.1153
TST	D–1	64	-6.7023	5.1341	0.7994	1.0601
	D–2	128	-3.6107	2.6479	0.2243	0.3767
	D–3	256	-1.7692	1.1559	0.0912	0.1752
	D–4	512	-0.7808	0.5594	0.0437	0.0836
	D–5	1024	-0.3132	0.3327	0.0368	0.0523
BRN	E–1	64	-8.4734	9.7270	1.4381	1.9822
	E–2	128	-2.7575	5.1121	0.5012	0.7097
	E–3	264	-2.2170	1.5601	0.2367	0.3461
	E–4	512	-0.7367	0.8860	0.1267	0.1733
	E–5	1024	-0.2460	0.4655	0.1282	0.1437

Table 4.5: Summary of errors in reconstruction of images PIC and IND

Image Name	*Image Code*	*NRAY*	*ERMIN*	*ERMAX*	ERL_1	ERL_2
PIC	Z–1	64	-9.7068	9.7919	1.0897	1.7531
	Z–2	128	-2.6595	2.6963	0.3678	0.6124
	Z–3	264	-1.1953	1.2619	0.1581	0.2841
	Z–4	512	-0.8794	0.7108	0.0729	0.1346
	Z–5	1024	-0.3026	0.3683	0.0489	0.0747
IND	N–1	64	-8.7730	8.3720	1.5107	1.9961
	N–2	128	-3.6732	3.9831	0.4918	0.7304
	N–3	264	-1.8676	1.9215	0.2311	0.3411
	N–4	512	-0.7342	1.1708	0.1129	0.1706
	N–5	1024	-0.3726	0.6003	0.1019	0.1227

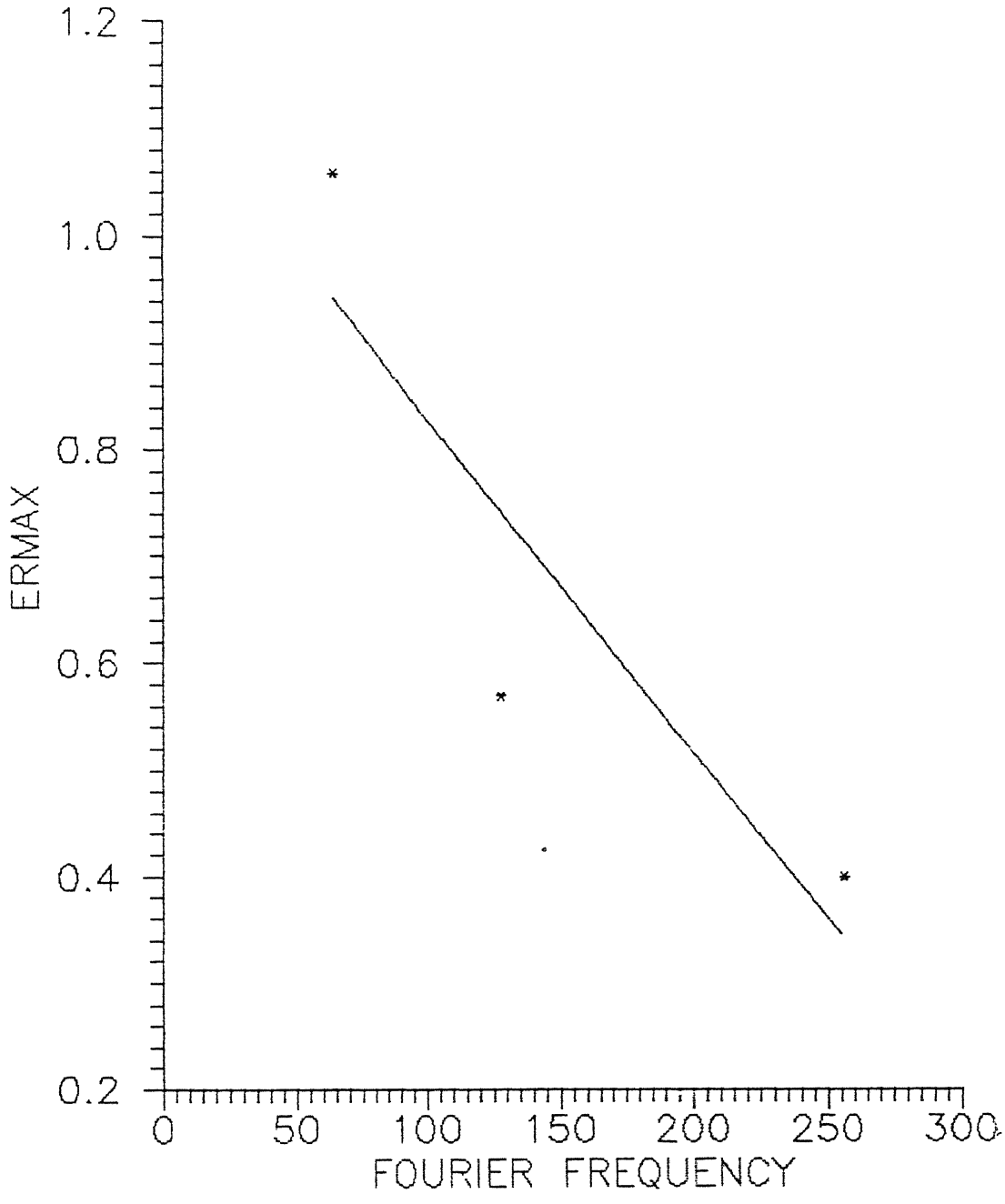

Figure 4.4: Maximum error variation at higher frequencies for SAT

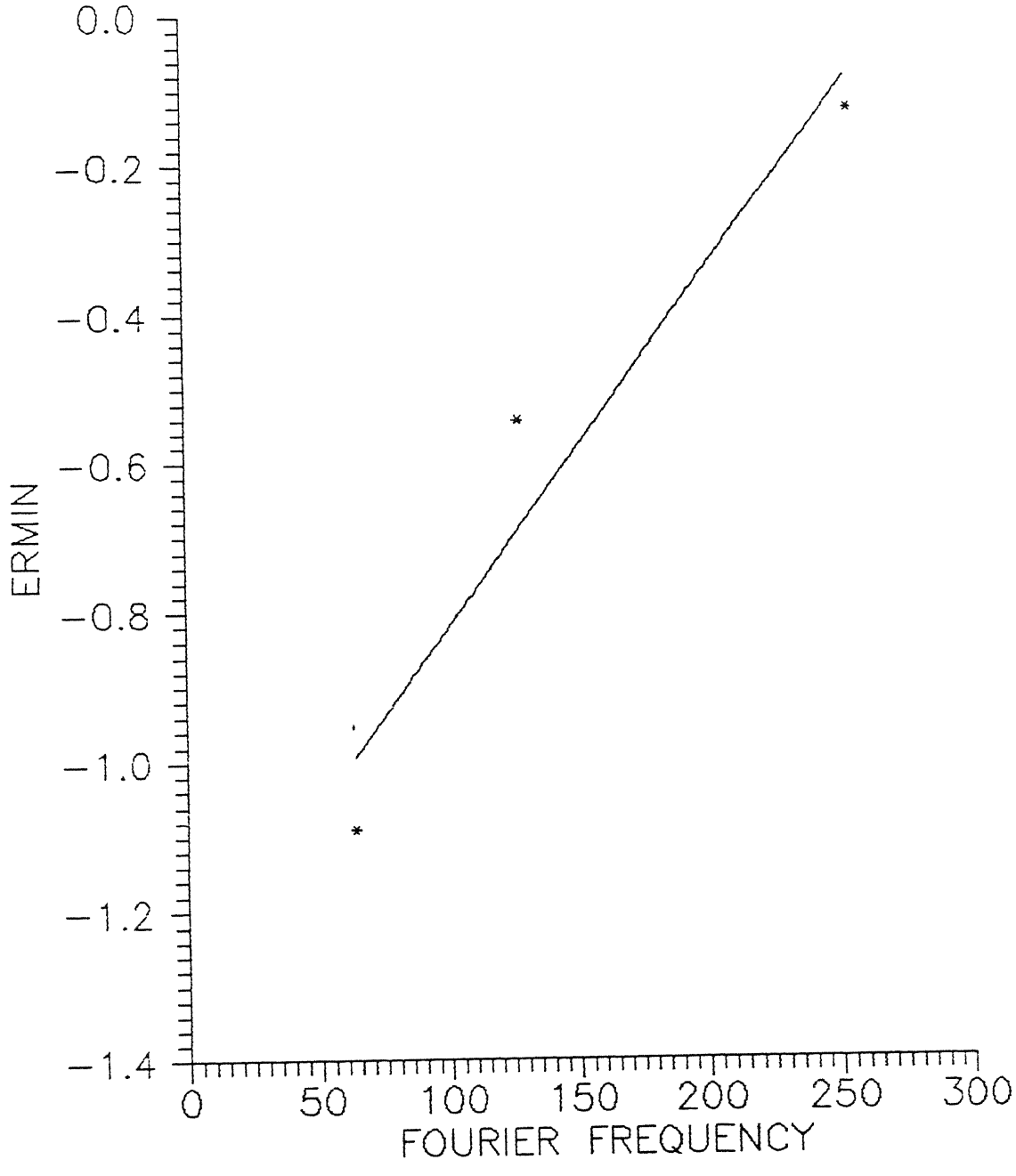

Figure 4.5: Minimum error variation at higher frequencies for SAT

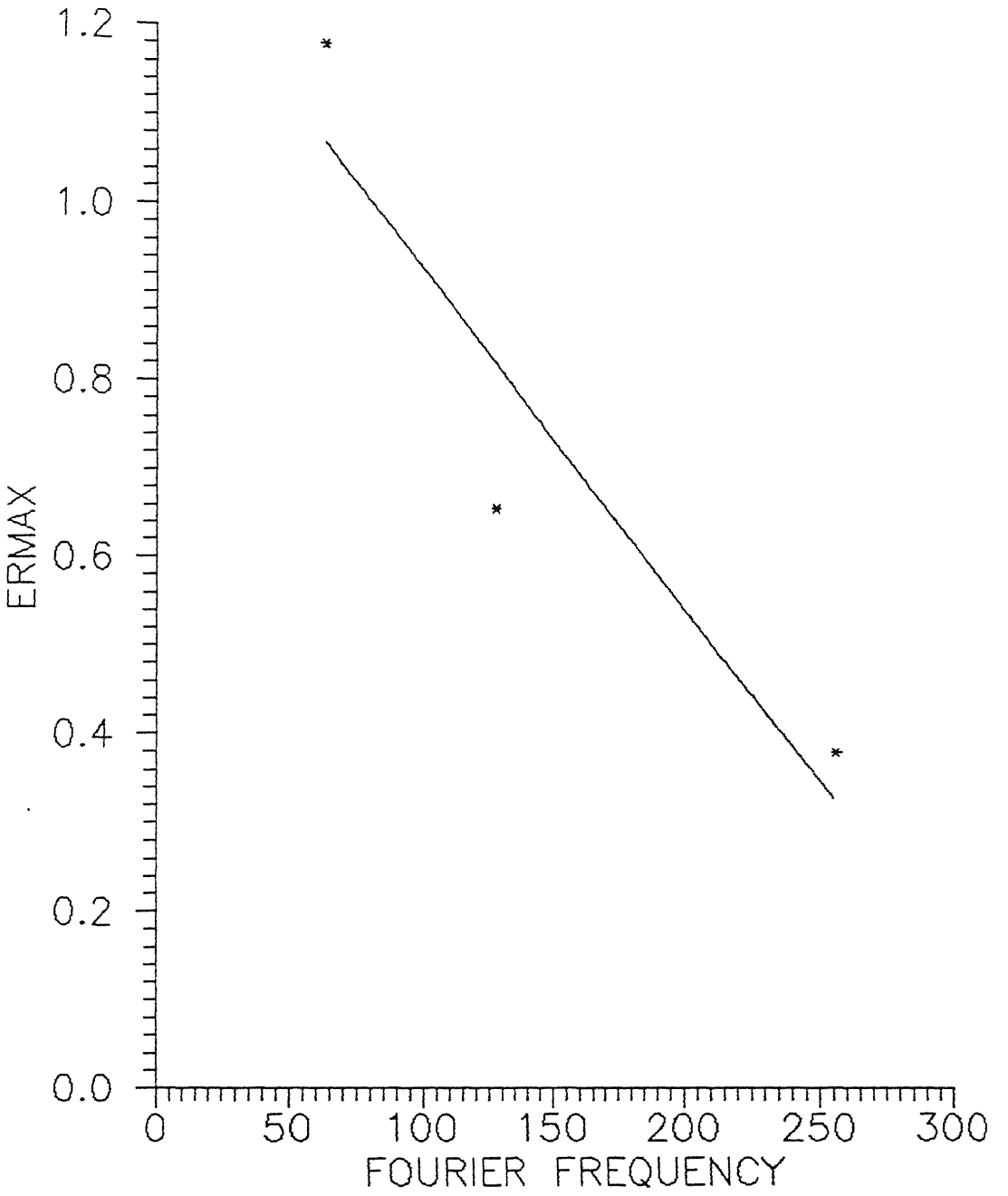

Figure 4.6: Maximum error variation at higher frequencies for LIN

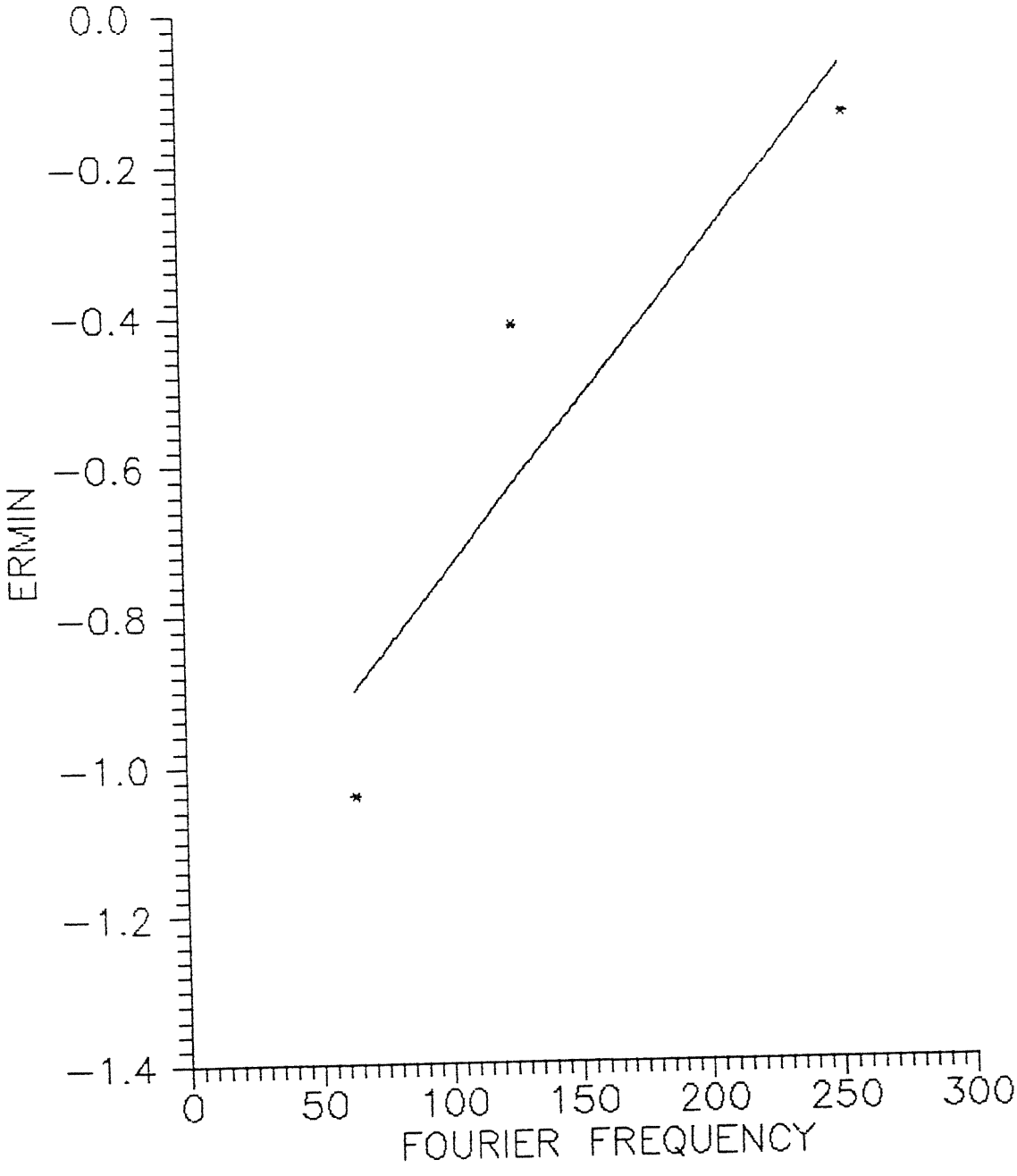

Figure 4.7: Minimum error variation at higher frequencies for LIN

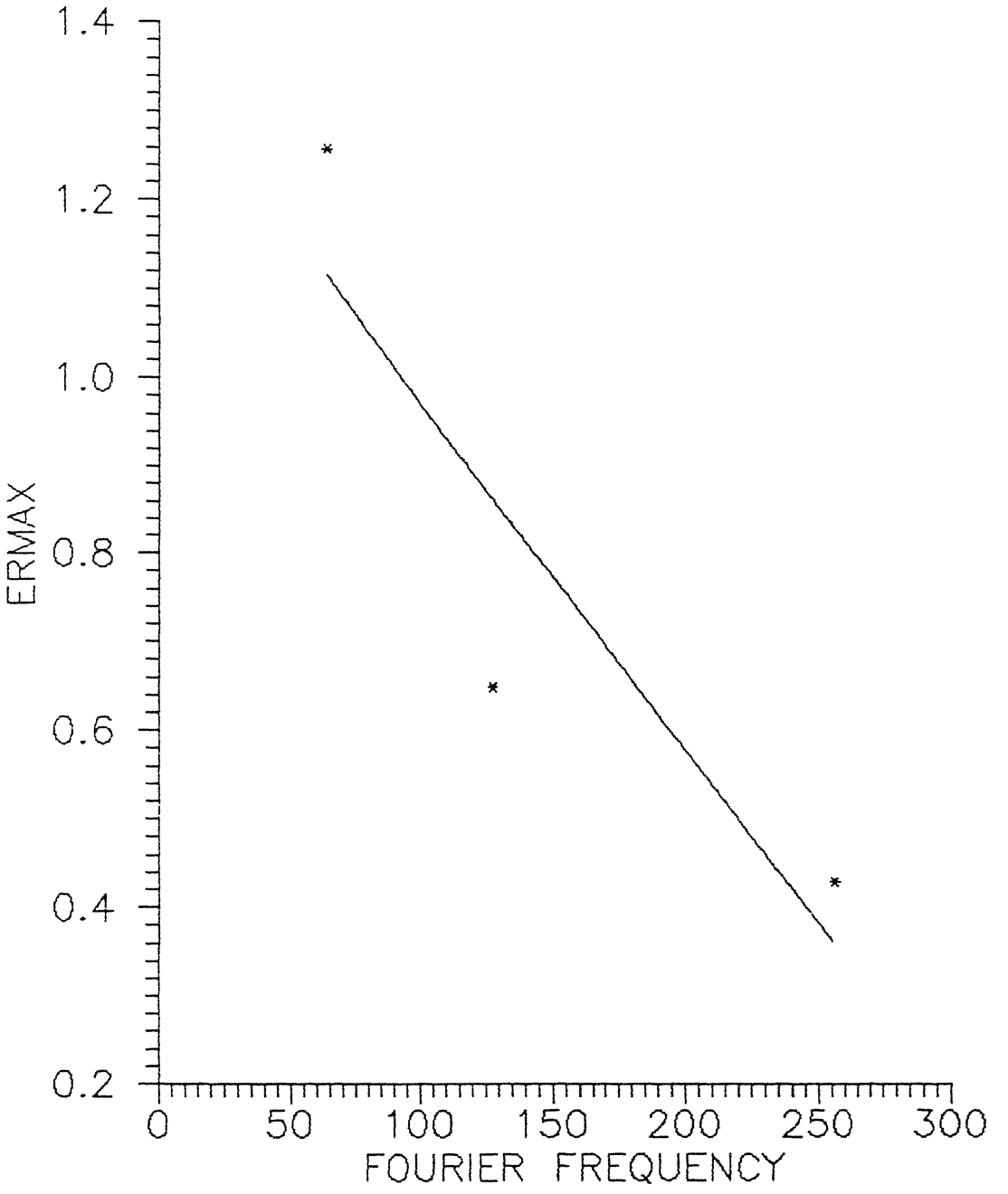

Figure 4.8: Maximum error variation at higher frequencies for FIN

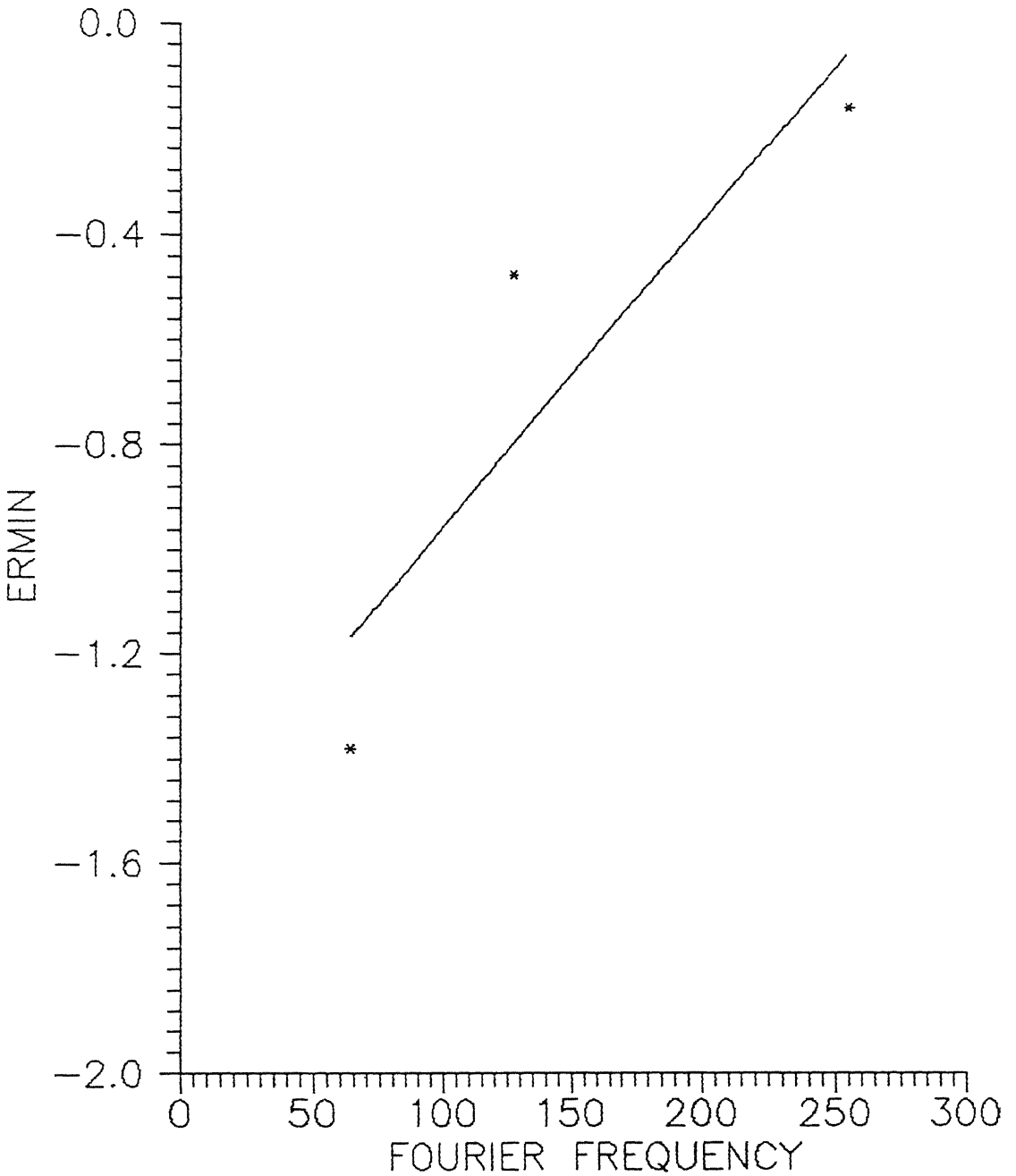

Figure 4.9: Minimum error variation at higher frequencies for FIN

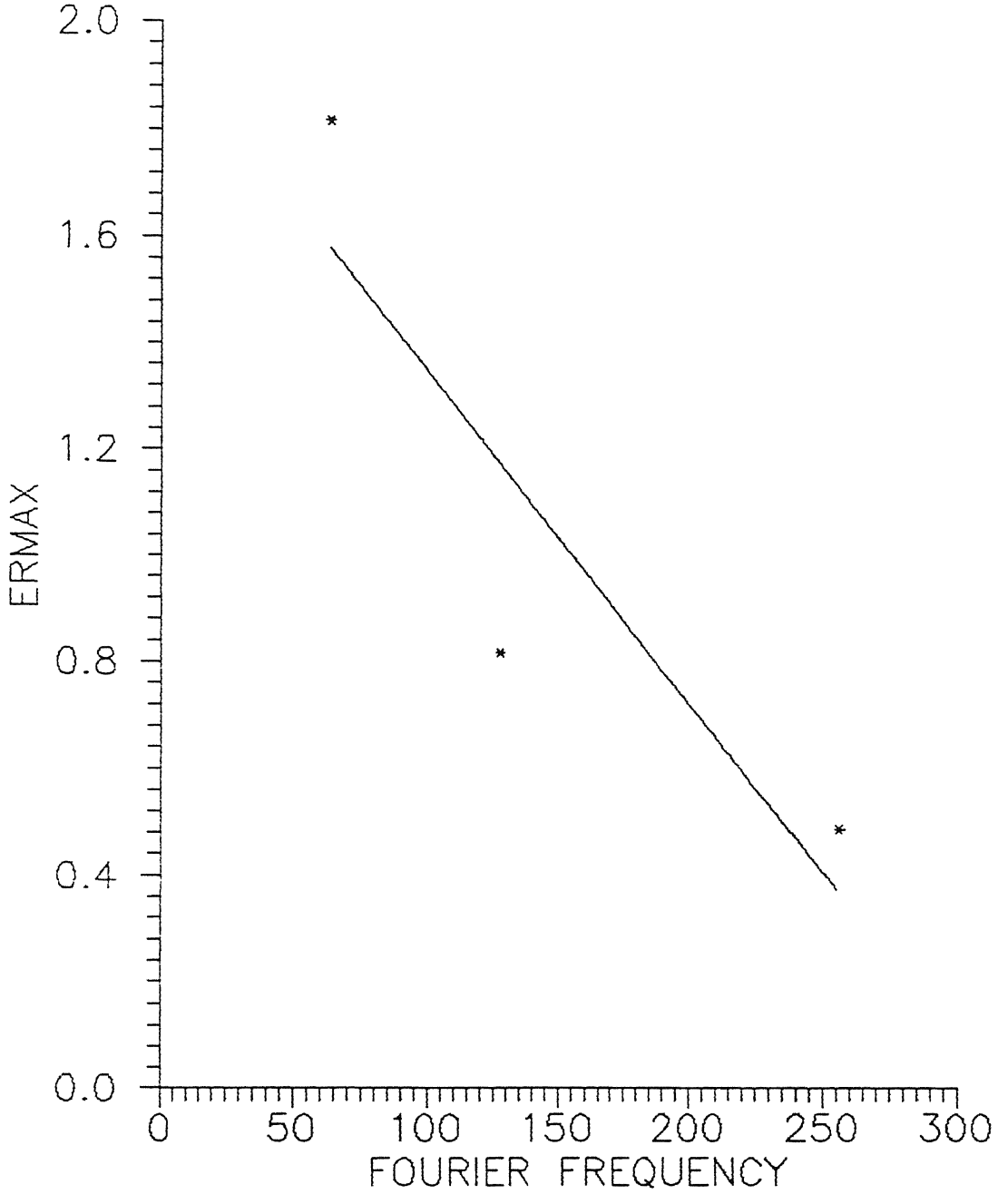

Figure 4.10: Maximum error variation at higher frequencies for GIN

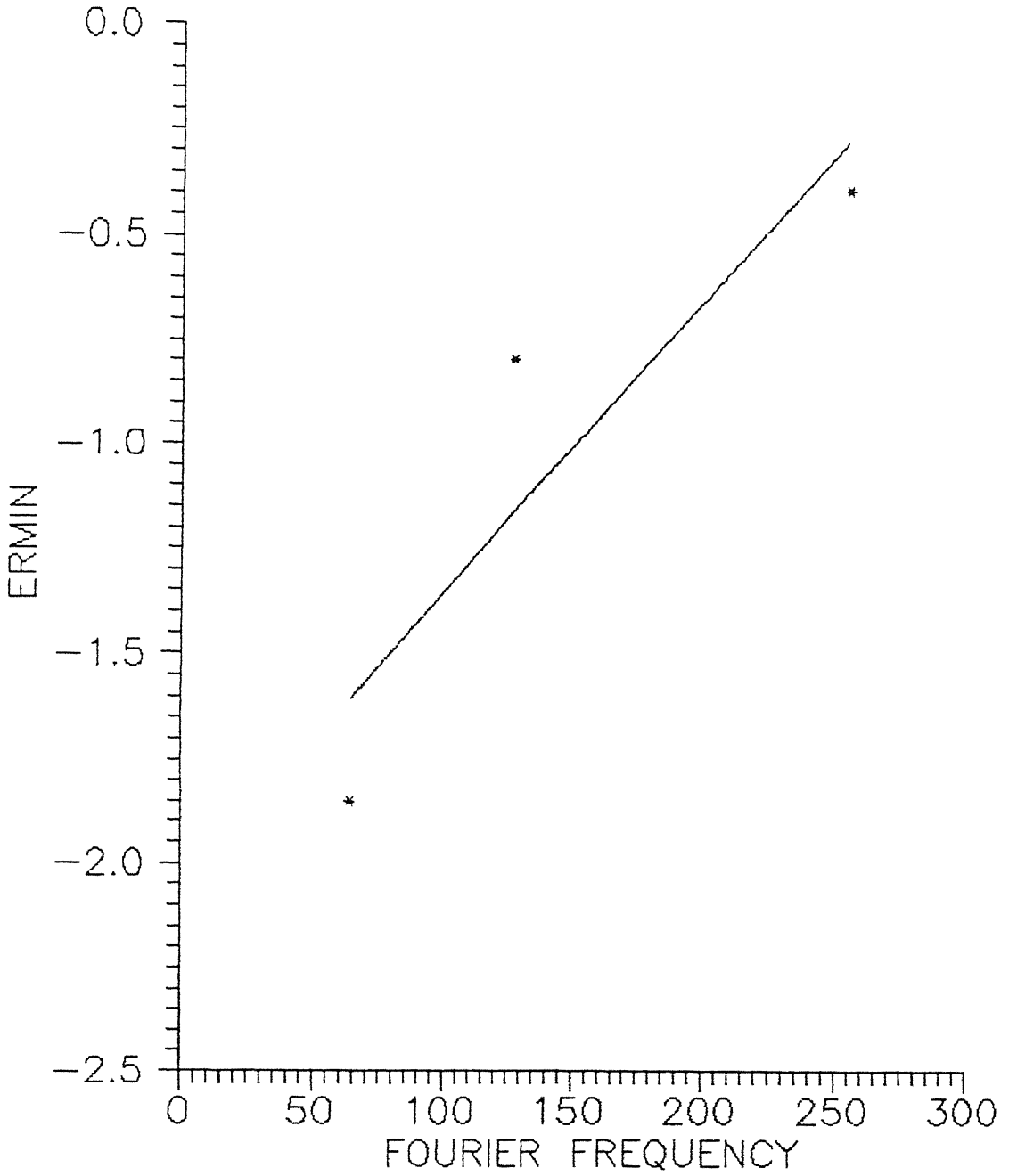

Figure 4.11: Minimum error variation at higher frequencies for GIN

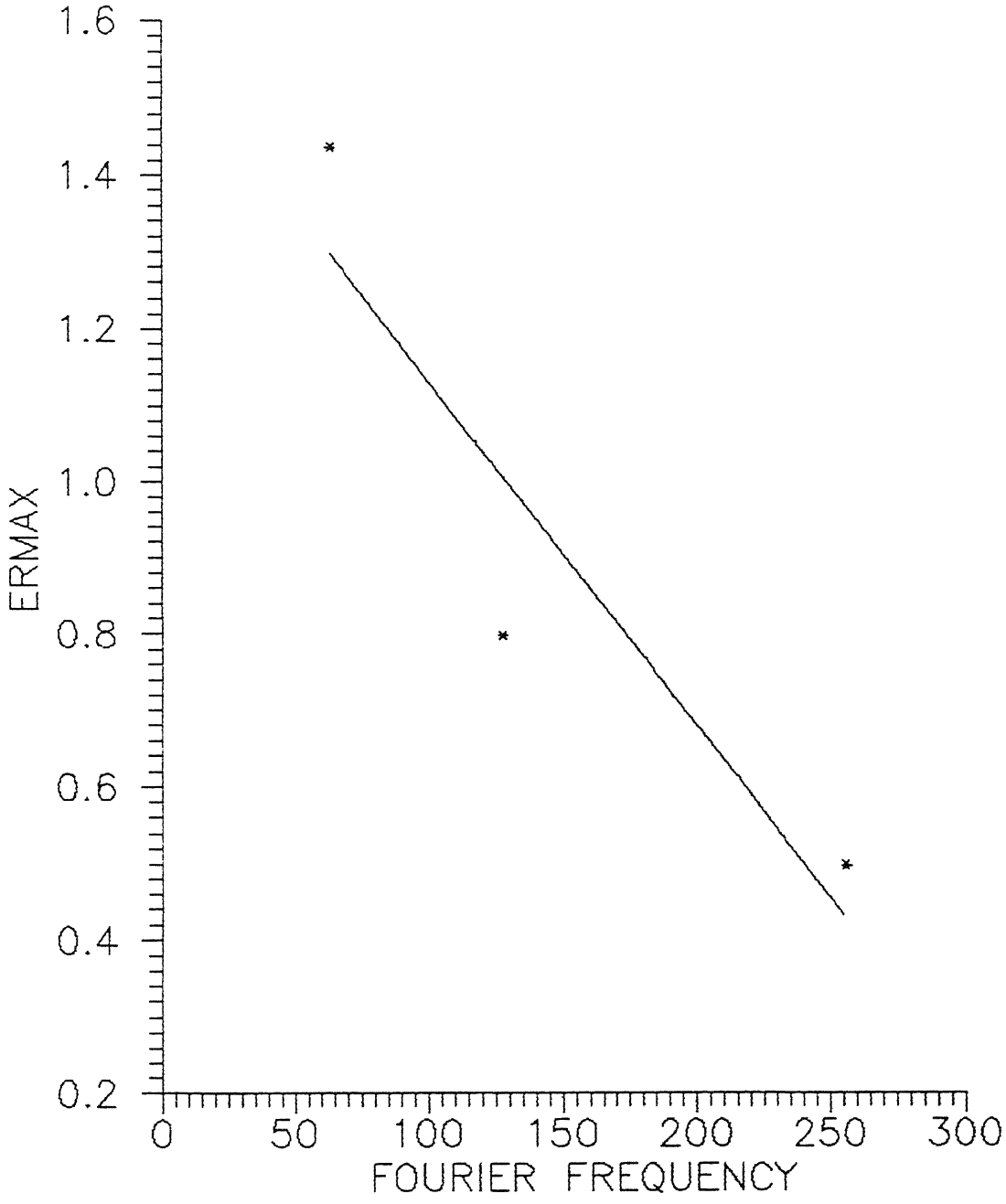

Figure 4.12: Maximum error variation at higher frequencies for JET

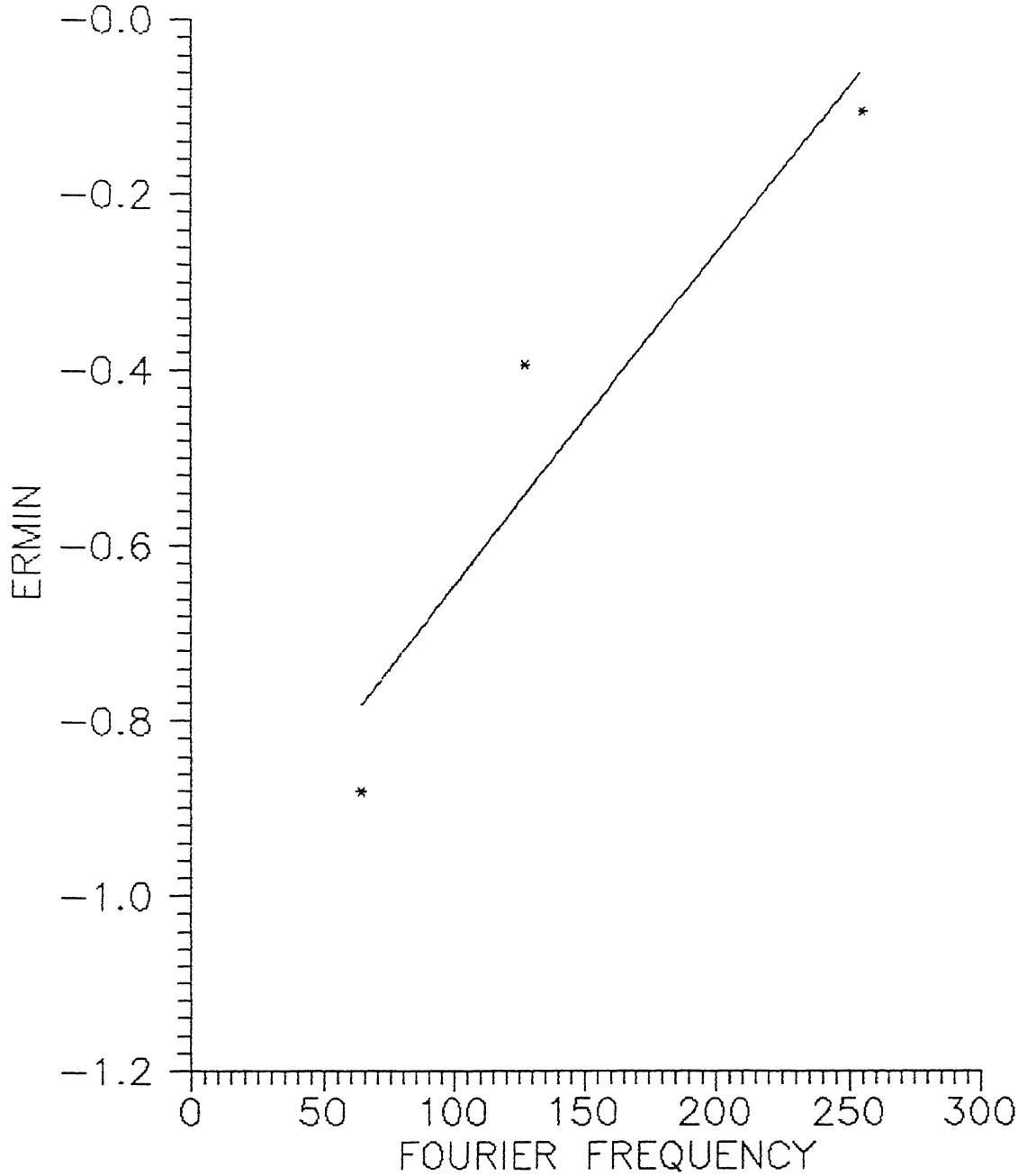

Figure 4.13: Minimum error variation at higher frequencies for JET

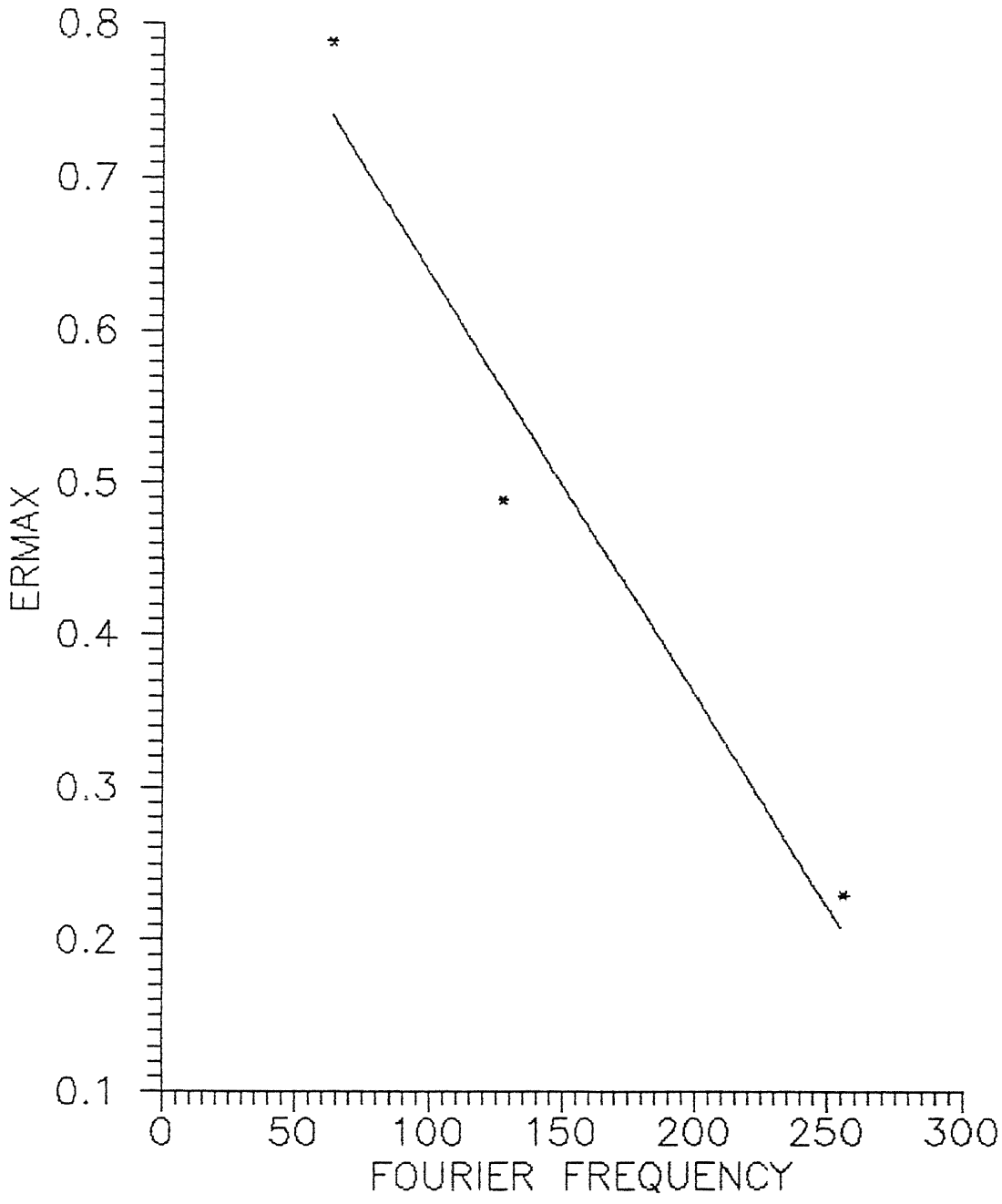

Figure 4.14: Maximum error variation at higher frequencies for CRO

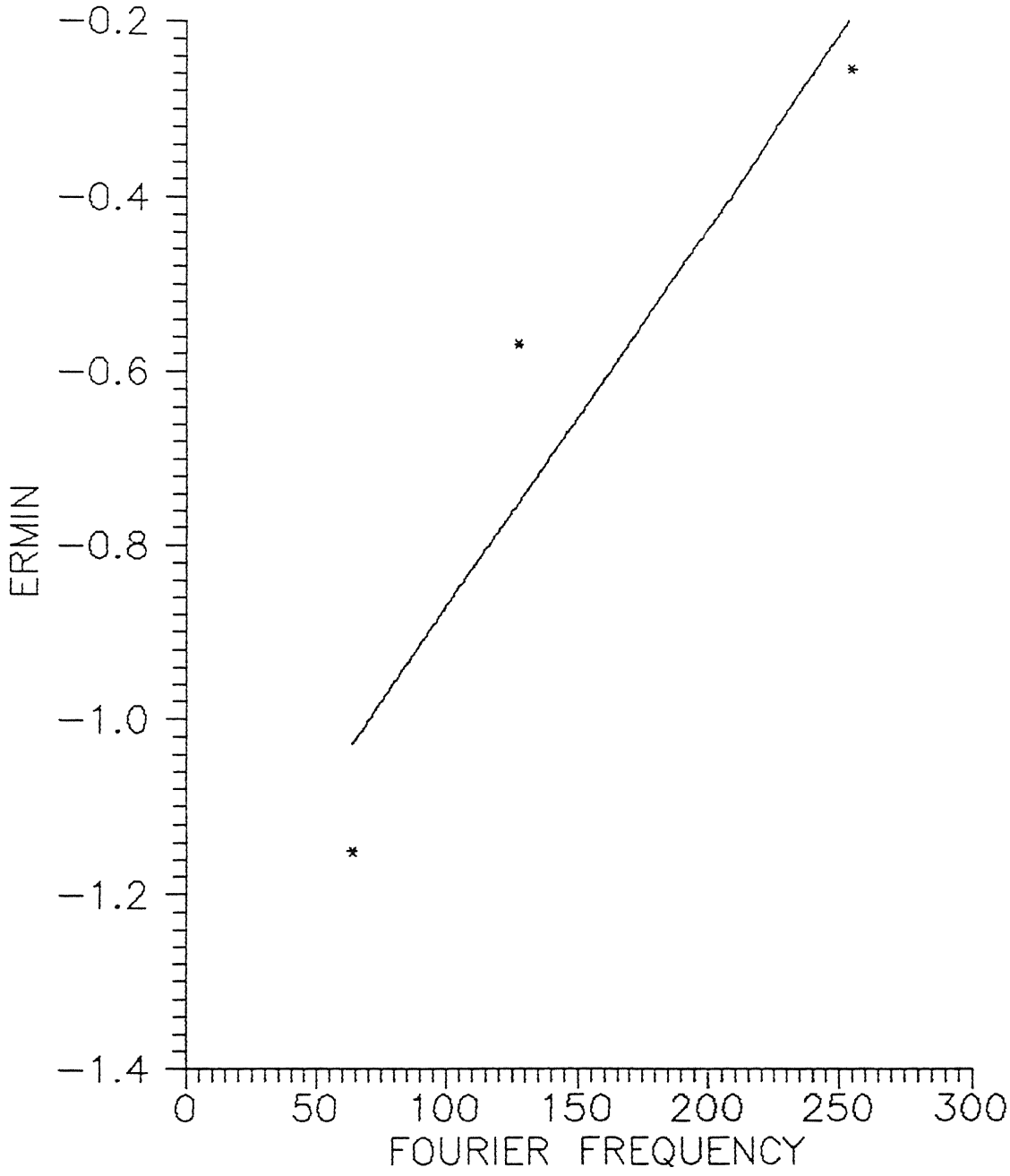

Figure 4.15: Minimum error variation at higher frequencies for CRO

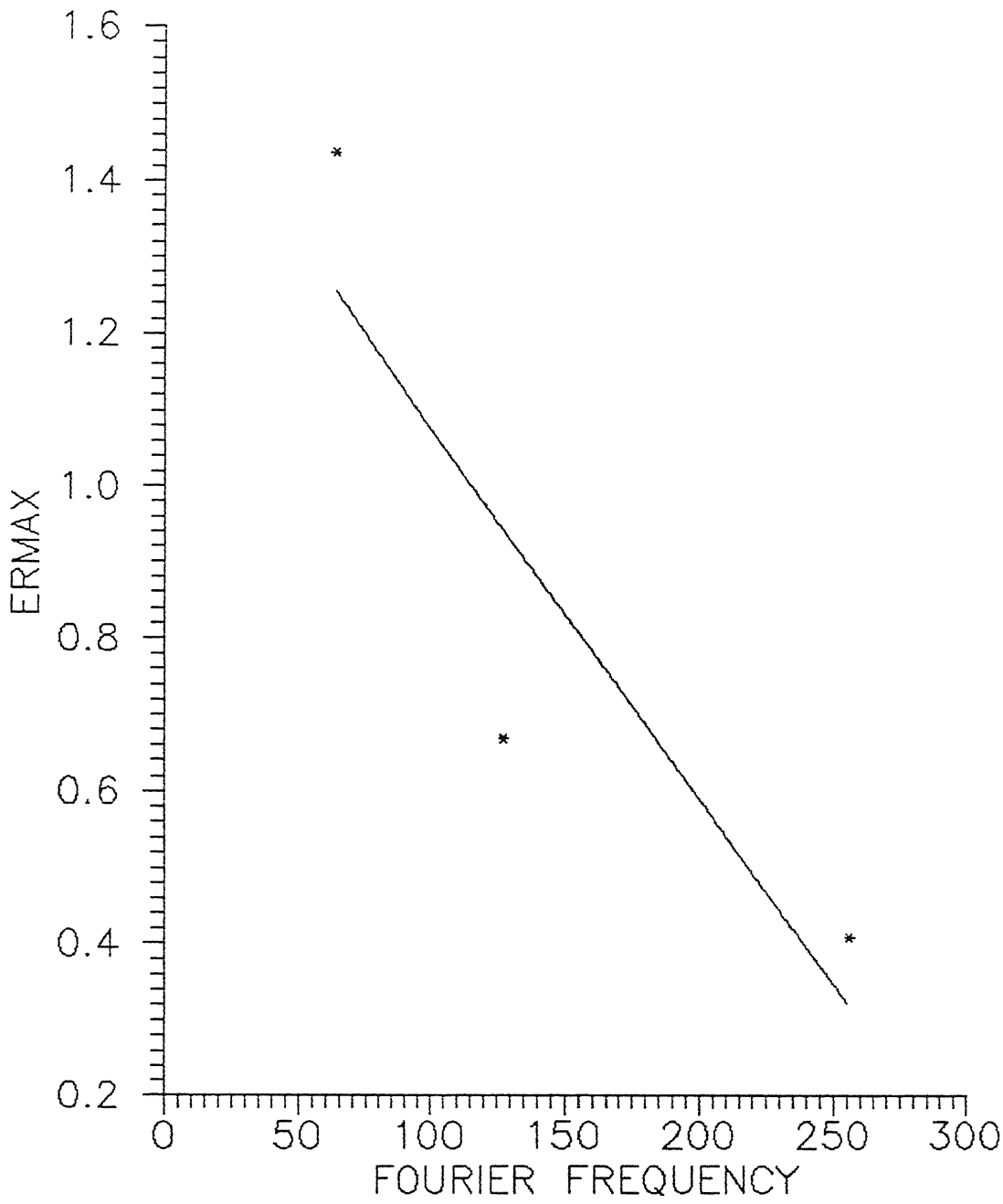

Figure 4.16: Maximum error variation at higher frequencies for THO

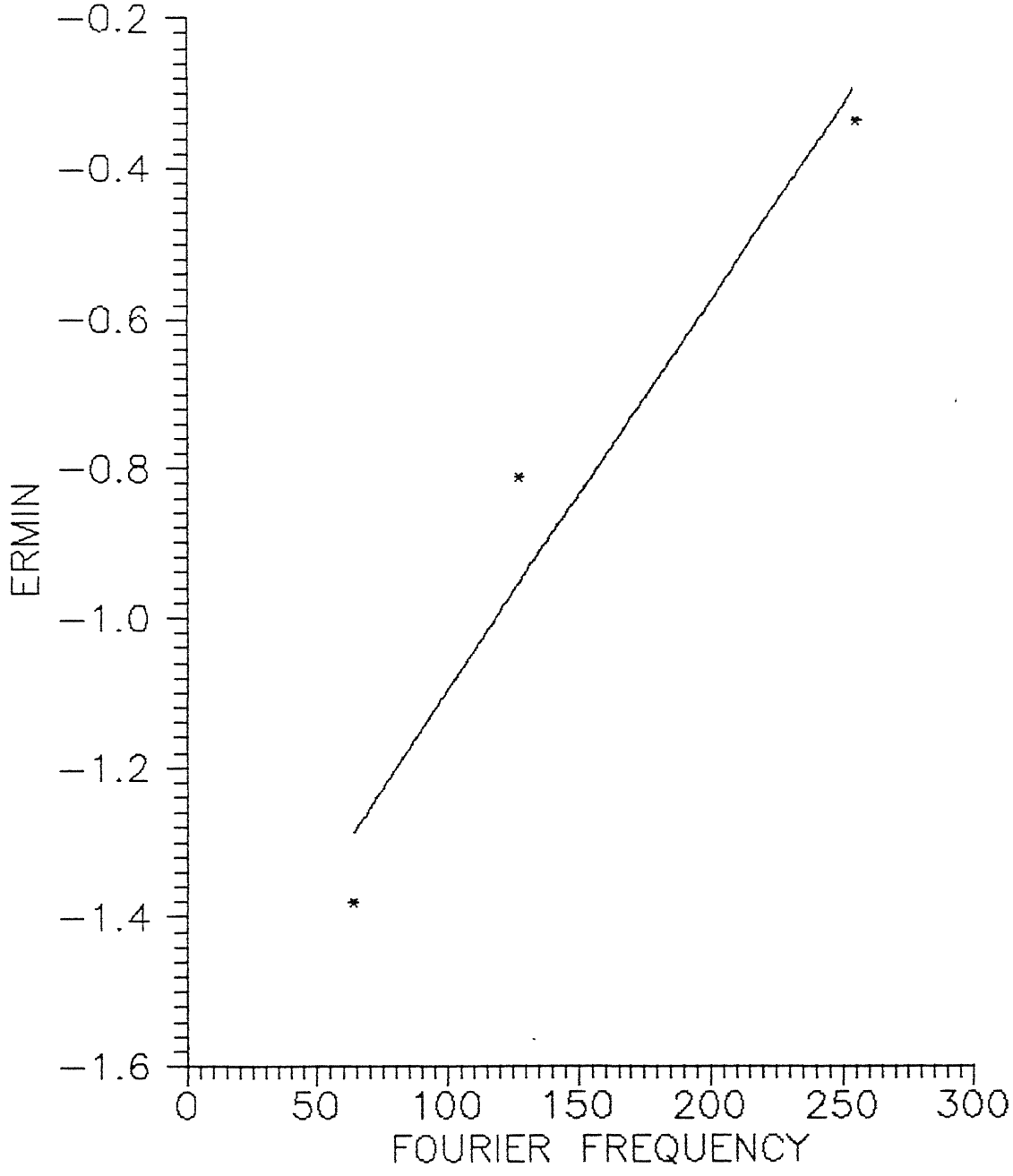

Figure 4.17: Minimum error variation at higher frequencies for THO

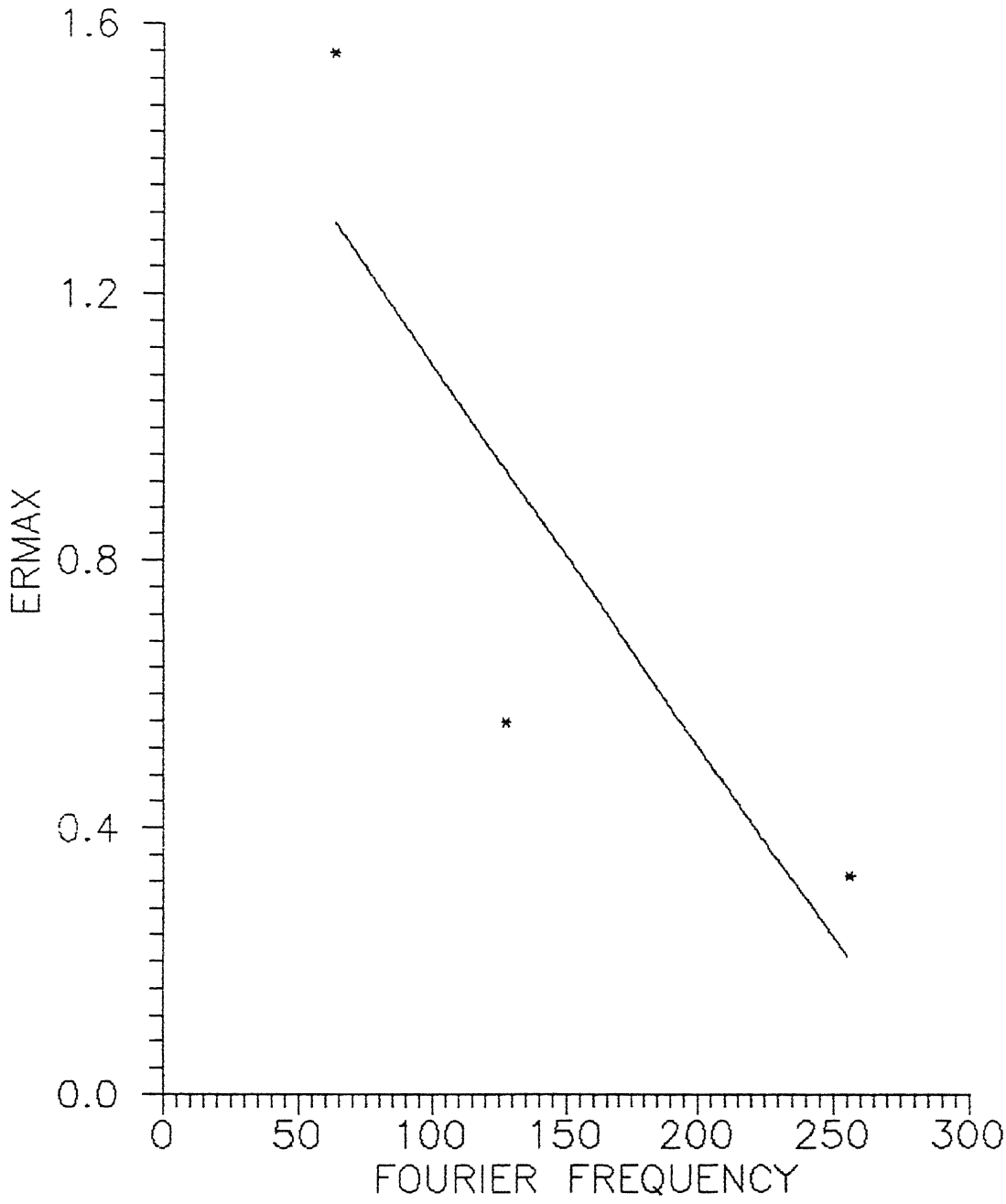

Figure 4.18: Maximum error variation at higher frequencies for TST

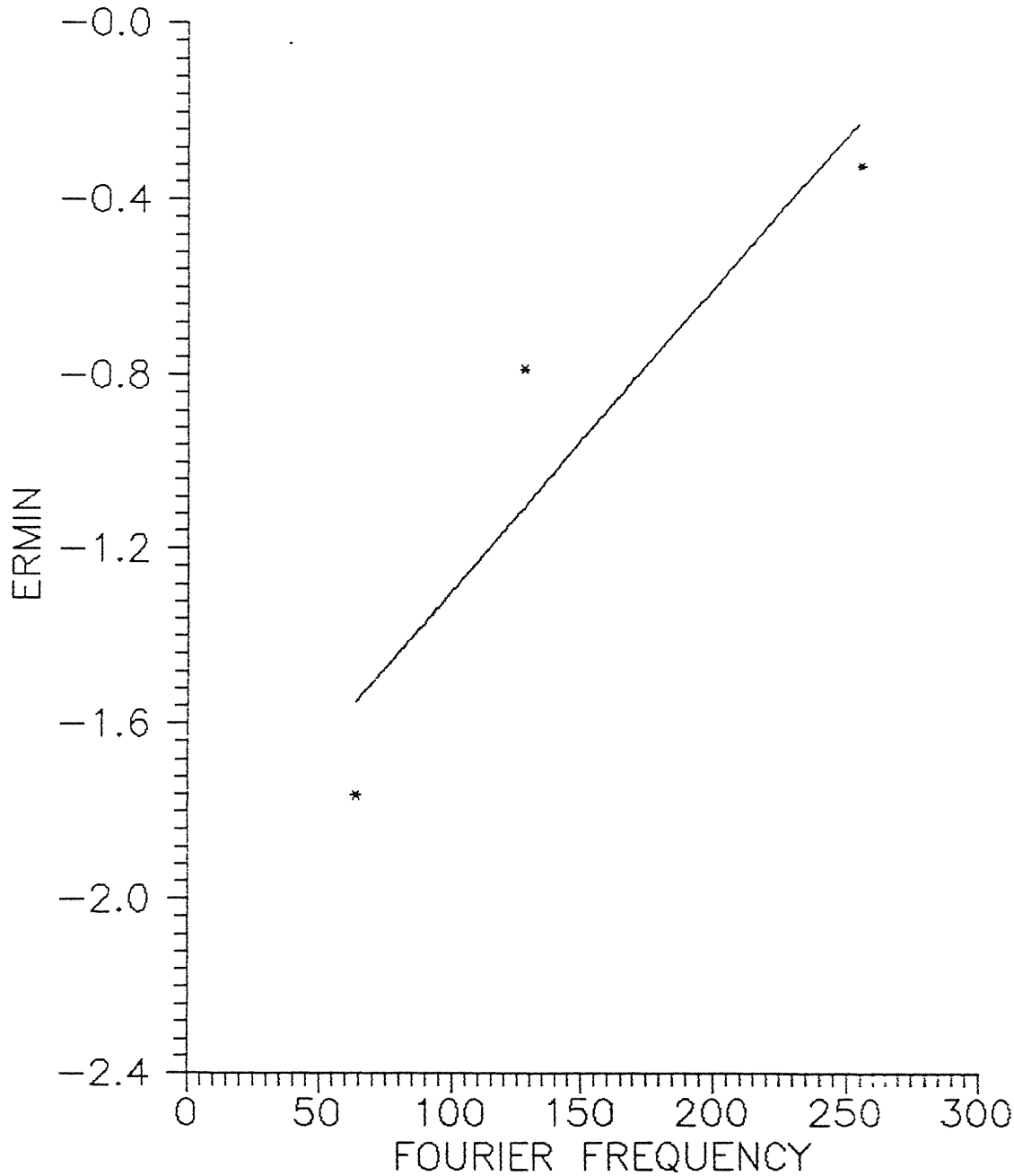

Figure 4.19: Minimum error variation at higher frequencies for TST

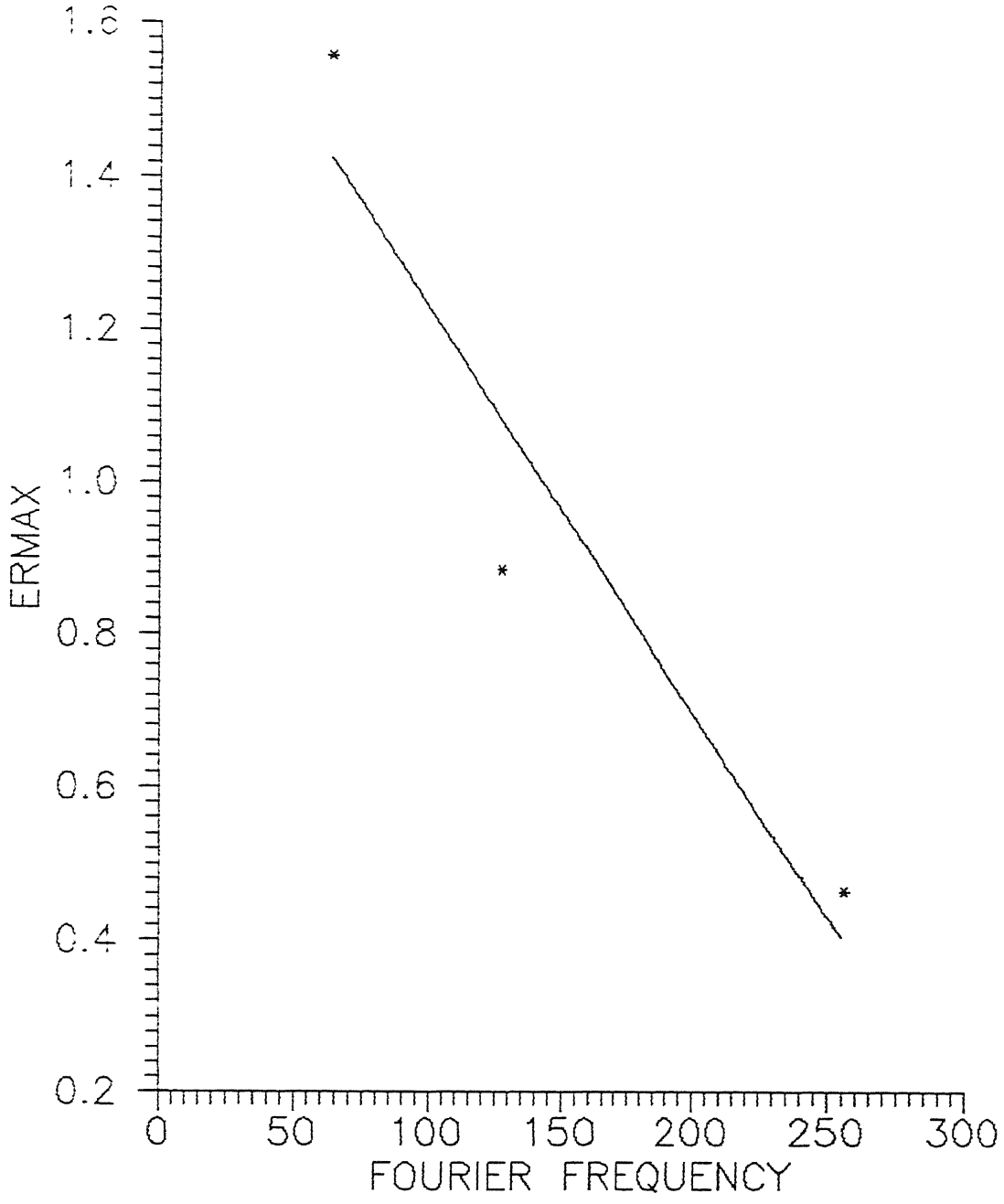

Figure 4.20: Maximum error variation at higher frequencies for BRN

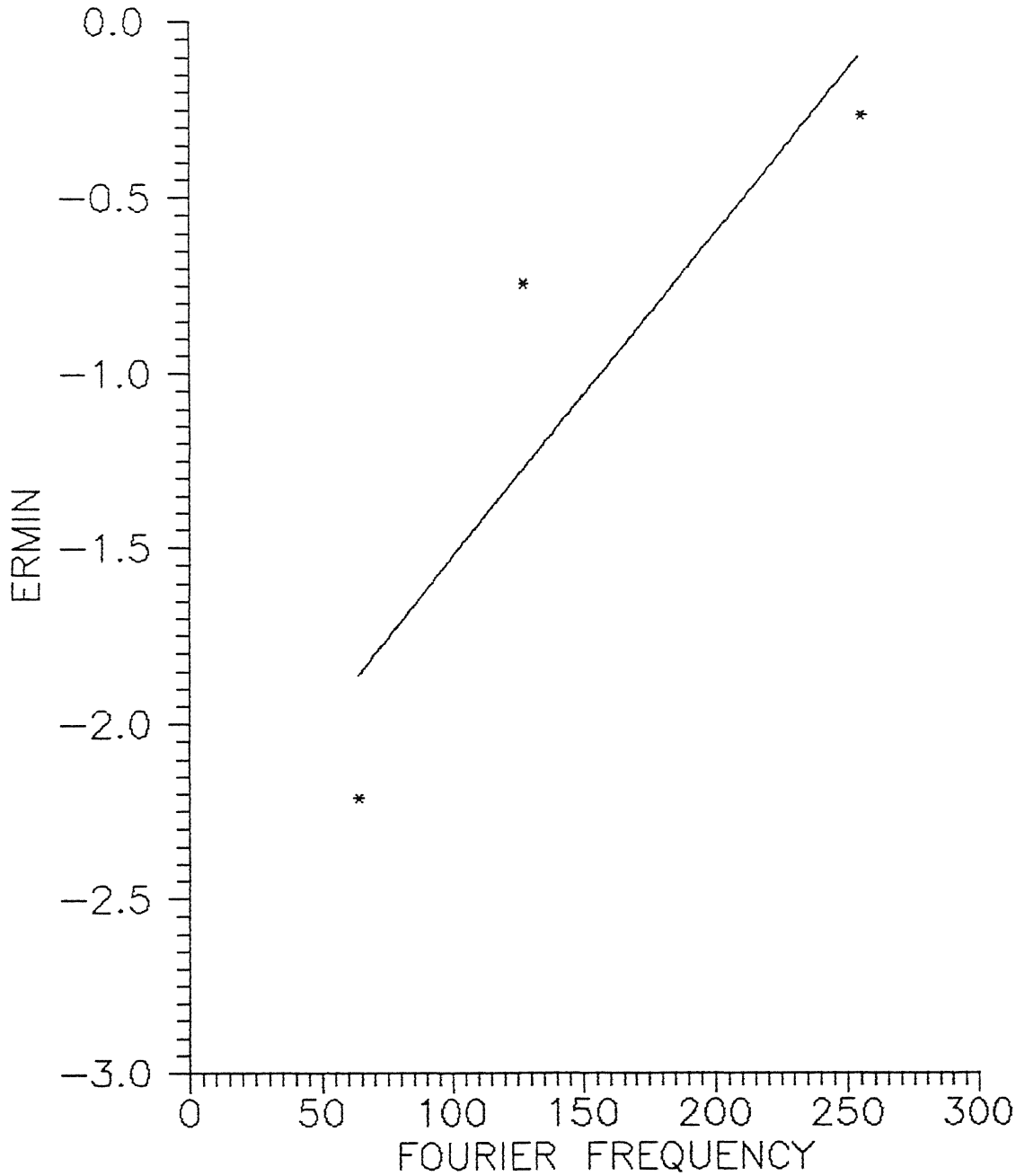

Figure 4.21: Minimum error variation at higher frequencies for BRN

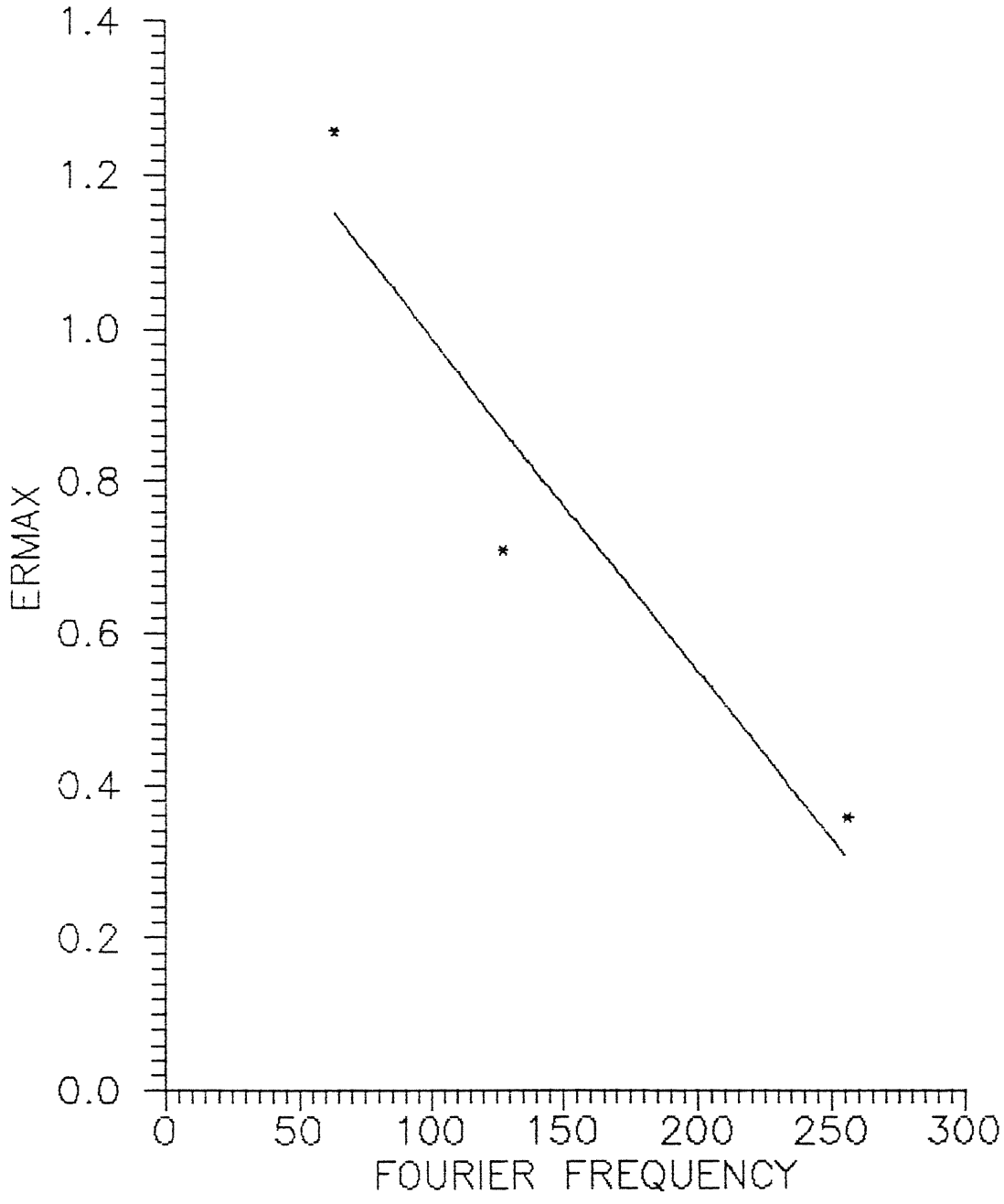

Figure 4.22: Maximum error variation at higher frequencies for PIC

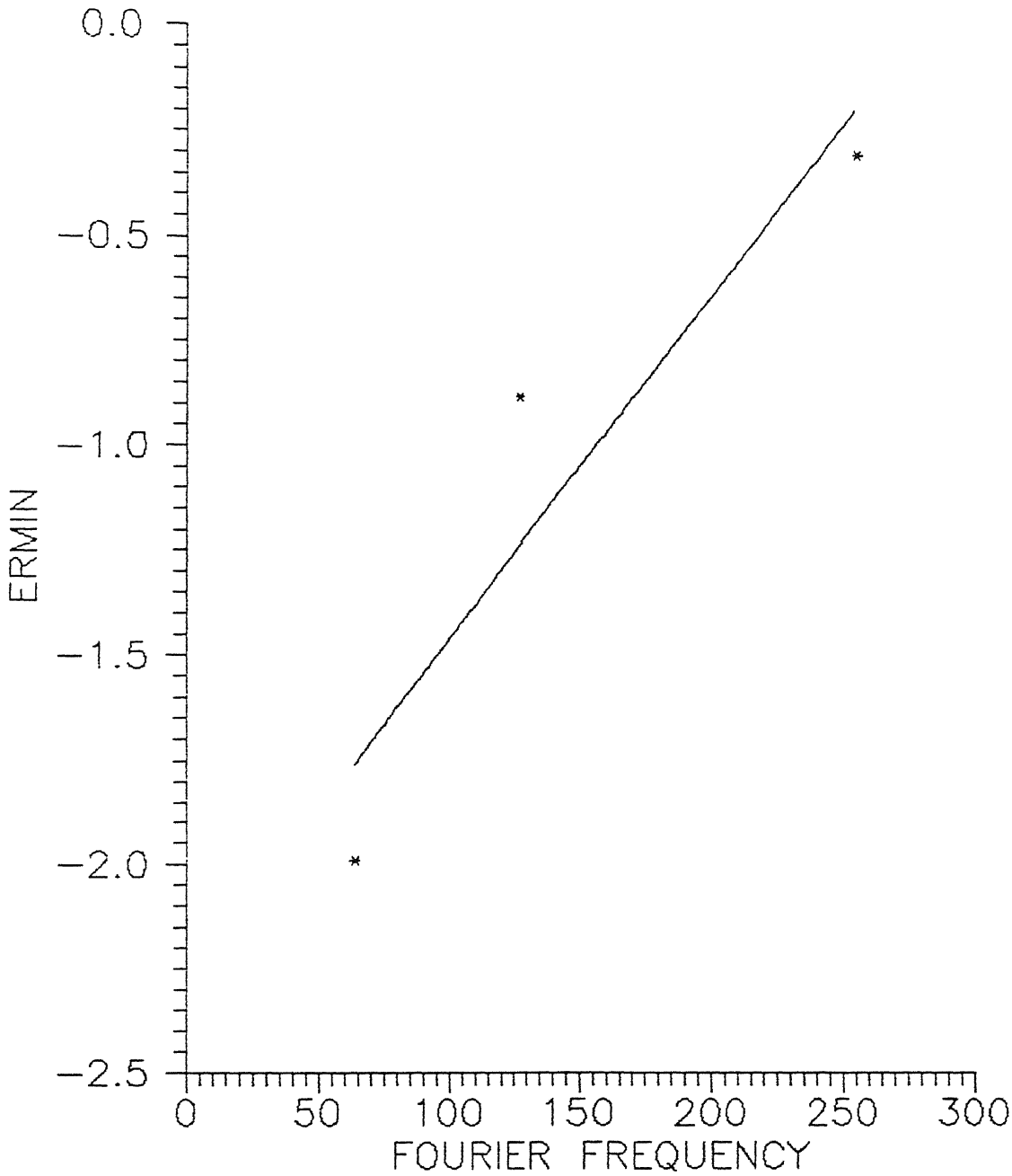

Figure 4.23: Minimum error variation at higher frequencies for PIC

Chapter 5

Conclusions and Recommendations

The application of Computer Tomography in a variety of fields ranging from medical imaging to astronomy demands a careful analysis of various errors involved in reconstruction of the projection data as different applications demand different precision and accuracy. The various errors involved in the reconstruction of objects are : error due to *beam hardening, photon statistics, focal spot of the source* and *finite detector width* (they are also referred as Partial Volume effect), *organ motion effect* etc. And of course, the *discretization* and *inherent error.*

Beauty of using computer simulation lies in the fact that effect of these errors can be studied separately and they can be coupled to make a judicious choice of various parameters affecting the error of reconstruction. The importance of this investigation is obvious because this not only helps to decide number of rays to be used for particular application, but also depicts the limitations of the algorithm used. Hence this investigation could be of immense practical application for deciding various parameters in design and development of CT scanners for various purposes

It is clear that the error value is reasonably small with number of views 1600 and

number of rays 256.

Following recommendations can be made regarding further investigations:

1. Discretization and inherent errors are coupled here and hence a scope to devise a methodology to separate the two and analyse their effect separately is there.

2. The studies can be done by coupling the internal errors(such as discretization and inherent errors) and external errors (such as photon statistics and Beam hardening etc.) for particular applications. This can be of immense practical application.

3. Effect of various filters for optimal number of rays and views on the error can be studied.

Appendix A

Reconstructed Images

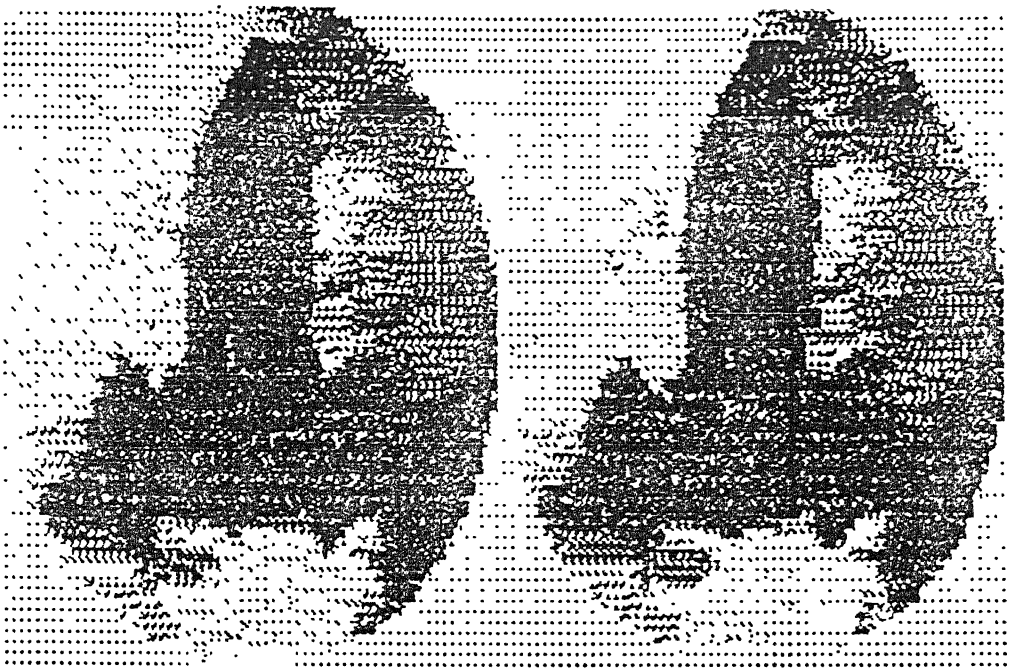

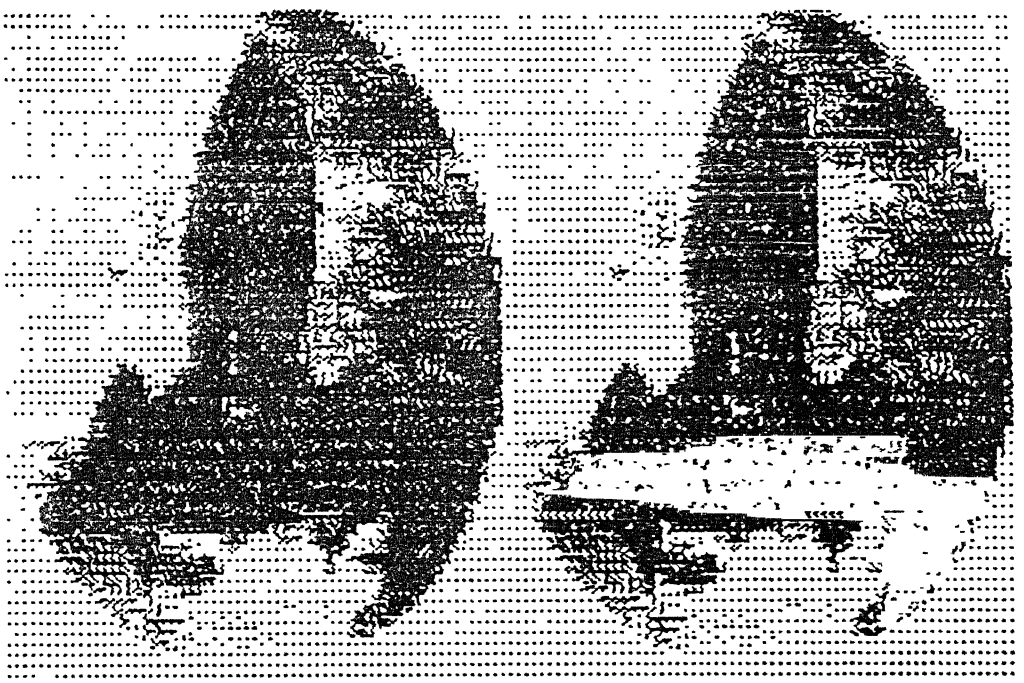

Figure A.1: Reconstructed Images

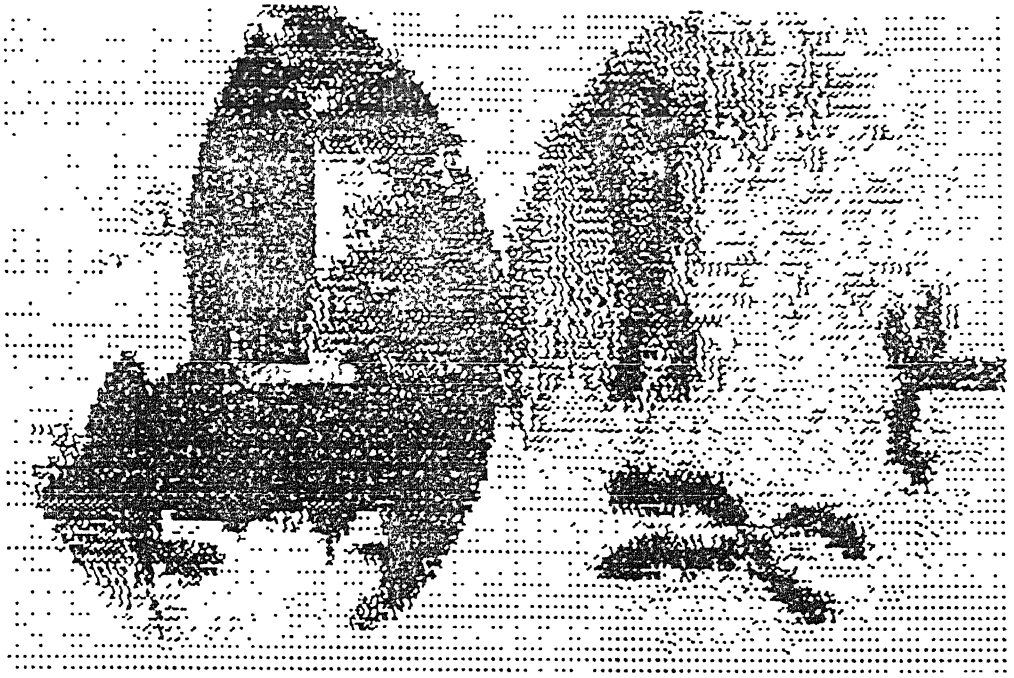

A=256

JET

A=16

CRO

A=32

CRO

A=64

CRO

Figure A.2: Reconstructed Images

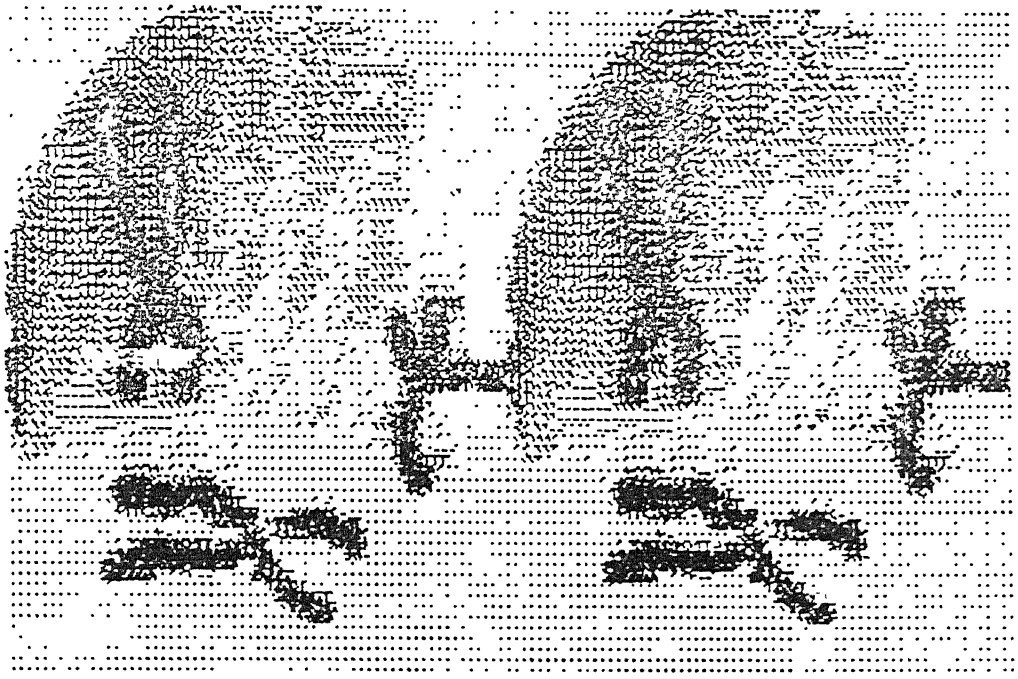

A=128

CR0

A=256

CR0

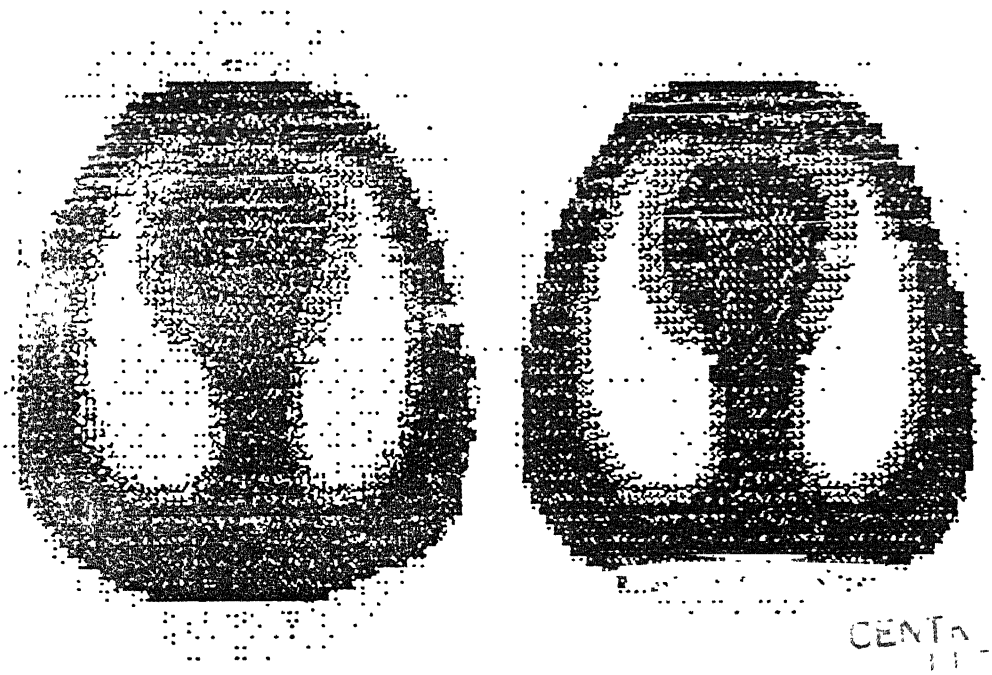

A=16

TH0

A=32

TH0

CENTRAL LIBRARY
Acc. No. A113495

Figure A.3: R...

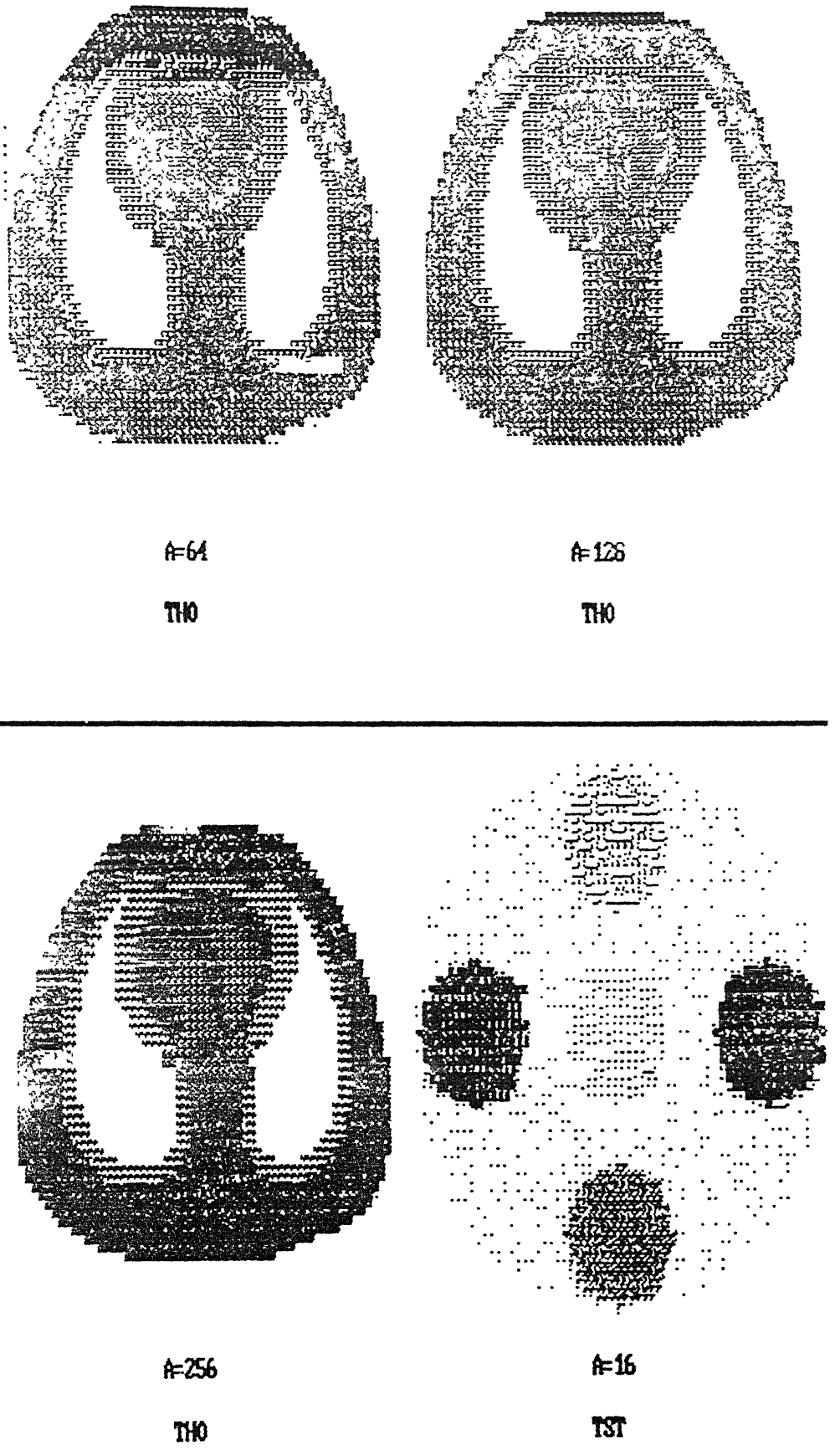

Figure A.4: Reconstructed Images

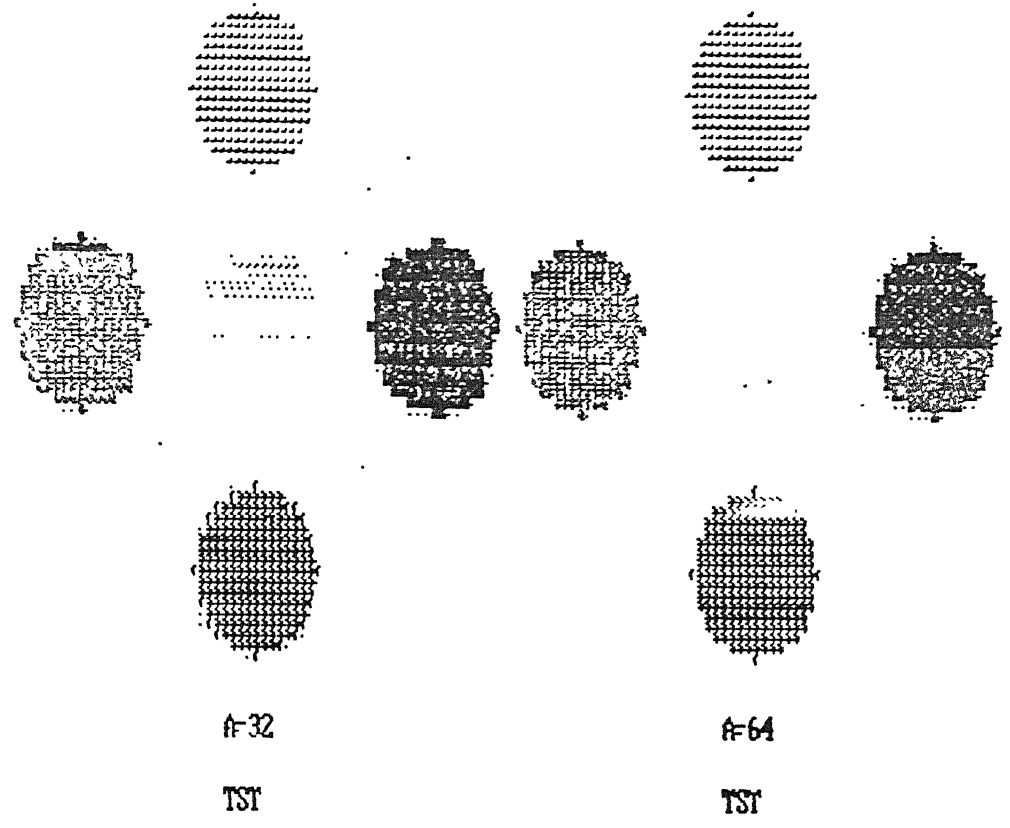

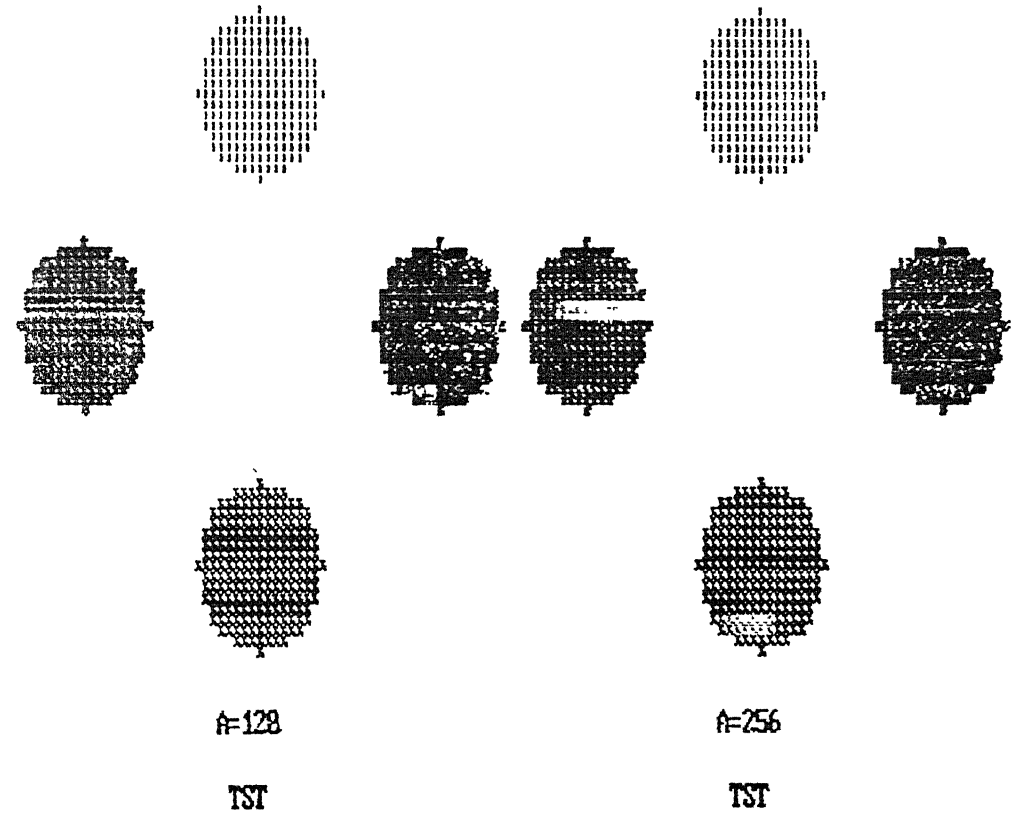

Figure A.5: Reconstructed Images

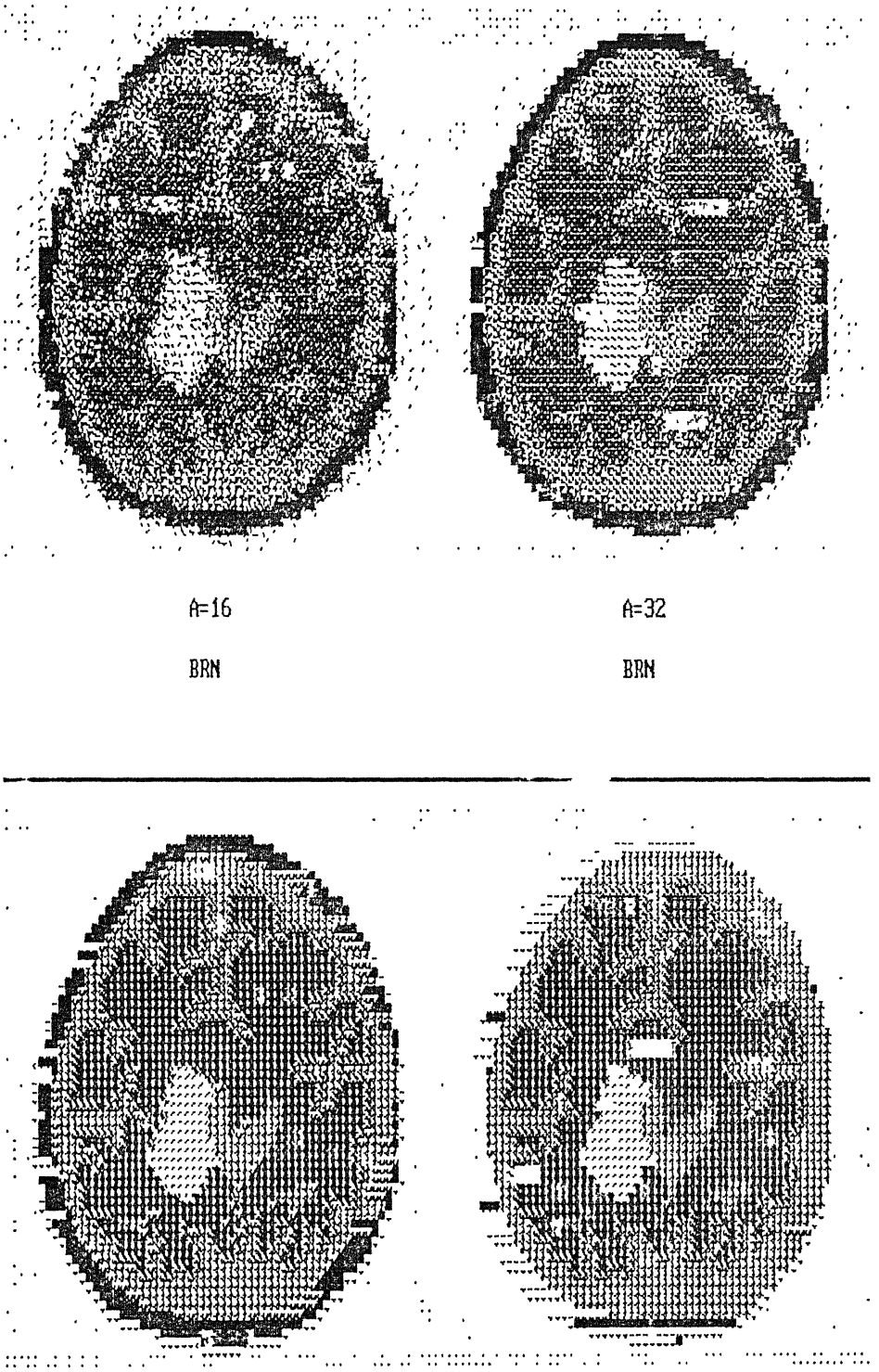

Figure A.6: Reconstructed Images

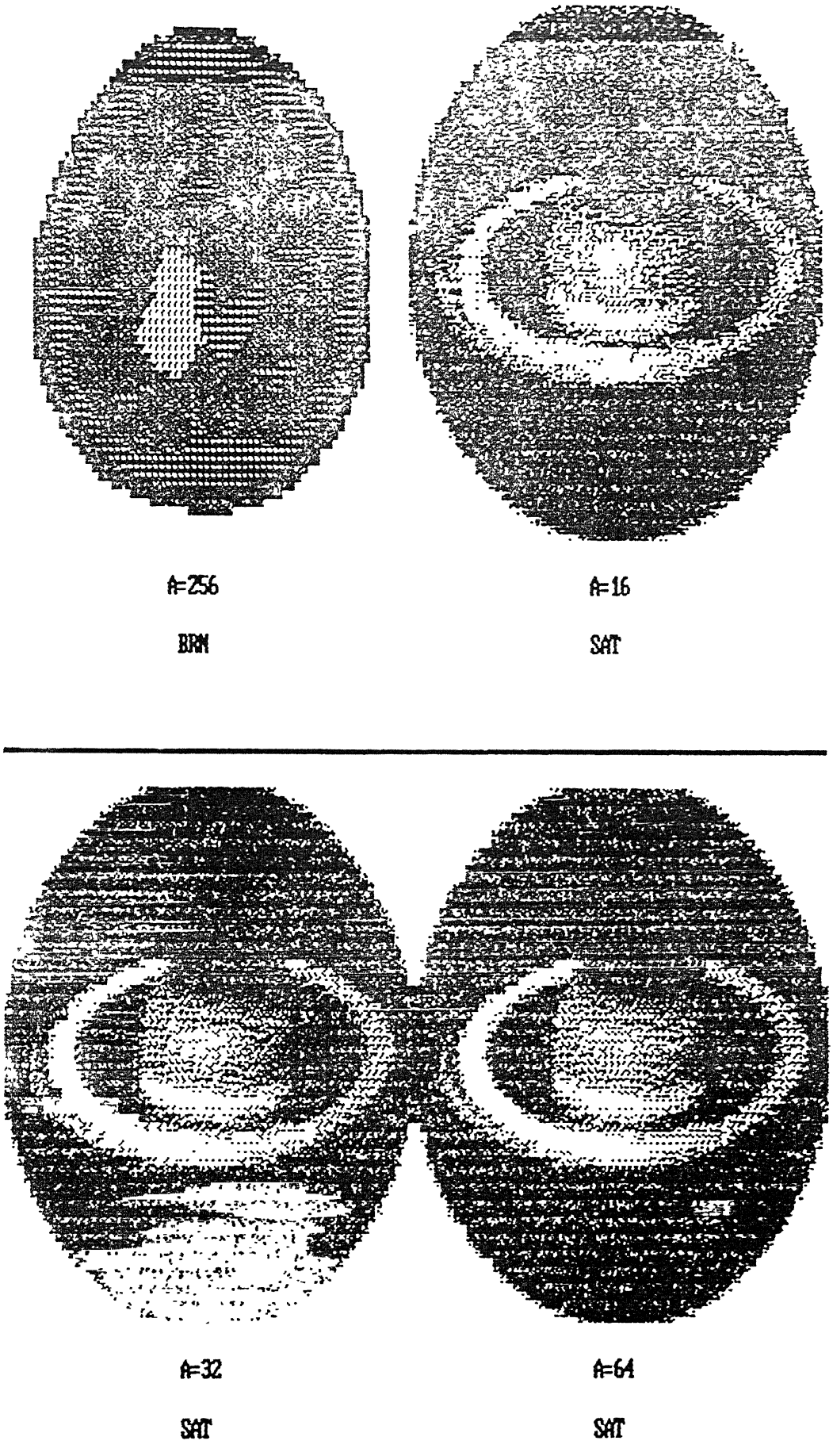

Figure A.7: Reconstructed Images

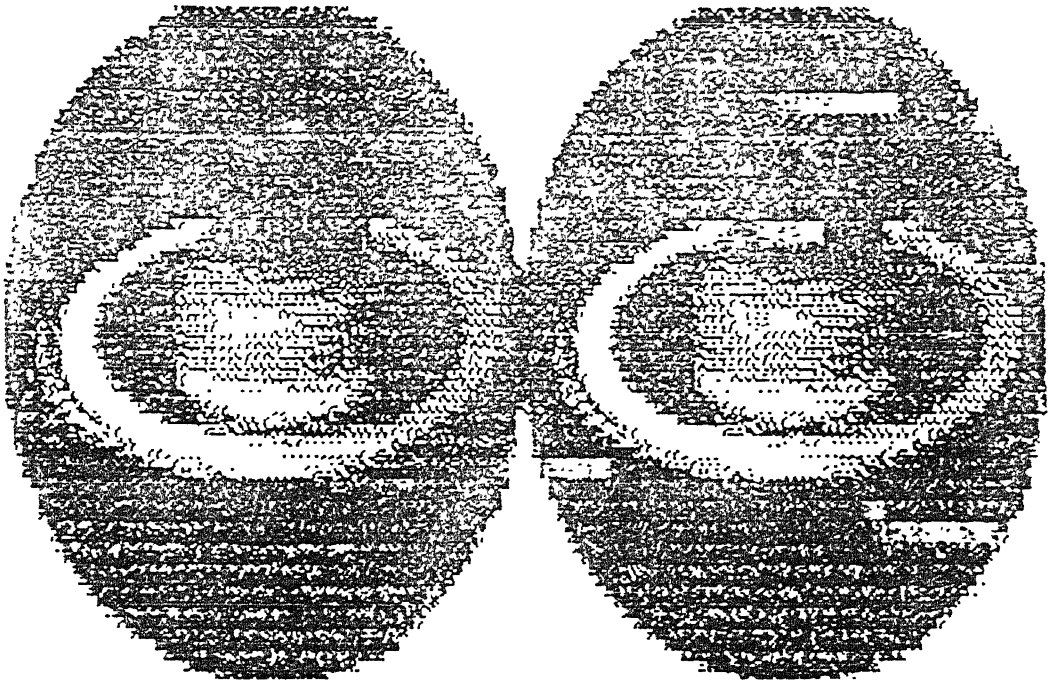

A=128

SAT

A=256

SAT

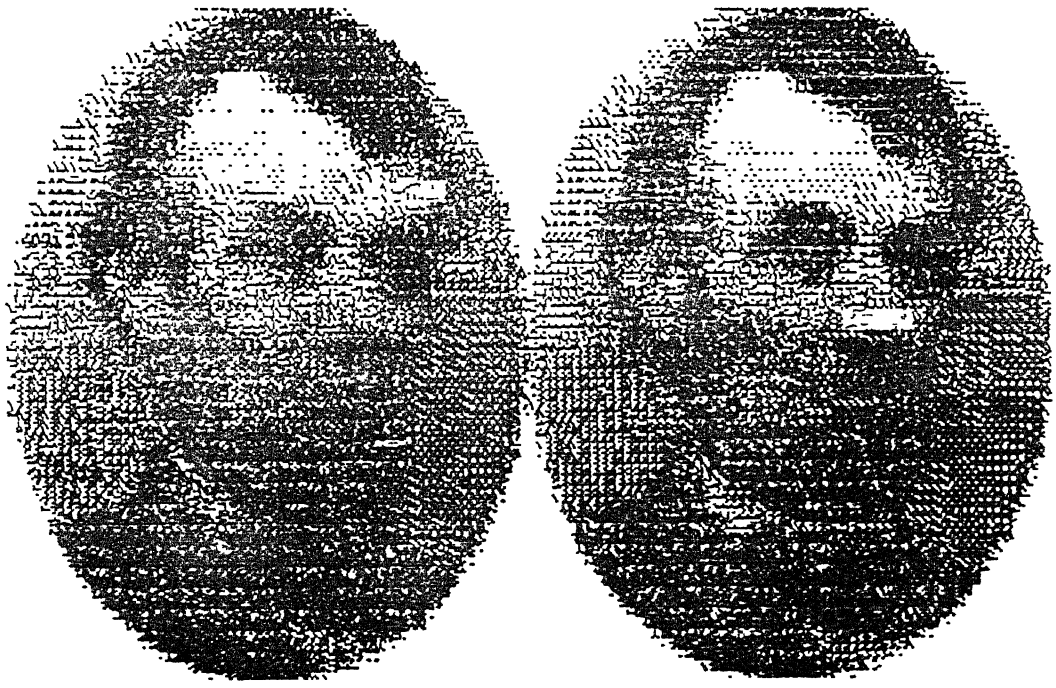

A=16

LIN

A=32

LIN

Figure A.8: Reconstructed Images

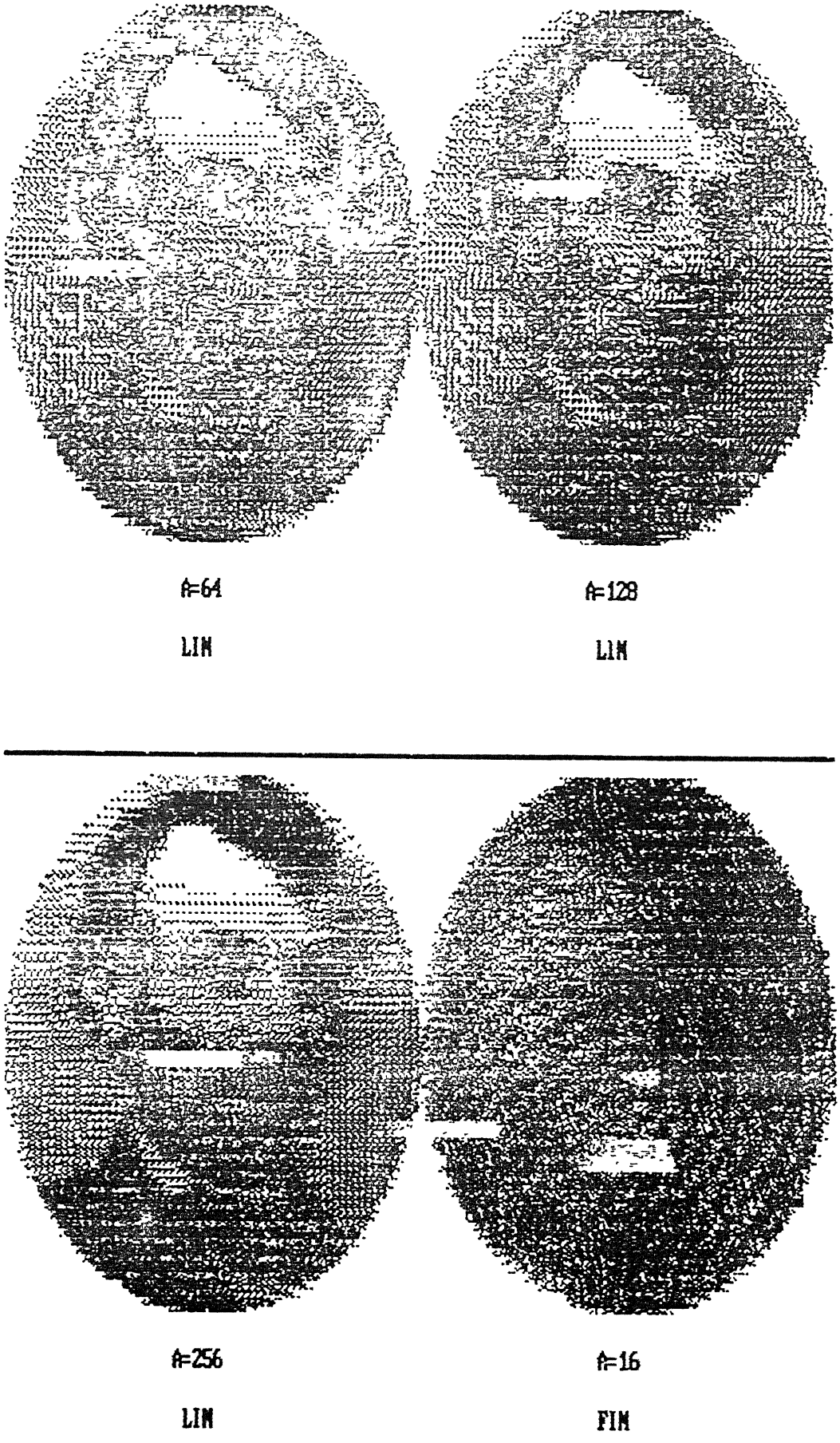

Figure A.9: Reconstructed Images

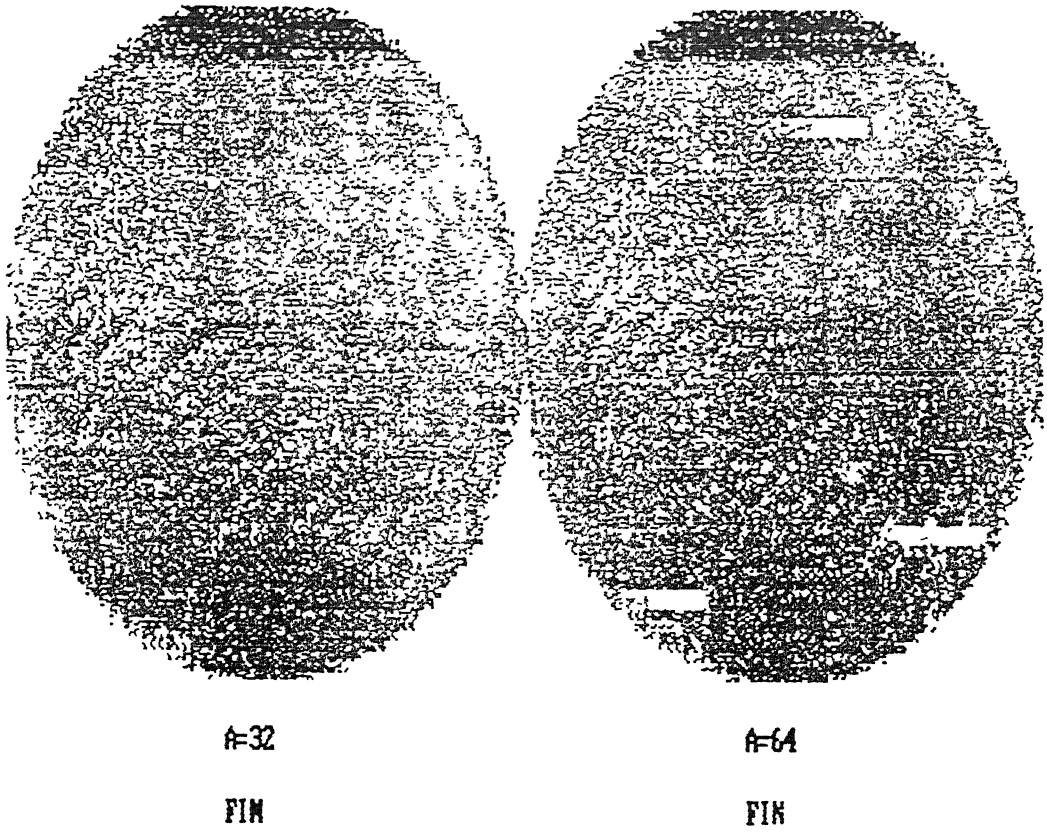

Figure A.10: Reconstructed Images

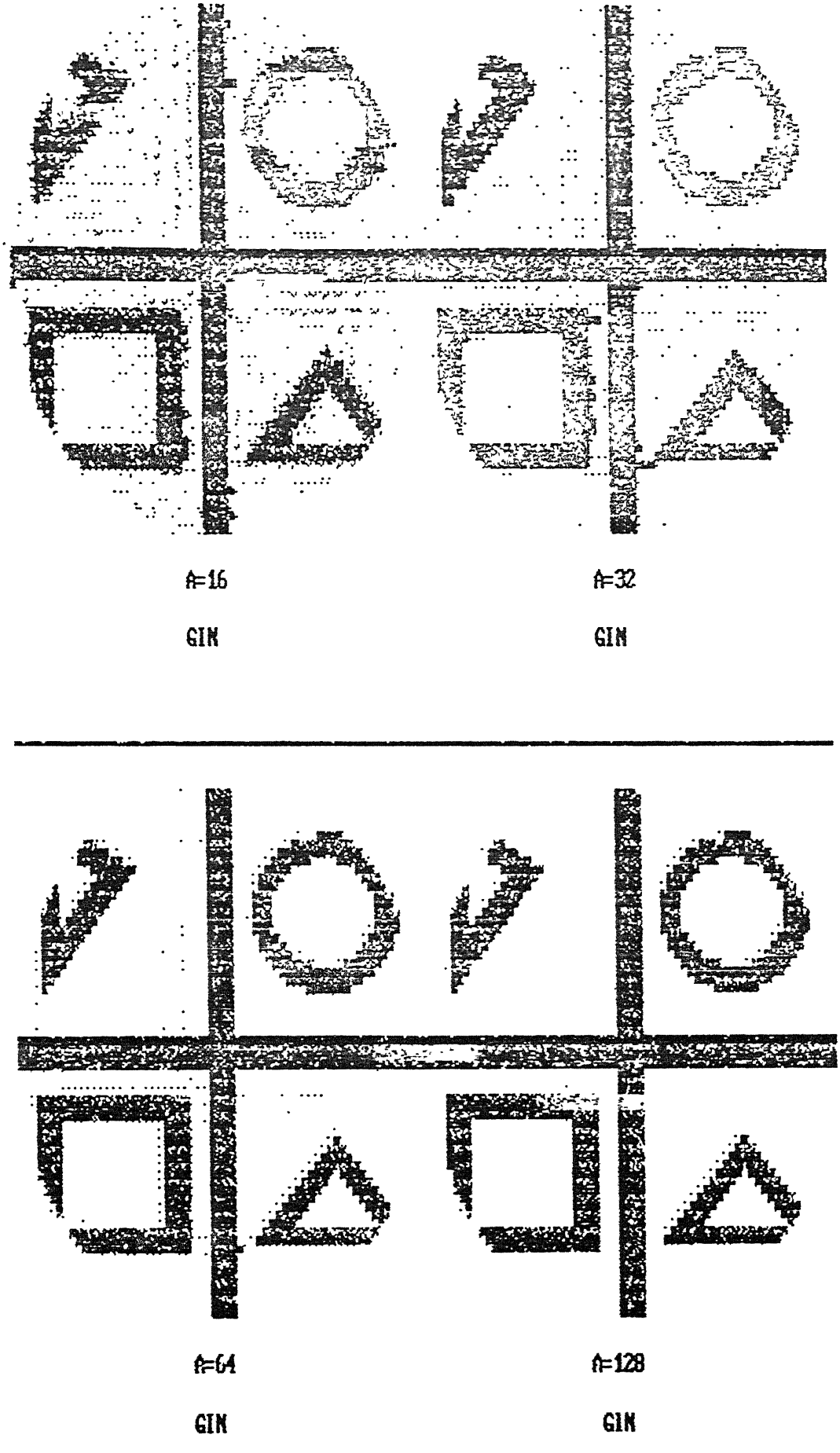

Figure A.11: Reconstructed Images

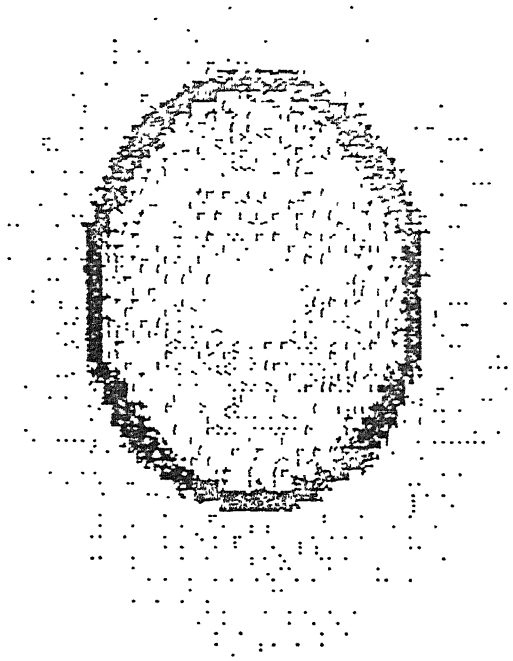

A=16

PIC

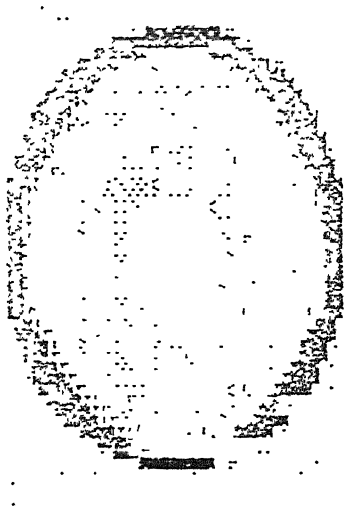

A=32

PIC

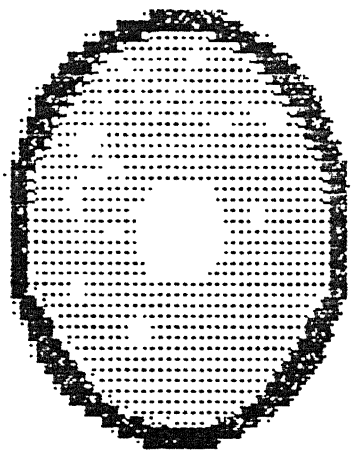

A=64

PIC

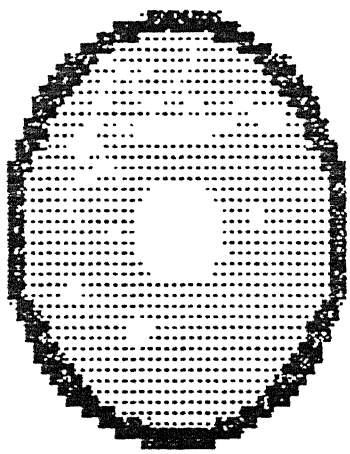

A=128

PIC

Figure A.12: Reconstructed Images

Appendix B

Error Variation with Frequency

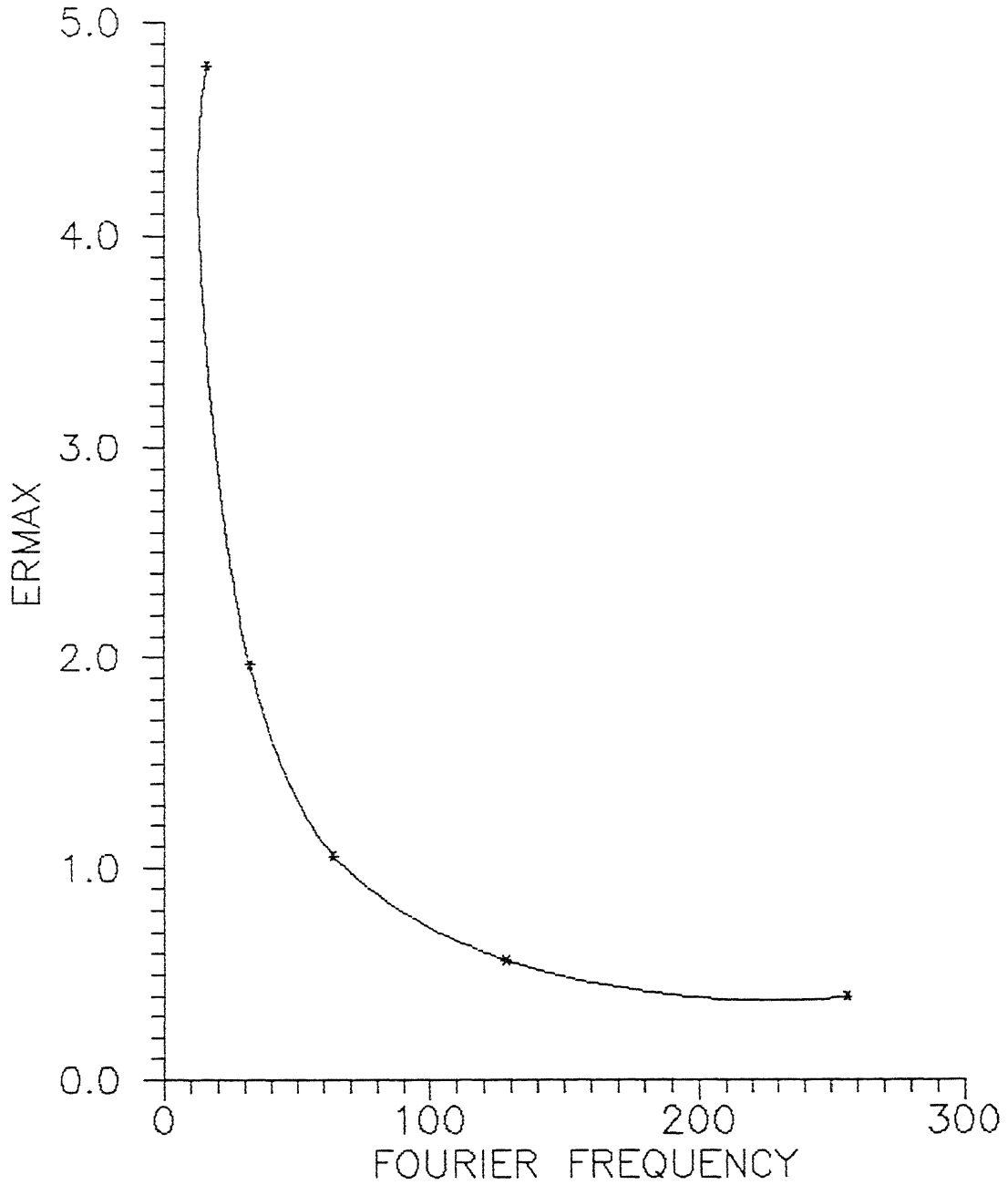

Figure B.1: Error Variation With Fourier Frequency for SAT

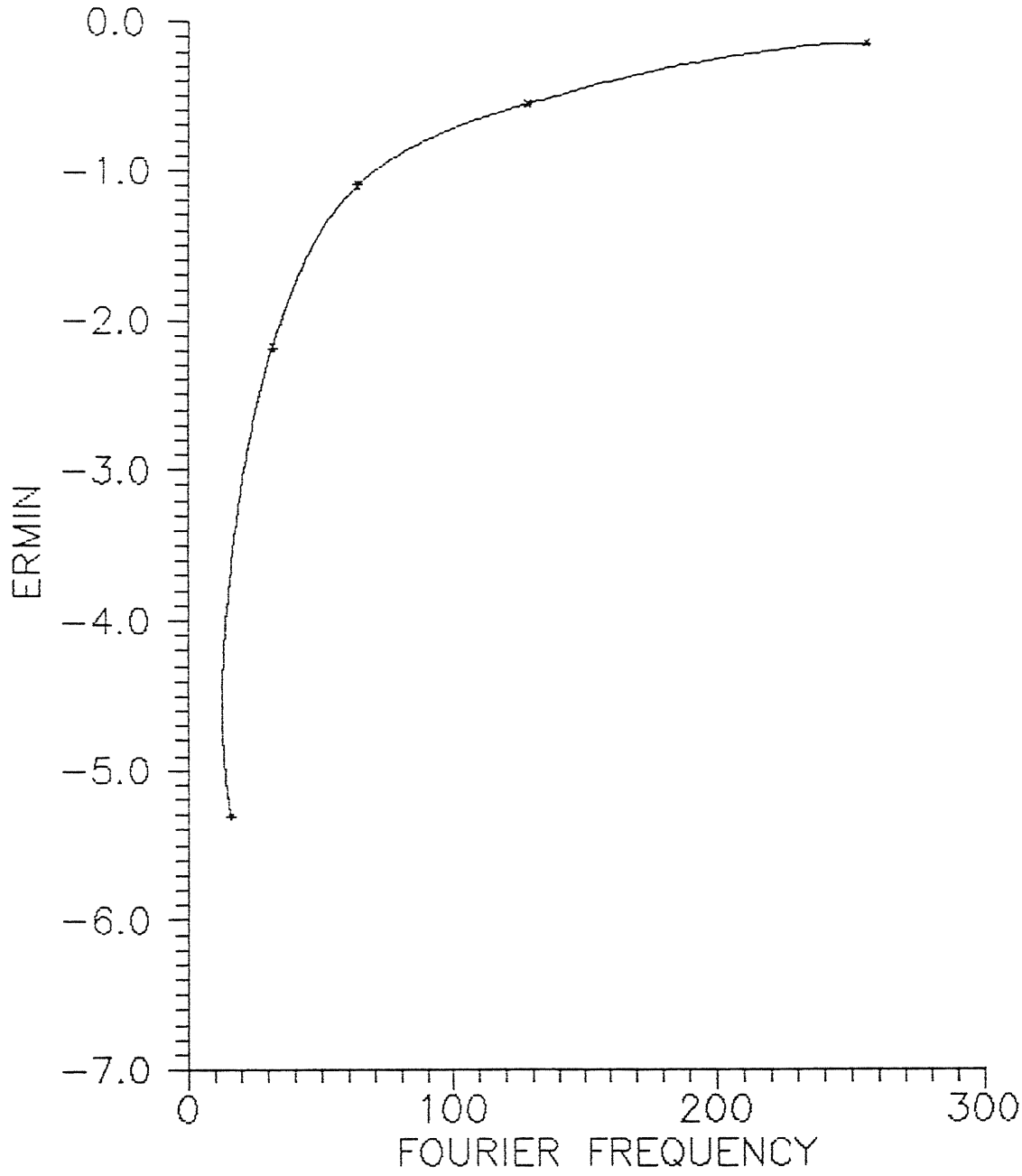

Figure B.2: Error Variation With Fourier Frequency for SAT

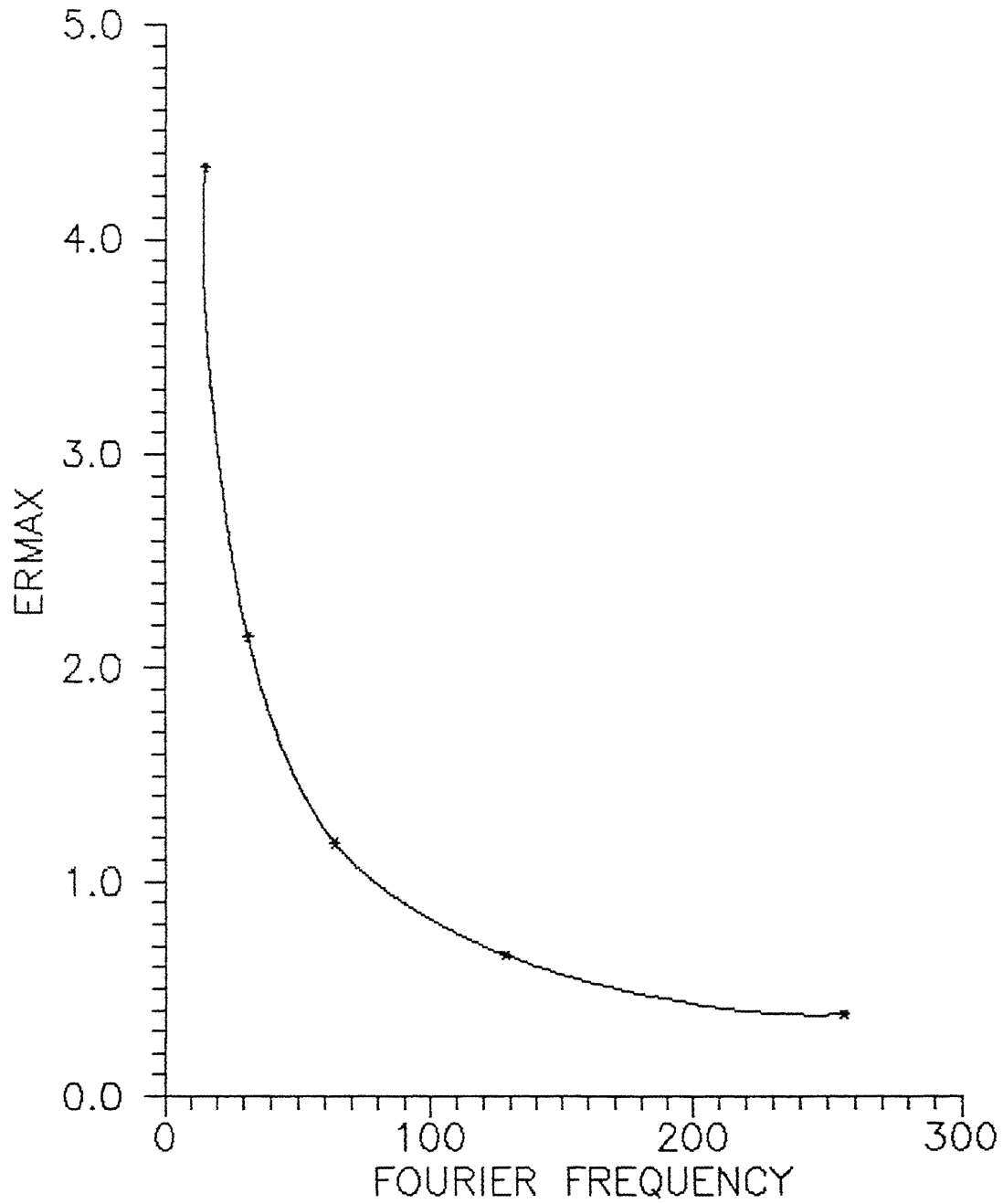

Figure B.3: Error Variation With Fourier Frequency for LIN

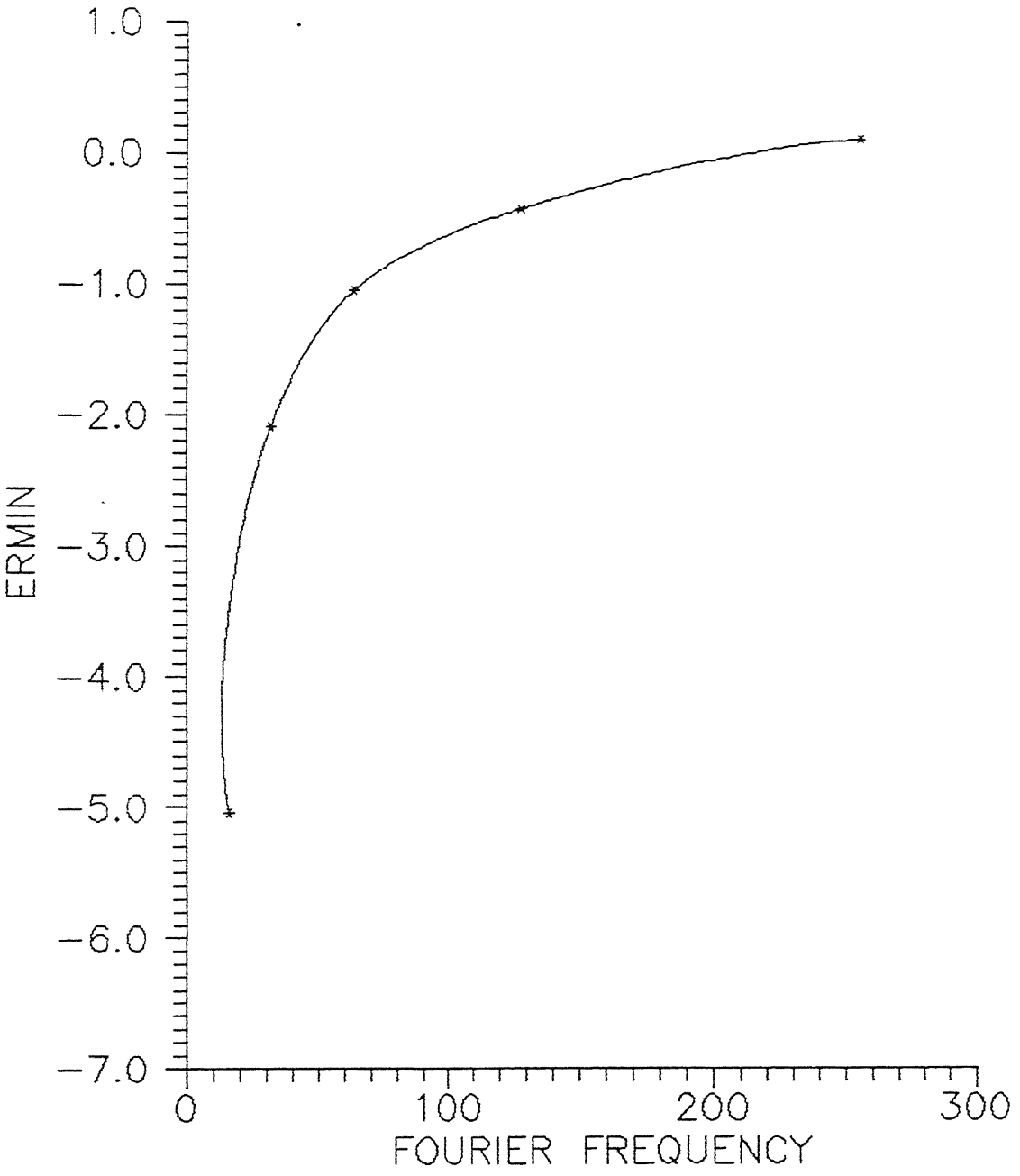

Figure B.4: Error Variation With Fourier Frequency for LIN

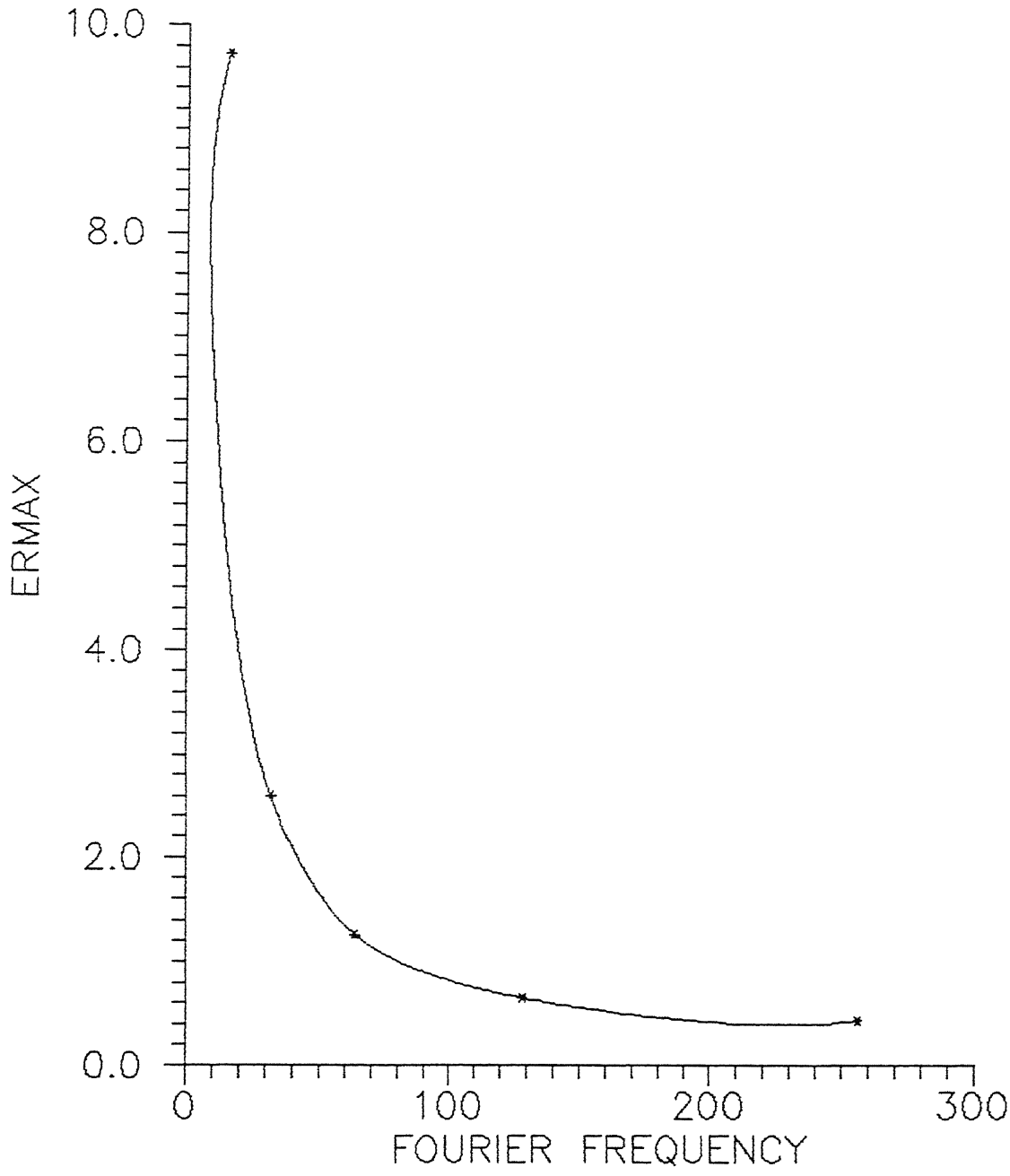

Figure B.5: Error Variation With Fourier Frequency for FIN

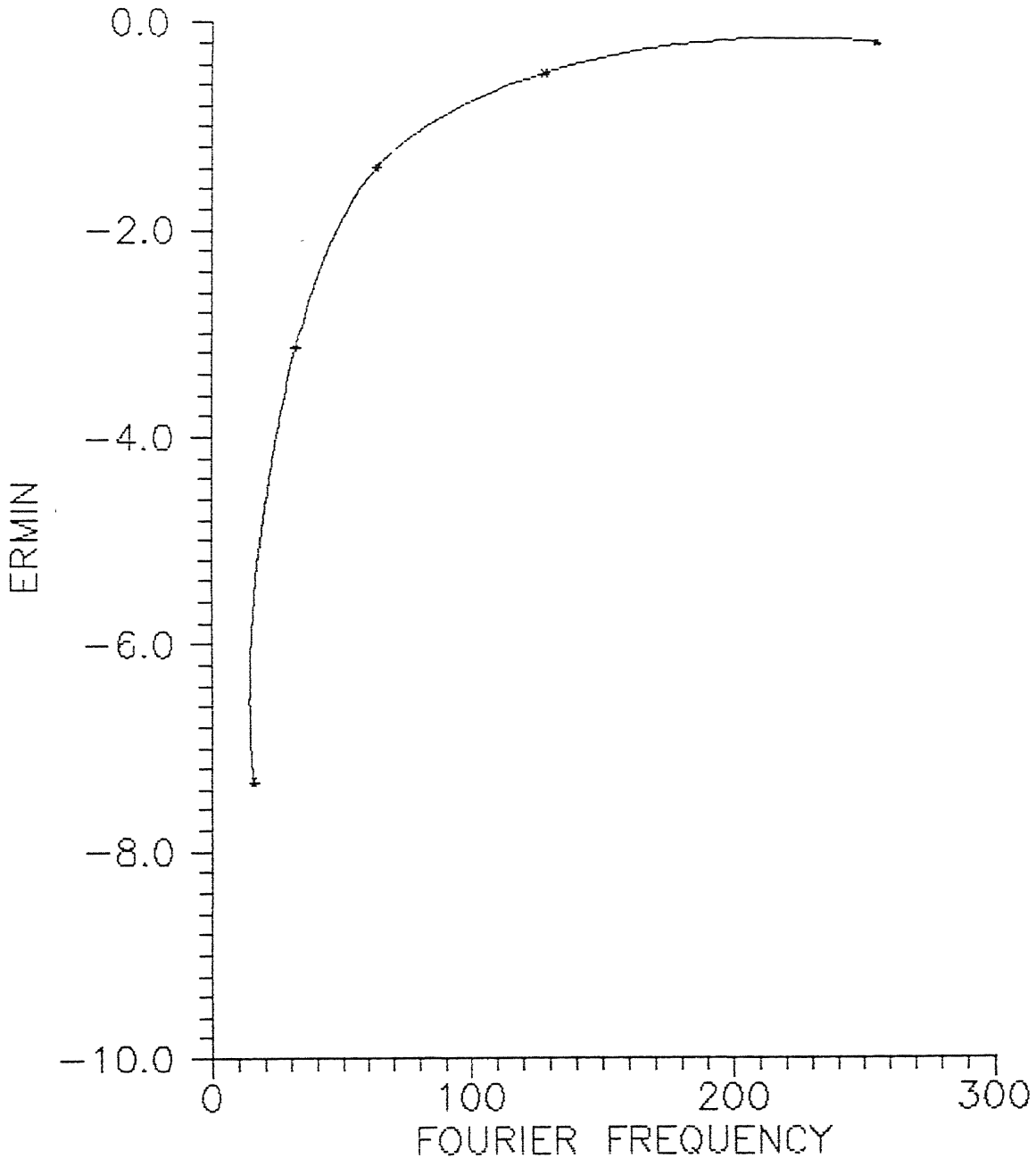

Figure B.6: Error Variation With Fourier Frequency for FIN

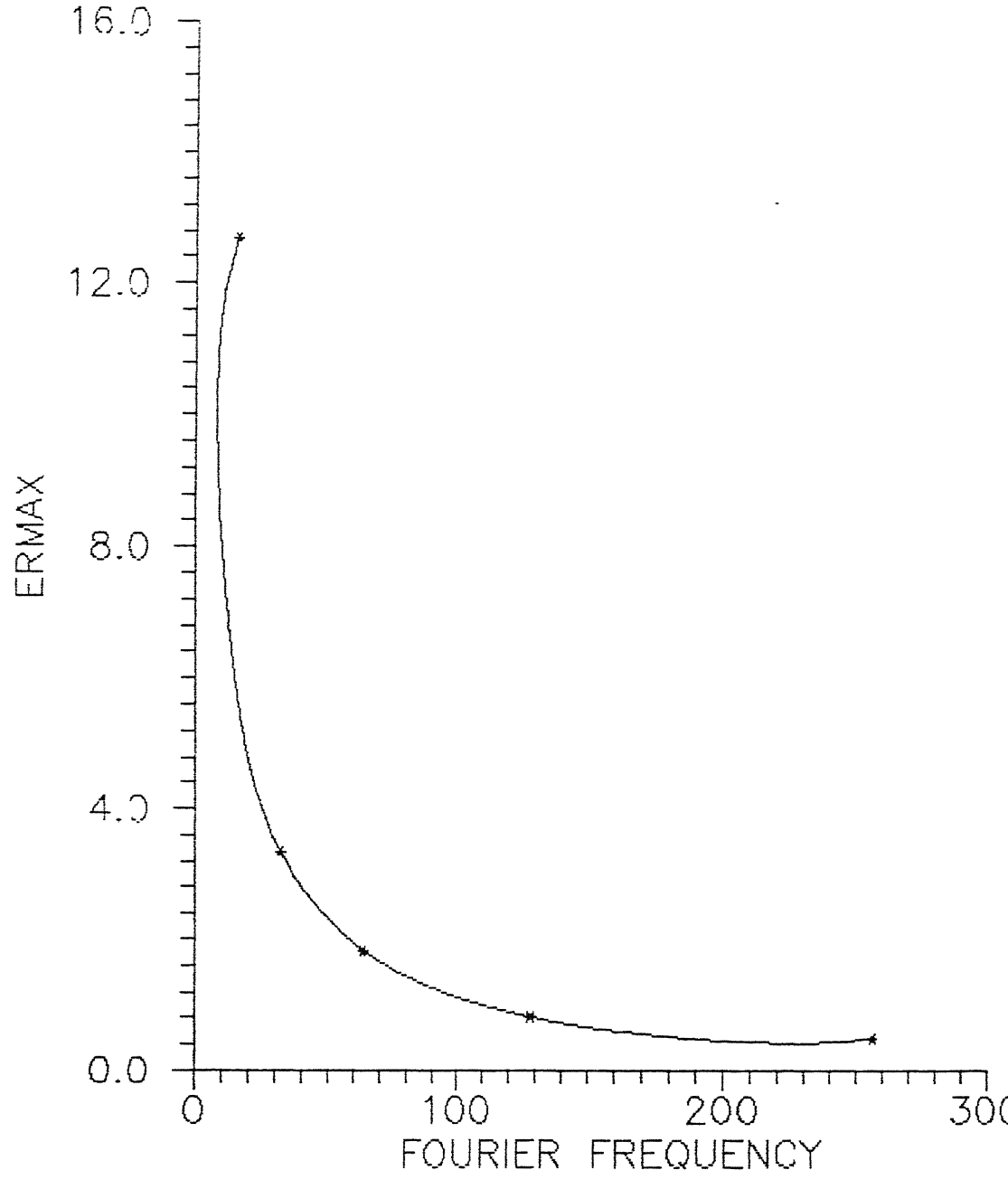

Figure B.7: Error Variation With Fourier Frequency for GIN

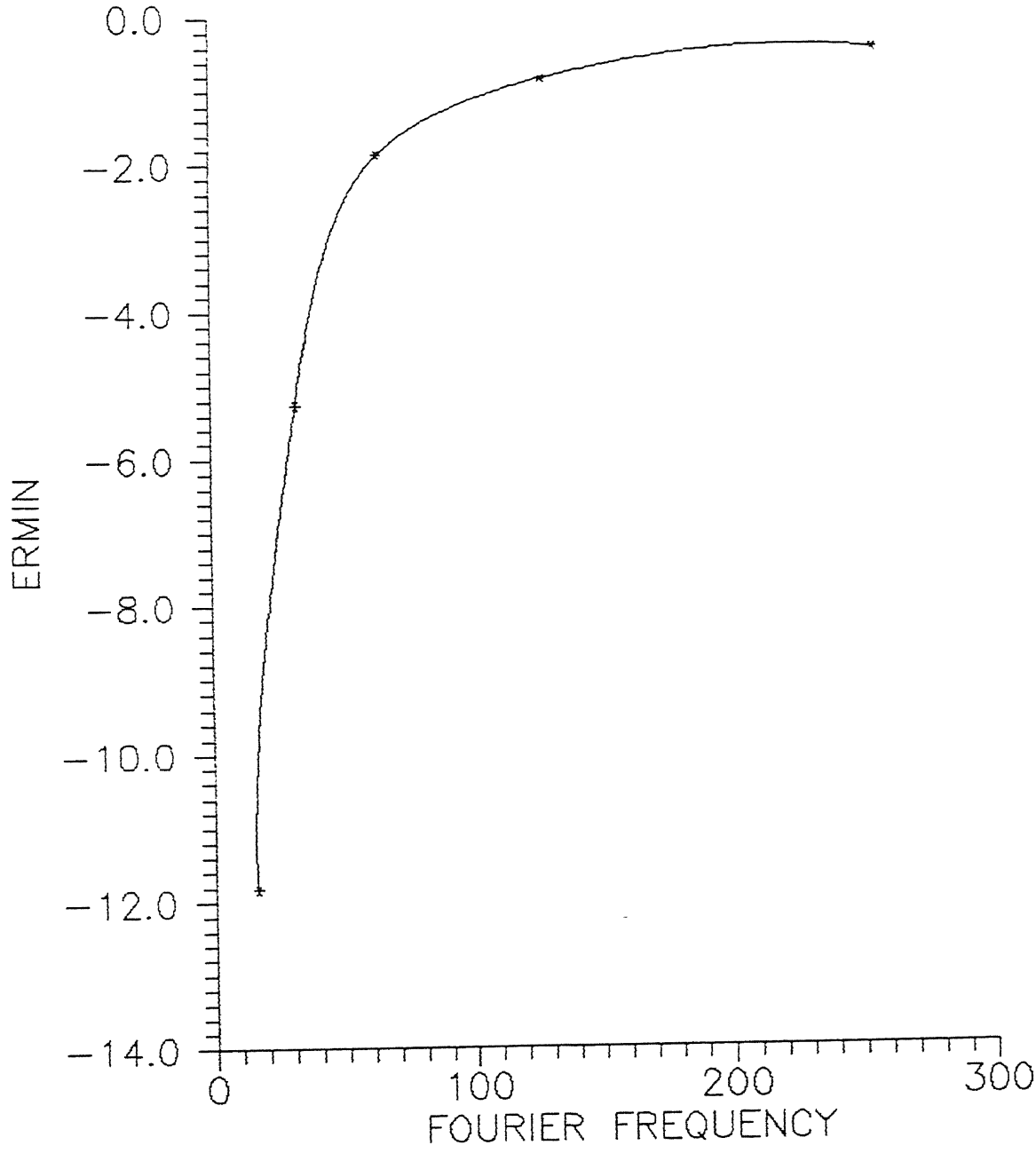

Figure B.8: Error Variation With Fourier Frequency for GIN

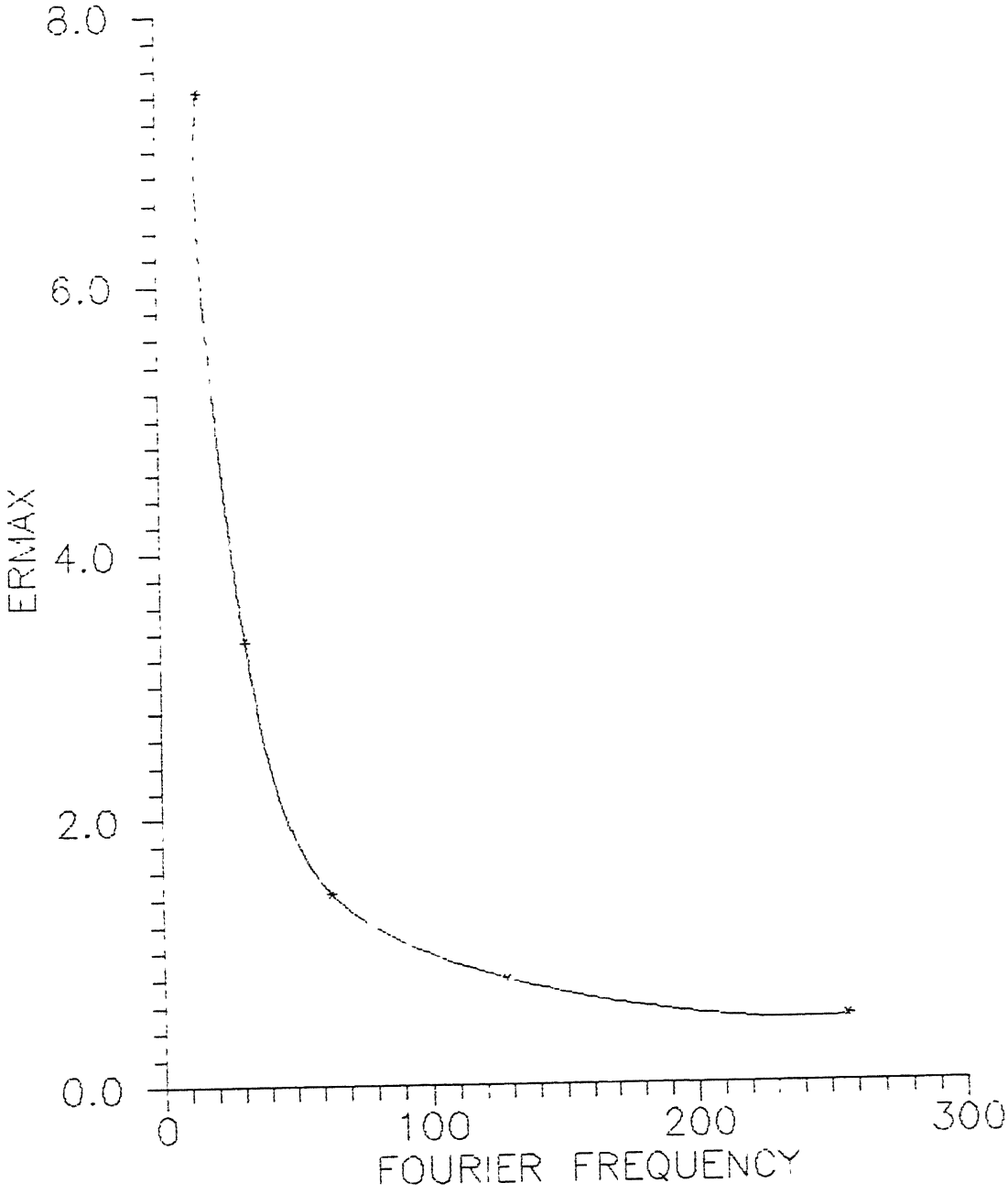

Figure B.9: Error Variation With Fourier Frequency for JET

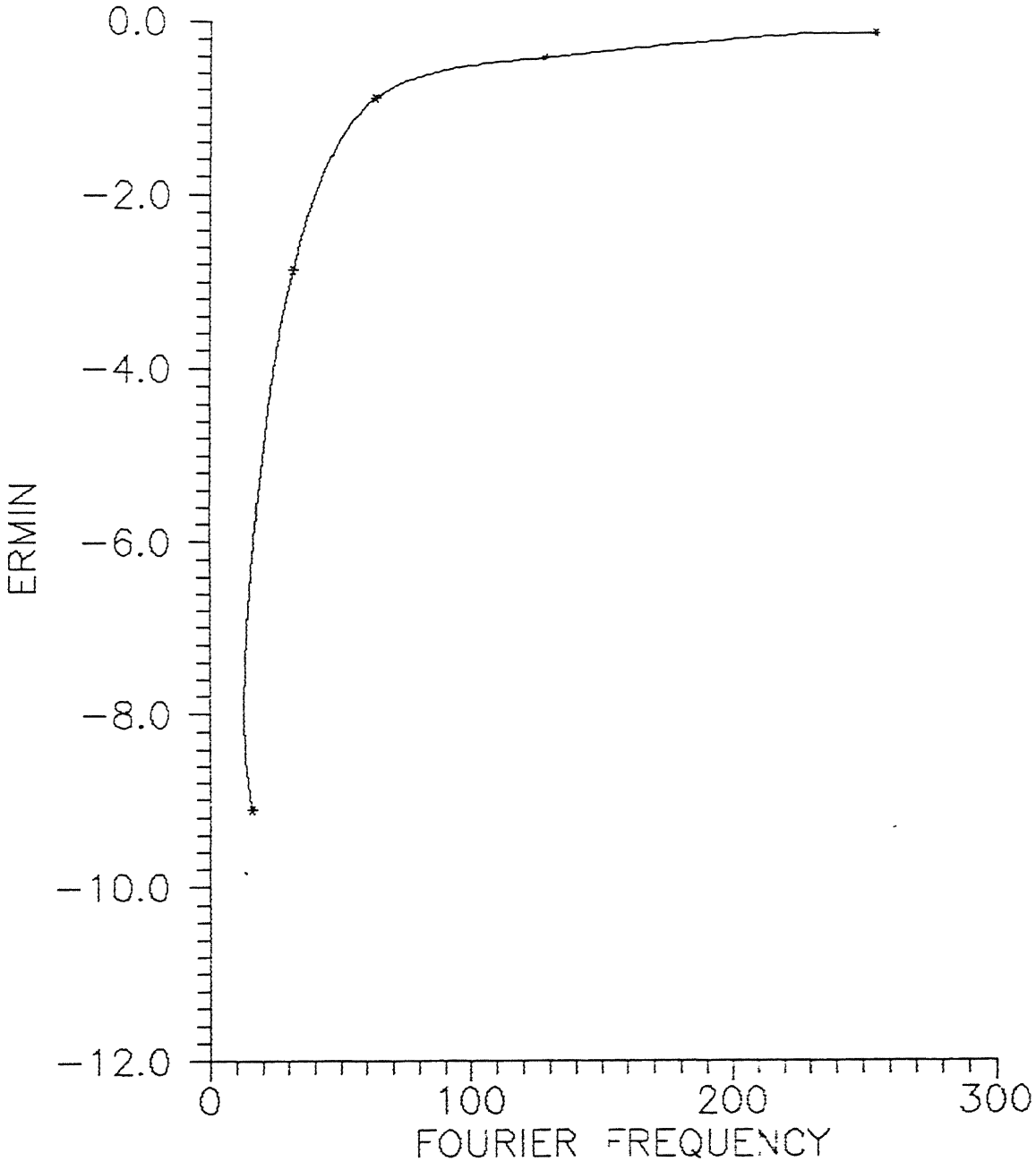

Figure B.10: Error Variation With Fourier Frequency for JET

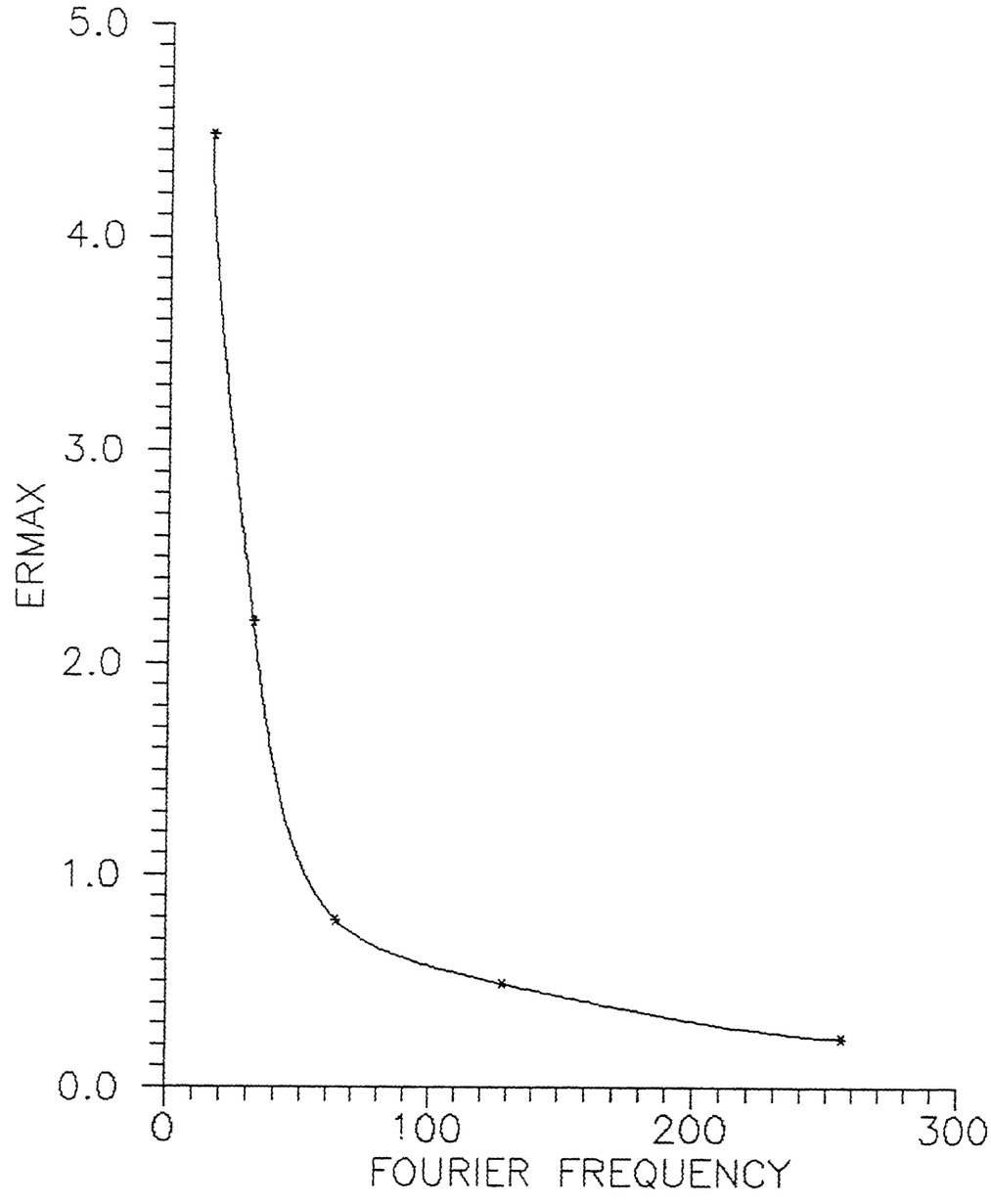

Figure B.11: Error Variation With Fourier Frequency for CRO

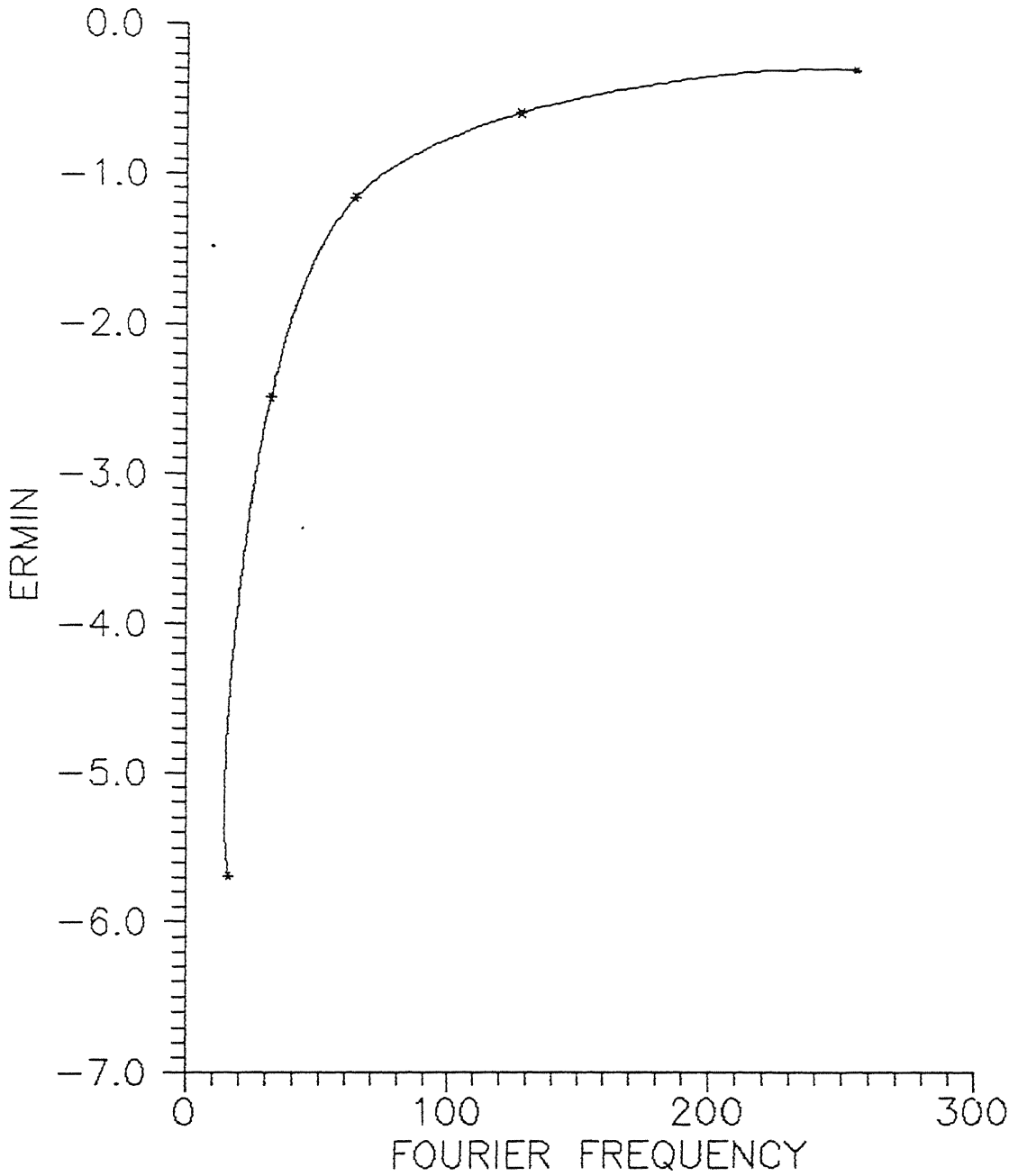

Figure B.12: Error Variation With Fourier Frequency for CRO

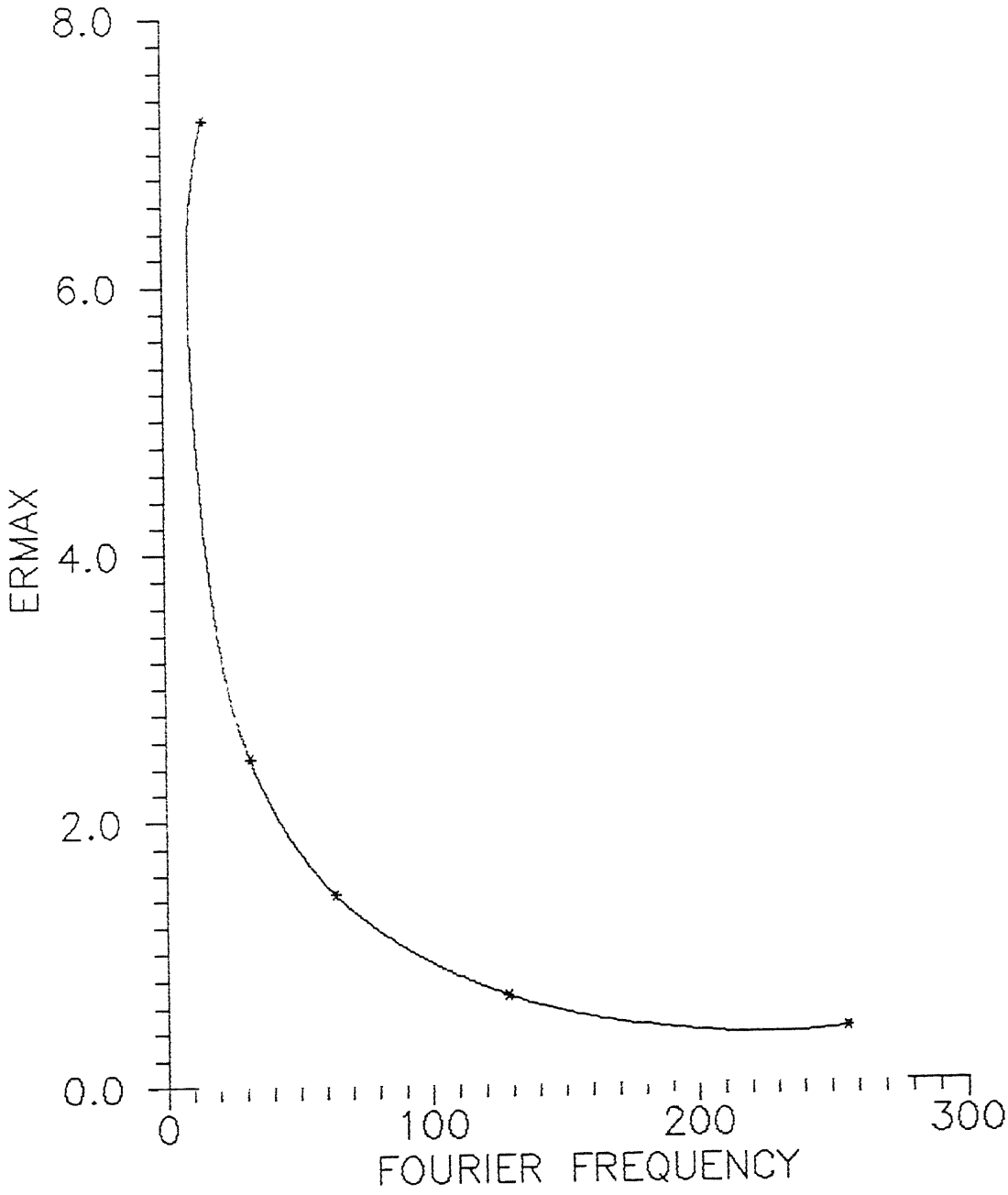

Figure B.13: Error Variation With Fourier Frequency for THO

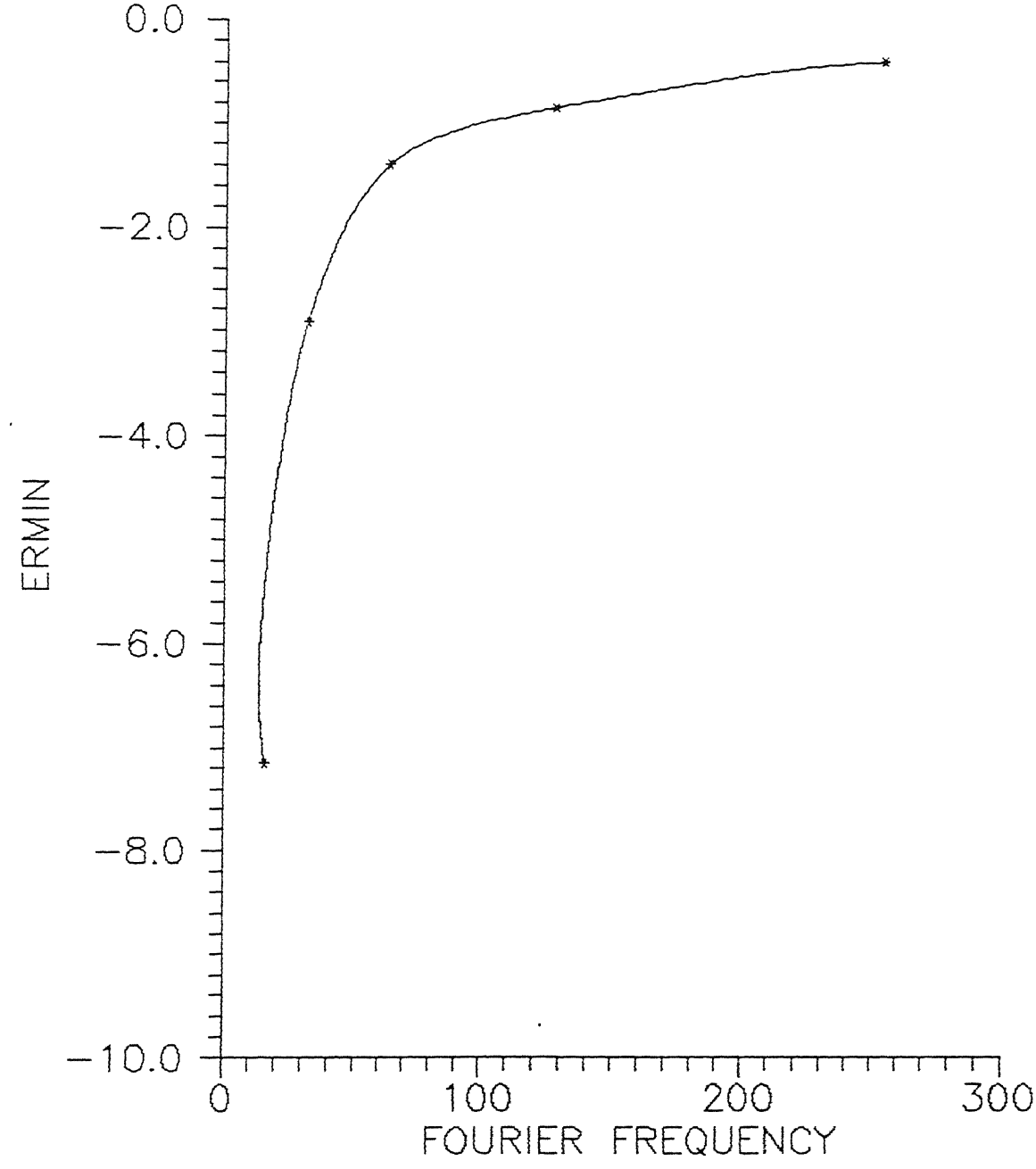

Figure B.14: Error Variation With Fourier Frequency for THO

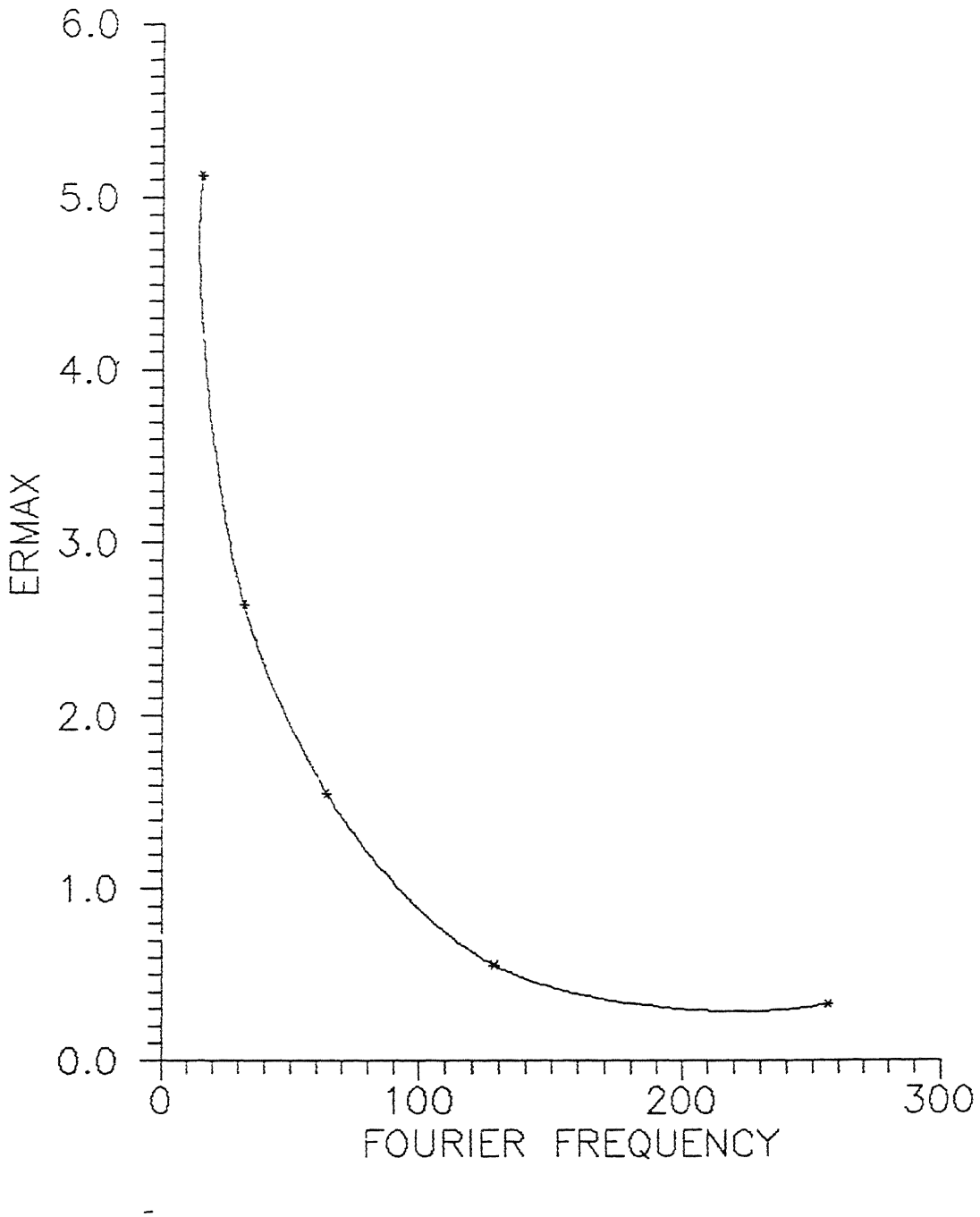

Figure B.15: Error Variation With Fourier Frequency for TST

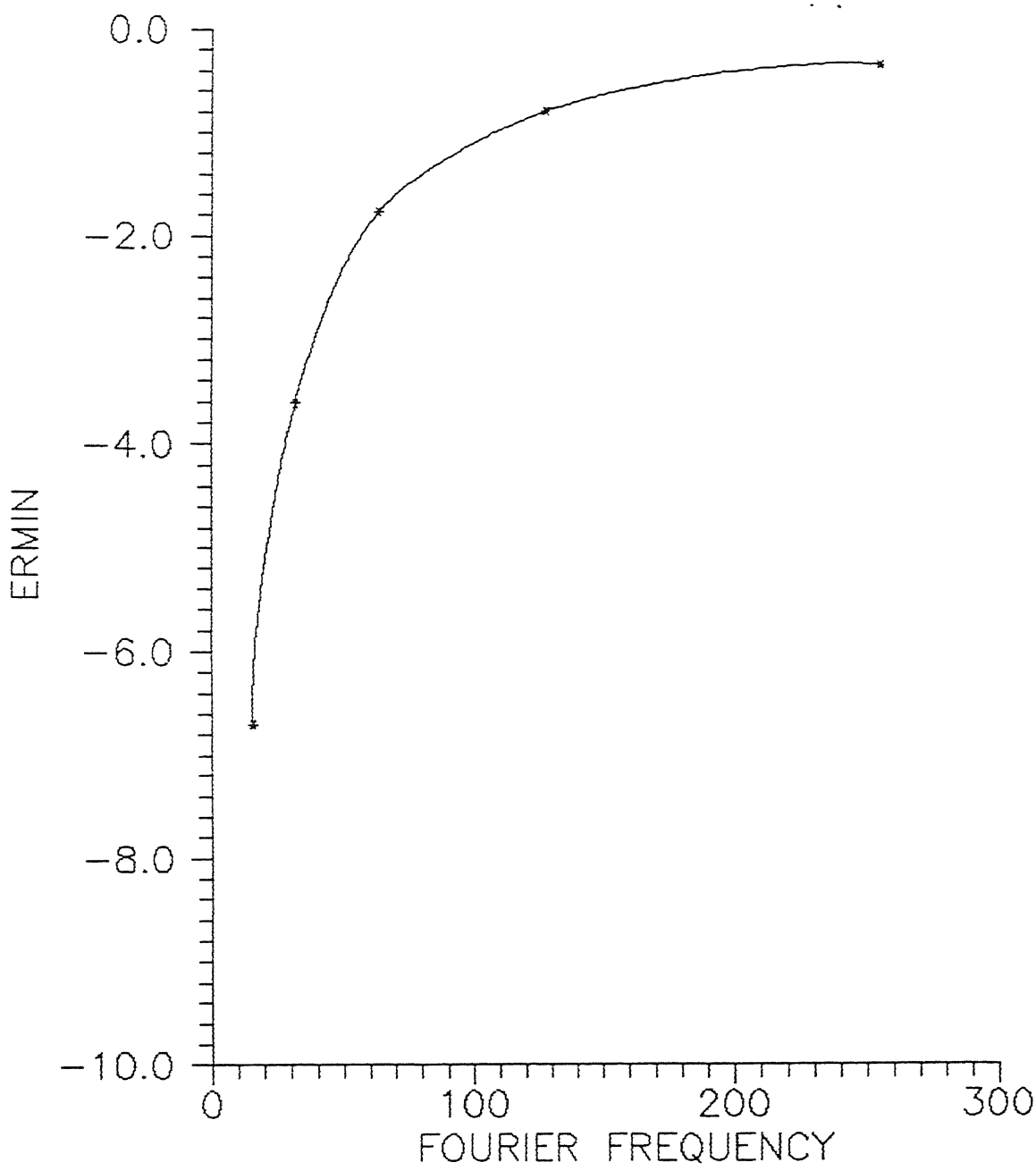

Figure B.16: Error Variation With Fourier Frequency for TST

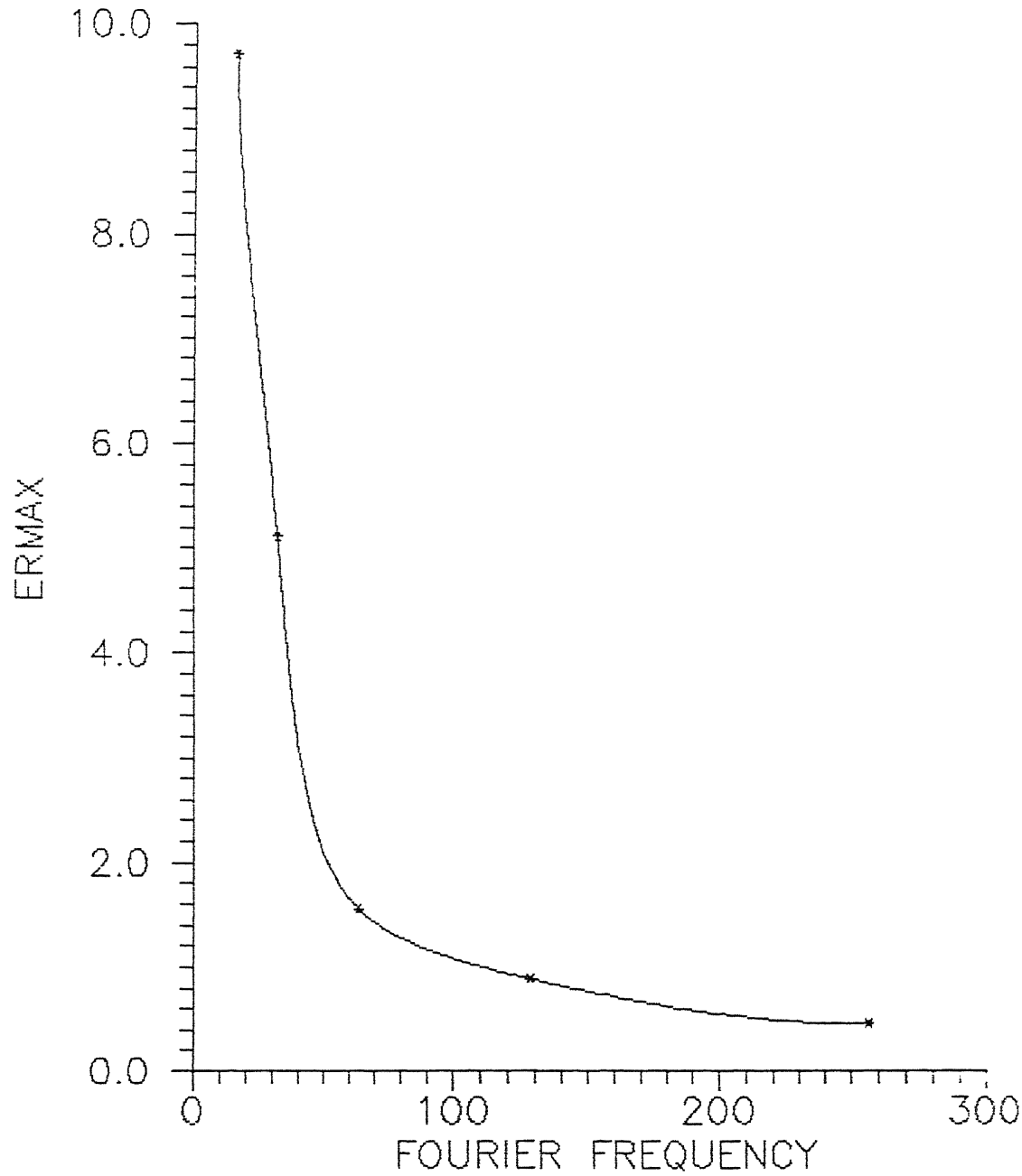

Figure B.17: Error Variation With Fourier Frequency for BRN

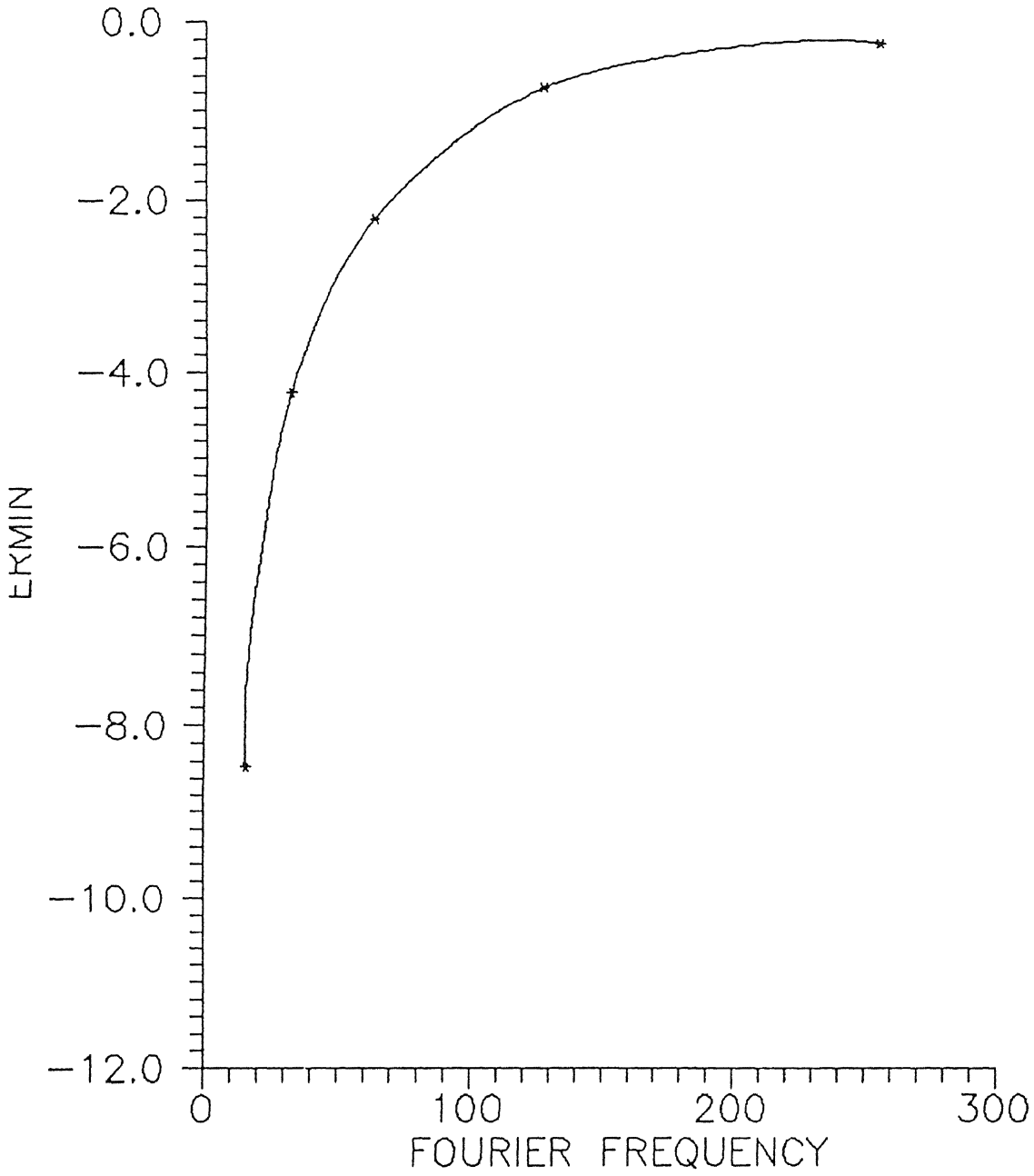

Figure B.18: Error Variation With Fourier Frequency for BRN

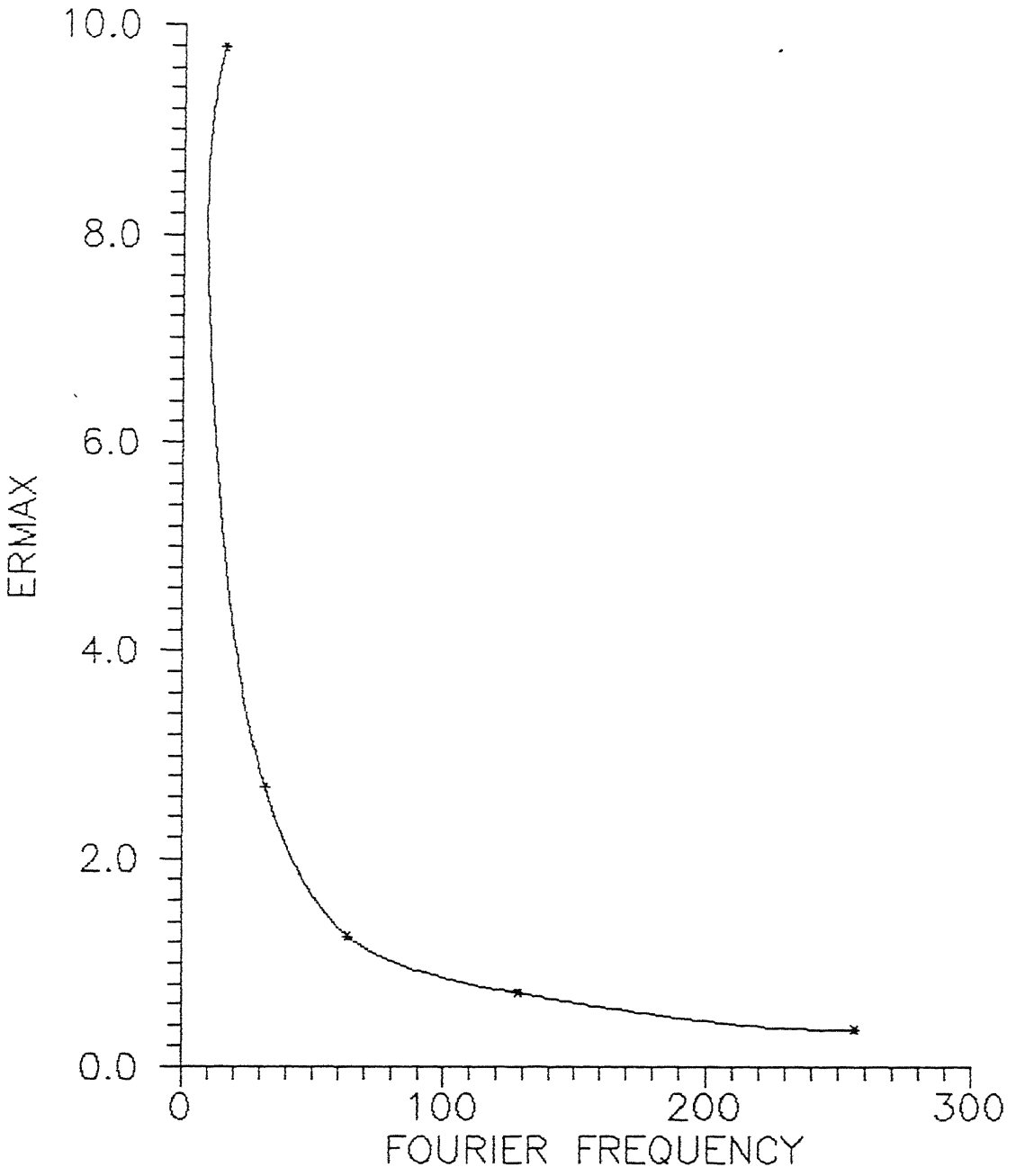

Figure B.19: Error Variation With Fourier Frequency for PIC

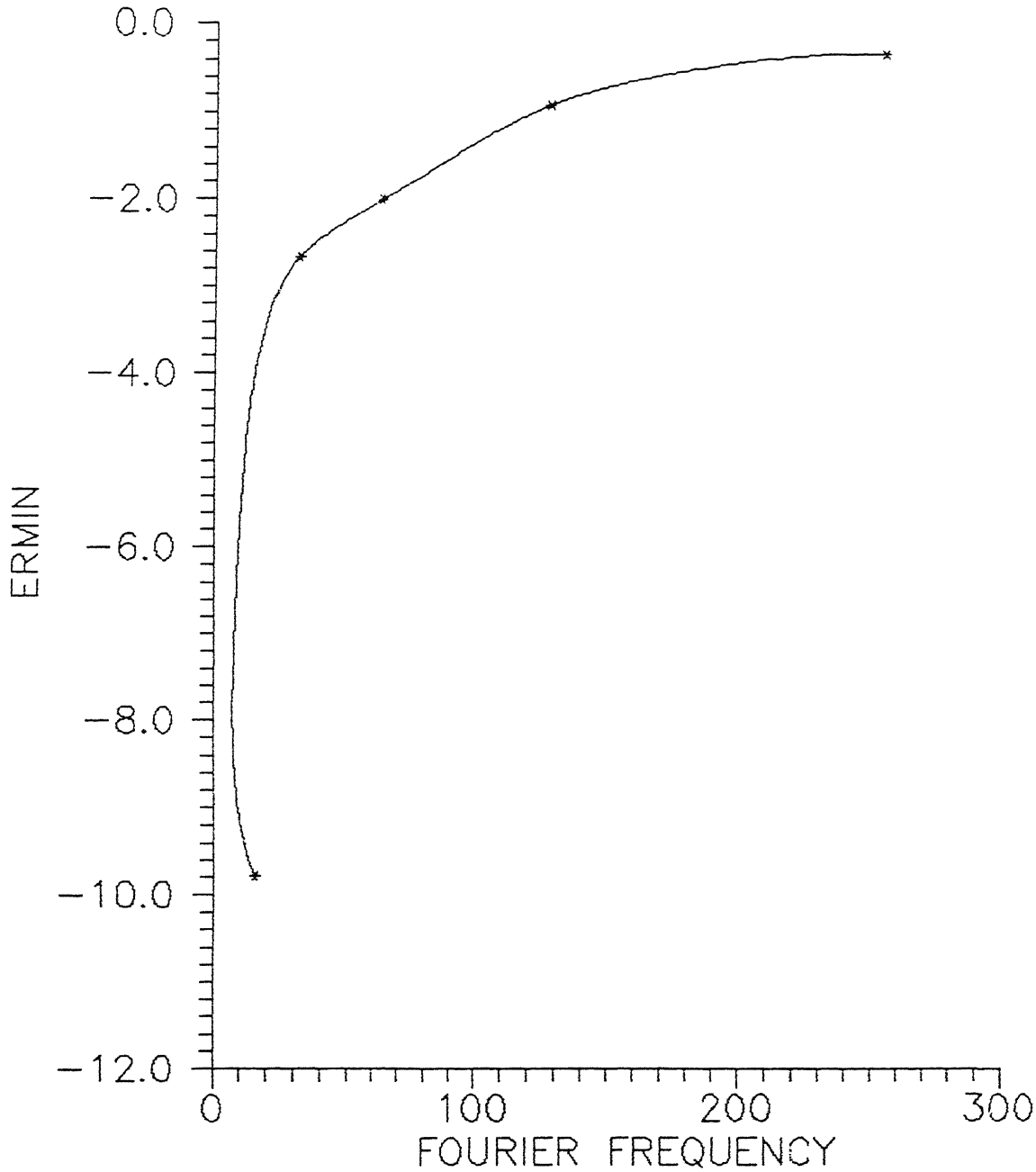

Figure B.20: Error Variation With Fourier Frequency for PIC

Bibliography

[1] J. Radon, Über die Bestimmung von Funktionen durch ihre Integralwerte längs gewisser Maanigfaltigkeiten, *Berichte Sächsische Akademie der Wissenschaften Leipzig, Math.–Phys. Kl.* **69**, (1917) pp.262–267.

[2] R. N. Bracewell. Strip integration in radio astronomy. *Aust. J. Phys.*, **9**, (1956) pp.198–217

[3] A. M. Cormack. Representation of a function by its line integrals with some radiological applications. *J. Appl. Phys.*, **35**, (1964) pp. 195–207

[4] R. N. Bracewell, and A. C. Riddle. Inversion of fan beam scans in radio astronomy. *Astrophy. J.*, **150**, (1967) pp.427-434

[5] G. N. Ramachandran, and A. V. Lakshminarayan. 3-D reconstruction from radiographs and electron micrographs : Application of convolution instead of Fourier transforms.*Proc. National. Academy. Science , USA*, **68**, (1971) pp.2236–2240

[6] G. N. Hounsfield. Computerized transverse axial scanning tomography. Part I : Description of the system. *Br. J. Radiol.*, **46**, (1973) pp.1016–1022

[7] P. Munshi, A review of computerized tomography with application to two-phase flows, *Sadhana*, **15**, (1990) pp.43–55.

[8] P. Munshi, Two-phase Flow Studies in the Bubbly Flow Regime Using a Scanning Gamma-Ray Densitometer, *Master of Science Thesis*, Ohio State University, (1979).

[9] P. Munshi, Error estimates for the convolution backprojection algorithm in computerized tomography, *Doctor of Philosophy Thesis*, IIT Kanpur (1988).

[10] R. K. S. Rathore, P. Munshi, P. Arora, S. D. Malik, A. K. Vaish, K. S. Singh, and U. Singh, A new non-Fourier tomographic filter for image reconstruction, *Nucl. Technol.*, **85**, (1989) pp.346–349

[11] P. Arora, P. Munshi, and R. K. S. Rathore, Higher order tomographic filters for non destructive purposes, *Nucl. Technol.*, **83**, (1988) pp.228–230.

[12] G. T. Herman, *Image Reconstruction from Projections : The Fundamentals of Computerized Tomography*, Academic Press, New York (1980)

[13] L. A. Shepp and B. F. Logan, The Fourier reconstruction of Head Section, *IEEE Trans. : Nucl. Sci.*, bf NS–21, (1974) pp.21–43.

[14] G. T. Herman and A. Naparstek, Fast image reconstruction based on a Radon inversion formula appropriate for rapidly collected data, *SIAM J. Appl. Math.*, **33**, (1978) pp.511–533.

[15] R. M. Lewitt. Reconstruction algorithms : Transform methods, *Proc. IEEE*, **71**(3), (1983), pp. 390–408

[16] P. Munshi, R. K. S. Rathore, K. S. Ram and M. S. Kalra, Error estimates for tomographic inversion, *Inverse Problems*,**7**, (1991) pp.399-408.

[17] F. Natterer, *The Mathematics of Computerized Tomography*, John Wiley & Sons, New York, (1986)

[18] Kwoh, I. S. Reed, T. K. Truong and C. M. Chang, 3–D reconstruction for diverging X-ray beams, *IEEE Trans. : Nucl. Sci.*, bf NS–25(3), (June 1978) pp.1006-1014.

[19] A. Mackovski, Physical problems of computerized tomography, *Proceedings of the IEEE*, 71(3), (1983) pp.373–378.

[20] V. Bhatt, P. Munshi, and J. K. Bhattacharjee, Analysis of the performance of medical CT scanners using fractal theory, *Bulletin of Radiation Protection*, **13**(2), (1990) pp.38–40.

[21] R. K. S. Rathore, P. Munshi, and R. K. Jarwal, Measurement of void–fraction distribution using a tomographic chord segment inversion algorithm, *Nucl. Technol.*, **82** (1987), pp.227–234

[22] W. H. Miller. The design of a portable CAT scanner for utility pole inspection. *Trans. American. Nuclear. Society*, **52**, (1986) pp. 350–351